Delft University of Technology
Faculty of Civil Engineering and Geosciences
Department of Structural Engineering
Section of Structural Mechanics

Topology Optimization of Wave Barriers

Development of a tool for use in engineering practice

Master Thesis

Author:
A.S. de Zeeuw
alwin_de_zeeuw@hotmail.com

Graduation committee
Prof. Dr. Ir. A.V. Metrikine (TU Delft)
Dr. Ir. K.N. van Dalen (TU Delft)
Dr. Ir. M.J.M.M. Steenbergen (TU Delft)
Dr. Ir. H.G. Stuit (Movares)

June 21, 2018

Abstract

Railway traffic and other sources of environmentally induced vibrations are often the cause of annoyance and sometimes even property damage. Mitigation measures can be used to reduce these vibrations. A common mitigation measure is the stiff wave barrier. These wave barriers are placed in the soil and used to impede the waves on their path from the source to the receiver. The geometries of the wave barriers that are used in practice are very simple. More complex geometries have not often been considered as it is difficult to estimate which changes to the geometries would increase the effectiveness of the wave barriers.

In literature, topology optimization was explored as a method to design wave barriers that have an increased effectiveness. This method was applied while modelling the soil as a homogeneous elastic half-space. The resulting wave barriers showed a significant increase in the achieved vibration reduction. However, the designs were often very complex and hard to manufacture. The goal of this thesis was the creation of a topology optimization tool that can be used in engineering practice. Two improvements were made to the method found in literature:

- A layered soil model was implemented
- The manufacturability of the optimized wave barriers was increased

The improved method was then applied to multiple situations in order to investigate aspects of wave barrier design and effectiveness. Application to a frequency independent homogeneous soil model showed the importance of the dimensions of the wave barrier relative to the encountered wavelengths for the wave barrier effectiveness. Even when using topology optimization, minimum wave barrier dimensions were required to achieve significant vibration reduction. A comparison of wave barriers optimized for homogeneous soils with those optimized for layered soils showed the significance of using a layered soil model. The interface between two layers resulted in reflections that could diminish the effectiveness of a wave barrier. The optimization algorithm responded to these reflections by placing material in the path of waves that would otherwise reflect back to the surface. For other soils the optimization algorithm responded differently. A wave barrier optimized for a three-layered soil model that consisted of a softer layer embedded in a stiff layer and a stiff half-space appeared to use the softer layer as a waveguide in order to reduce the energy at the surface.

The increase of the manufacturability was accomplished using a combination of a robust topology optimization approach and a vertical filter. This resulted in wave barriers with a more manufacturable design at the cost of a decrease in vibration reduction. In three of the four cases, the optimized wave barrier still performed significantly better than the reference wave barrier. In one case, the final design reverted back to the reference wave barrier when the manufacturability conditions were applied.

The goals set at the start of the thesis were largely accomplished. The model was able to more accurately reflect soil profiles found in practice by using a layered soil model and the topology optimization algorithm resulted in wave barriers that are relatively easy to manufacture while still showing a significant improvement over the standard reference wave barriers. The possible use of soft embedded layers as waveguides was discovered during the optimization. Future research into this possibility could prove valuable. Some concerns are posited with regards to the reliability of the wave barriers. In some cases, the optimized wave barrier appeared to abuse the idealized representation of the interface between layers. An initial investigation showed that in those cases, the effectiveness of the wave barrier was sensitive to changes of the interface depth. Further investigation would be required to determine the sensitivity of the designed wave barriers to other parameters related to the idealized representations of the interfaces.

Contents

List of Figures

List of Tables

Acronyms

BESO	Bi/directional evolutionary structural optimization.
DOF	Degrees of freedom.
ESO	Evolutionary structural optimization.
FEA	Finite element analysis.
FEM	Finite element method.
GCMMA	Globally converging method of moving asymptotes.
MMA	Method of moving asymptotes.
OC	Optimality criteria method.
PML	Perfectly matched layers.
SIMP	Solid isotropic material with penalization.

Symbols

Sign	Description	Unit
E_r	Energy reduction ratio	$-$
E	Young's modulus	N/m^2
K	Global stiffness matrix	$-$
M	Global mass matrix	$-$
S	Global dynamic stiffness matrix	$-$
V	Volume	m^3
ϵ_0	Volumetric strain $(\epsilon_{xx} + \epsilon_{yy} + \epsilon_{zz})$	$-$
ϵ	Strain	$-$
λ_R	Rayleigh wavelength	m
λ	Lamé's first parameter	N/m^2
μ	Lamé's second parameter	N/m^2
∇^2	Laplace operator $\left(\frac{\delta^2}{\delta x^2} + \frac{\delta^2}{\delta y^2} + \frac{\delta^2}{\delta z^2}\right)$	$-$
ν	Poisson's ratio	$-$
ω	Frequency	rad/s
ρ	Density	kg/m^3
σ	Stress	N/m^2
c_p	P-wavespeed	m/s
c_r	Rayleigh wavespeed	m/s
c_s	S-wavespeed	m/s
c	Wavespeed	m/s
k_e	Element stiffness matrix	$-$
k_p	P-wavenumber	m^{-1}
k_r	Rayleigh wavenumber	m^{-1}
k_s	S-wavenumber	m^{-1}
k	Wavenumber	m^{-1}
m_e	Element mass matrix	$-$

Part I

Introduction

Chapter 1

Introduction

1.1 Background

Ground-borne vibration is a commonly reported problem among residents near railway traffic [3, 4]. Vibrations are generated at the interface between the wheel and rail due to various factors. Among these are track unevenness, the effect of quasi-static moving loads and transient effects due to rail joints, switches and crossings [5]. As a consequence of these vibrations, waves are propagated through the ground. The waves propagating from railway traffic depend not only on the properties of the train, wheels and the railway track but also on the properties of the underlying soil. In the Netherlands, the soil profile is often layered, consisting of softer upper layers overlying stiffer soil layers [6]. The wavespeeds and the layer depth of the softer upper soil layer influence the frequencies of the generated waves. For upper layers with a thickness of 2-6 m, the most severe vibrations often occur in the range 10-40 Hz [7]. If the upper layer reaches a greater depth and is characterized by a lower wavespeed, the most severe vibrations can occur at frequencies below 10 Hz.

These low frequency waves can induce vibrations in structures in the vicinity of railway tracks [8]. While these vibrations are not likely to damage the structure, they can be in the perceptible range of residents. There are two main ways that residents perceive these vibrations, depending on the frequency range. Low frequency vibrations in the range 1-80 Hz can be perceived as mechanical vibration of the human body, resulting in annoyance, increased heart rates and reduced sleep quality [9, 10]. Higher frequency vibrations in the range 16-250 Hz can be radiated as sound inside buildings [3, 7, 11]. For structures in the vicinity of railway tracks these effects are not a rare occurrence. A review of reports from from 9 countries across the world on ground vibration along railway tracks showed that in 44% of all reports the national or international ground vibration limitation was exceeded in at least one section [12]. The same review found that in 49% of reports mitigation measures were deemed necessary.

Mitigation measures can be applied at the source, the receiver and on the transmission path. When vibration reduction is required in a situation with existing track and structures, a mitigation measure focused on the transmission path is the most attractive option. A number of different mitigation measures for the transmission path have been studied. Among these are open trenches [7], soft and stiff buried wall barriers [7, 13, 11], sub-grade stiffening [5, 14], wave impeding blocks [15, 16] and wave reflectors [17].

The expected vibration reduction is the most important factor when deciding which measure to use. Aside from effectiveness, environmental and economical aspects are contributing factors as well. A study into the environmental and economical costs of the available mitigation

measures showed that the buried wall barriers were among the most expensive measures [18]. The material required for constructing the mitigation measures was a major contributing factor for the economical cost and the environmental impact. Reducing the required material appears to be an attractive option for controlling these costs. Material reduction is often not seen as a possibility as it would adversely affect the effectiveness of the measure. This is true for the simple design geometries that have largely been the focus of past studies. However, with the availability of construction methods such as jet-grouting, more complex geometries can be realized. The possibility of more complex geometries could allow for more optimal use of material, reducing the environmental costs of the wave barriers. Regarding the economical costs, optimal use of material would lead to a reduction only if the decrease in material costs outweighs the possible increase in construction costs due to the more complex geometries.

This problem was approached by Van Hoorickx et al. (2016) by using the method of structural topology optimization [19, 20]. Structural topology optimization is a numerical method to iteratively improve the design towards an optimum. Using this method, material is iteratively placed and moved around to wherever it is most effective. The results are designs that make very effective use of all the available material.

In order to facilitate the optimization of wave barriers the vibrations must be determined. For this purpose, Van Hoorickx et al. (2016) used a 2D homogeneous elastic solid to model the soil. The source was modelled as a vertical harmonic point load at the surface. The displacements resulting from this load were calculated in the frequency domain. The cross-section of a wave barrier was then optimized to reduce the vibrations at the target location under a specified maximum volume of wave barrier material. The frequency range for which the wave barriers were optimized was 20-80 Hz. The initial results were very promising. For all cases the optimized wave barriers showed a significant improvement in vibration reduction for the chosen location behind the barrier.

There were some limitations to these studies that inhibit the use of their method in practice. The limitations pertain to the accuracy of the model, the source frequencies that were used and the complexity of the final optimized designs:

1. As stated, Van Hoorickx et al. (2016) used a homogeneous soil model. In practice, soils are hardly ever homogeneous. Especially in the Netherlands, where different layers such as clay, peat and sand occur frequently be found.

2. The frequency range will also generally be lower than that discussed in the papers by Van Hoorickx et al. (2016). Again, especially in the Netherlands, where softer upper layers are often found, dominant frequencies occur below 10 Hz.

3. The complexity of the optimized designs also prevents them from being used in practice. While the optimized designs showed a significant increase in vibration reduction for an identical volume, the increase in complexity would increase the production costs to such a degree that using a larger amount of material in a standard geometric shape still appears to be the more feasible approach.

1.2 Scope

1.2.1 Goals

The goal of this thesis is the development of a tool for the optimization of wave barriers that results in designs that are usable in engineering practice. This will be attempted by improving upon the method of Van Hoorickx et al. (2016) in two ways:

- The implementation of layered soils
- The increase of the manufacturability of the optimized wave barriers

Using this improved model, three areas of interest will be investigated pertaining to the design of wave barriers for a low frequency range, the design of wave barriers in a layered soil model and the design of manufacturable wave barriers.

Low frequency range

For soils with relatively soft and large upper layers, the frequency of the strongest vibrations caused by railway traffic can be below 10 Hz. In the Netherlands the soils are often very soft, leading to a higher occurrence of low frequency vibrations and waves with a greater wavelength. In general the amplitude of waves with a greater wavelength are difficult to reduce using wave barriers [11, 21]. However, the geometries of studied wave barriers have generally been relatively simple. More complex geometries might facilitate the reduction for even waves of greater wavelength. This leads to the first research question:

1. Does topology optimization offer significant benefits when the aim is to reduce low frequency vibrations?

Layered soil model

For an accurate soil model, it is recommended to at least model the soil as a series of parallel layers with different properties [3]. The previous studies used a homogeneous soil model. During this thesis the implementation of a layered soil model will be investigated. It is expected that wave barriers optimized for homogeneous soil models would be inefficient in a layered soil model, resulting in changes to the topology of the optimized wave barriers. This is captured in the following research question:

2. In what ways does the introduction of a layered soil model affect the topology of an optimized wave barrier?

The implementation of layers also introduces new uncertainties regarding the robustness of the design to changes in the soil model. Determining the soil profile is often an uncertain process and subject to significant deviations between locations only small distances apart. The result is that the soil profile might deviate from what was used in the model. As a result, the sensitivity of the optimized design to changes of the soil profile is investigated as well. In this thesis the focus is on the uncertainties introduced by the implementation of a layered soil model. Two important uncertainties are introduced in a layered soil model. The first is the interface depth, the second is the relative stiffness ratios between the layers and the wave barrier material. In this thesis, only the influence of the interface depth is investigated. The relevant research question is formulated as:

3. How sensitive are the designed wave barriers to changes of the interface depth?

Manufacturable design

Van Hoorickx et al. (2016) used a robust form of topology optimization that ensured that small changes in the design of the wave barriers would not significantly influence the effectiveness of the wave barrier [19, 20]. This allowed for the simplification of the wave barrier design in a post-processing step. However, even the resulting simplified barriers were still relatively complex,

consisting of multiple parts buried beneath each other within the soil. During this thesis an attempt will be made to increase the manufacturability of the optimized wave barriers. However, the increase of manufacturability will always lead to a less optimal design, giving way to the final research question:

4. How can the manufacturability of the designed barriers be increased and what effects does this have on the wave barrier effectiveness?

1.2.2 Approach

The model used in this thesis will largely mirror that used by Van Hoorickx et al. (2016). Before implementing the layered soil profile, topology optimization will be applied to low frequency sources to investigate the extent to which wave barriers of complex geometry can be used to mitigate waves induced by low frequency sources. A wavelength dependent model will be created to provide some insight into the required wave barrier dimensions to achieve significant vibration reductions. A layered soil model will then be implemented and validated to allow the algorithm to design wave barriers for more practical soil types and to investigate the influence of different soil models on the optimized designs. Wave barriers will be optimized for different layered soil models to highlight different ways in which the topology optimization program copes with the effects of a layered soil. After designing wave barriers for layered soil models, the sensitivity of these optimized wave barriers to deviations of the interface depth will be investigated. Lastly, the optimization algorithm will be expanded upon to increase the manufacturability of the wave barriers. Different levels of manufacturability are compared in terms of topology and vibration reduction.

1.2.3 Limitations

The limitations in this thesis relate mostly to the accuracy of the model that is used. The accuracy will be increased by the addition of a layered soil model, but other aspects that can be of importance to an accurate modelling of the problem will not be considered. Two important aspects related to the source and the receiver will be highlighted here.

Source limitations

The source in this thesis will be modelled as a harmonic point load on a 2D model. This is equivalent to an infinite line load on a 3D model. This modelling is a great simplification of the loads that can be expected of railway traffic. The waves generated by railway traffic depend on a complex interaction between the vehicle, the entire railway track structure and the underlying ground. A recent study modelled track-ground vibrations induced by railway traffic using a combined 3D model of the vehicle, of the railway track and its underlying structure and of the ground itself [22]. After a 98 hour calculation, validation with experimental data showed good agreement. As topology optimization requires a large number of iterations, a 3D model is not viable. Simulating a moving load would still be possible using a 2.5D model. However, that is outside of the scope of this thesis.

Receiver limitations

The receivers in this thesis will consist of an area of soil at the surface of the model. As stated before, annoyance generally depends on the vibration of buildings. For the response of buildings but also the soil, soil-structure interaction can be an important factor. In practice this interaction

is often taken into account by including the structure in the model or by using adjustment factors to account for vibration attenuation through the foundation, floors and spans [23]. While it would be possible to include a structure in the model, the type of structure would be heavily dependent on the case and it is therefore not included in this thesis.

Optimization limitations

Related to the previous limitations, the medium will be modelled using a 2D plane strain model because of the computation time required for a 3D model. This prevents the optimization of a 3D wave barrier. As a result, only the cross-section of a wave barrier is optimized. The considered model also does not include the possibility of the addition of elements above the surface. As a result, measures such as heavy masses near the source [17] or possibly a measure similar to tuned mass dampers can not be considered in the optimization process. Lastly, while optimization of the material properties is possible, it is not considered in this thesis.

1.3 Outline

This thesis is divided into 5 parts. Part I covers the background of the thesis and included the goals and scope. Part II discusses relevant theory. It contains a chapter describing wave propagation in linear elastic solids and a chapter giving an introduction to topology optimization and its advantages and disadvantages. Part III discusses the finite element model complete with validation and shortcomings, and the application of topology optimization to the wave barrier problem. In part IV the goals and research questions are investigated. Part 9 discusses the results and the complications that were encountered throughout the thesis.

Part II

Theory

Chapter 2

Wave propagation

If at a location the ground is disturbed, this disturbance elicits a propagating wave that carries the effects to different locations. In this thesis the focus will be on the effects of environmental disturbances at the surface on the vibrations at the surface a certain distance removed from the disturbance. Wave propagation near the surface is therefore especially important. This chapter will discuss the wave propagation in media that are infinite in all but one direction. To do this, first a concise derivation of the equations of motion is given. This is followed by the discussion of the relevant wave types in homogeneous semi-infinite media and then expanded to layered semi-infinite media.

2.1 Equations of motion

In this derivation a Cartesian coordinate system is used (x, y, z) with corresponding displacements u, v, w (figure 2.1).

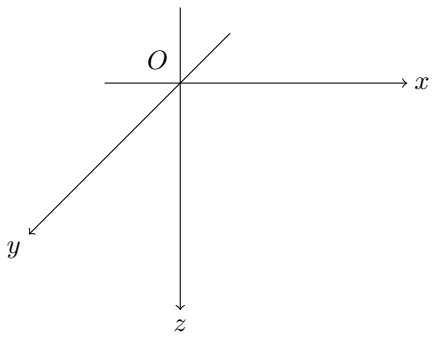

Figure 2.1: Coordinate system

The kinematic equations can then be given in the form:

$$\begin{aligned}
\epsilon_{xx} &= \frac{\delta u}{\delta x} \\
\epsilon_{yy} &= \frac{\delta v}{\delta y} \\
\epsilon_{zz} &= \frac{\delta w}{\delta z} \\
\epsilon_{xy} = \epsilon_{yx} &= \frac{1}{2}\left(\frac{\delta u}{\delta y} + \frac{\delta v}{\delta x}\right) \\
\epsilon_{yz} = \epsilon_{zy} &= \frac{1}{2}\left(\frac{\delta v}{\delta z} + \frac{\delta w}{\delta y}\right) \\
\epsilon_{zx} = \epsilon_{xz} &= \frac{1}{2}\left(\frac{\delta w}{\delta x} + \frac{\delta u}{\delta z}\right)
\end{aligned} \tag{2.1}$$

The constitutive equations can be given in matrix formulation as:

$$\begin{bmatrix} \sigma_{xx} \\ \sigma_{yy} \\ \sigma_{zz} \\ \sigma_{xy} \\ \sigma_{yz} \\ \sigma_{zx} \end{bmatrix} = \begin{bmatrix} \lambda+2\mu & \lambda & \lambda & 0 & 0 & 0 \\ \lambda & \lambda+2\mu & \lambda & 0 & 0 & 0 \\ \lambda & \lambda & \lambda+2\mu & 0 & 0 & 0 \\ 0 & 0 & 0 & \mu & 0 & 0 \\ 0 & 0 & 0 & 0 & \mu & 0 \\ 0 & 0 & 0 & 0 & 0 & \mu \end{bmatrix} \begin{bmatrix} \epsilon_{xx} \\ \epsilon_{yy} \\ \epsilon_{zz} \\ 2\epsilon_{xy} \\ 2\epsilon_{yz} \\ 2\epsilon_{zx} \end{bmatrix} \tag{2.2}$$

with:

$$\lambda = \frac{\nu E}{(1+\nu)(1-2\nu)}, \qquad \mu = \frac{E}{2(1+\nu)} \tag{2.3}$$

Finally, the equilibrium equations can be given as:

$$\begin{aligned}
\rho\frac{d^2u}{dt^2} &= \rho X + \frac{\delta\sigma_{xx}}{\delta x} + \frac{\delta\sigma_{yx}}{\delta y} + \frac{\delta\sigma_{zx}}{\delta z} \\
\rho\frac{d^2v}{dt^2} &= \rho Y + \frac{\delta\sigma_{xy}}{\delta x} + \frac{\delta\sigma_{yy}}{\delta y} + \frac{\delta\sigma_{zy}}{\delta z} \\
\rho\frac{d^2w}{dt^2} &= \rho Z + \frac{\delta\sigma_{xz}}{\delta x} + \frac{\delta\sigma_{yz}}{\delta y} + \frac{\delta\sigma_{zz}}{\delta z}
\end{aligned} \tag{2.4}$$

The kinematic equations (2.1), the constitutive equations (2.2) and the equilibrium equations (2.4) can then be used to form the equations of motion. If the body forces (X, Y and Z) are neglected, the equations of motion are:

$$\begin{aligned}
\rho\frac{\delta^2u}{dt^2} &= (\lambda+\mu)\frac{\delta\epsilon_0}{\delta x} + \mu\nabla^2 u \\
\rho\frac{\delta^2v}{dt^2} &= (\lambda+\mu)\frac{\delta\epsilon_0}{\delta y} + \mu\nabla^2 v \\
\rho\frac{\delta^2w}{dt^2} &= (\lambda+\mu)\frac{\delta\epsilon_0}{\delta z} + \mu\nabla^2 w
\end{aligned} \tag{2.5}$$

2.2 Wave propagation in infinite media

First the simplest case of linear elastic media will be discussed: the infinite or boundless medium. In a medium of this type there are no boundaries and as a result only one category of waves can

be found: body waves. In order to show the existence of these waves first an intuitive derivation will be done using the propagation of a plane wave in x-direction [24]. Afterwards, a more general derivation will be given according to the method used in Ewing, Jardetzky and Press (1957) [25].

2.2.1 Body waves

In elastodynamics, different wave types can occur depending on the medium and boundary conditions. First the propagation of a plane wave in the x-direction through an unbounded homogeneous medium will be investigated. In this situation all derivatives in y, and z-direction are zero. The equations of motion (2.5) then reduce to:

$$\begin{aligned} \frac{\delta^2 u}{dt^2} &= c_p^2 \frac{\delta^2 u}{\delta x^2} \\ \frac{\delta^2 v}{dt^2} &= c_s^2 \frac{\delta^2 v}{\delta x^2} \\ \frac{\delta^2 w}{dt^2} &= c_s^2 \frac{\delta^2 w}{\delta x^2} \end{aligned} \tag{2.6}$$

with:

$$\begin{aligned} c_p &= \sqrt{\frac{\lambda + 2\mu}{\rho}} \\ c_s &= \sqrt{\frac{\mu}{\rho}} \end{aligned} \tag{2.7}$$

The equations of motion show the possibility of three different waves.

- A longitudinal wave with a displacement in the same direction as the direction of propagation. The velocity of this wave is c_p.
- A transverse wave with a displacement perpendicular to the direction of propagation. The velocity of this wave is c_s.
- A second transverse wave with a displacement perpendicular to both the direction of propagation and the previously mentioned transverse wave. The velocity of this wave is also c_s.

It is important to realize that $c_p > c_s$. If a disturbance occurs, the longitudinal waves will be the first to arrive. As a result, the longitudinal wave is often referred to as the primary wave (P-wave), while the transverse waves are referred to as secondary waves (S-waves). Within the secondary waves a differentiation can be made between vertically polarized waves (SV-waves) characterized by vertical displacements and horizontally polarized waves (SH-waves) characterized by horizontal displacements. In 2D the SV-waves are concerned with in-plane motion, while the SH-waves are concerned with out-of-plane motion. The above derivation is valid for a plane wave travelling in the x-direction. In the general derivation, use is made of the Helmholtz decomposition. By using the Helmholtz decomposition, a vector can be decomposed into the gradient of a scalar potential (ϕ) and the curl of a vector potential (ψ_j). When applied to the displacements, the result is the following:

$$\begin{aligned} u &= \frac{\delta \phi}{\delta x} + \frac{\delta \psi_3}{\delta y} - \frac{\delta \psi_2}{\delta z} \\ v &= \frac{\delta \phi}{\delta y} + \frac{\delta \psi_1}{\delta z} - \frac{\delta \psi_3}{\delta x} \\ w &= \frac{\delta \phi}{\delta z} + \frac{\delta \psi_2}{\delta x} - \frac{\delta \psi_1}{\delta y} \end{aligned} \tag{2.8}$$

Inserting equations (2.8) into the first of the equation of motion (2.5) results in the following:

$$\frac{\delta}{\delta x}\left(\rho\frac{\delta^2\phi}{\delta t^2}\right)+\frac{\delta}{\delta y}\left(\rho\frac{\delta^2\psi_3}{\delta t^2}\right)-\frac{\delta}{\delta z}\left(\rho\frac{\delta^2\psi_2}{\delta t^2}\right)=(\lambda+\mu)\frac{\delta}{\delta x}\nabla^2\phi+\mu\frac{\delta}{\delta x}\nabla^2\phi+\mu\frac{\delta}{\delta y}\nabla^2\psi_3-\mu\frac{\delta}{\delta z}\nabla^2\psi_2 \tag{2.9}$$

Similar results can be found for the other equations of motion. It can be seen that equation (2.9) is satisfied if the following equations are satisfied:

$$\begin{aligned}\frac{\delta^2\phi}{\delta t^2}&=\frac{\lambda+2\mu}{\rho}\nabla^2\phi\\ \frac{\delta^2\psi_2}{\delta t^2}&=\frac{\mu}{\rho}\nabla^2\psi_2\\ \frac{\delta^2\psi_3}{\delta t^2}&=\frac{\mu}{\rho}\nabla^2\psi_3\end{aligned} \tag{2.10}$$

When including the other equations of motion, all equations of motion are satisfied if the following equations are satisfied:

$$\begin{aligned}\nabla^2\phi&=\frac{1}{c_p^2}\frac{\delta^2\phi}{\delta t^2}\\ \nabla^2\psi_i&=\frac{1}{c_s^2}\frac{\delta^2\psi_i}{\delta t^2}\quad\text{for } i=1,2,3\end{aligned} \tag{2.11}$$

with c_p and c_s as defined in (2.7). Note that the scalar potential and vector potential equations resemble the wave equation. Similar to the previous derivation, waves travelling with a velocity of either c_p or c_s can be inferred.

2.3 Wave propagation in semi-infinite media

In this section the consequences of a free surface are discussed. First the reflection of body waves at the free surface is shown. Second, the emergence of surface waves, resulting from the boundary conditions at the surface are discussed.

2.3.1 Reflection at free surface

The model is changed to include a free surface at $z=0$. Again a plane wave will be considered, except now the travelling direction will be considered more generally as perpendicular to the y-direction (2.2). The consequence of this is that now only the derivatives in the y-direction are fixed at zero. The displacements expressed in terms of the potentials (2.8) then become:

$$\begin{aligned}u&=\frac{\delta\phi}{\delta x}-\frac{\delta\psi_2}{\delta z}\\ v&=\frac{\delta\psi_1}{\delta z}-\frac{\delta\psi_3}{\delta x}\\ w&=\frac{\delta\phi}{\delta z}+\frac{\delta\psi_2}{\delta x}\end{aligned} \tag{2.12}$$

Two cases will be discussed. First incident P-waves propagating in the AO-direction in the xz-plane at an angle e with the free surface are discussed (see figure 2.2). Using the chosen

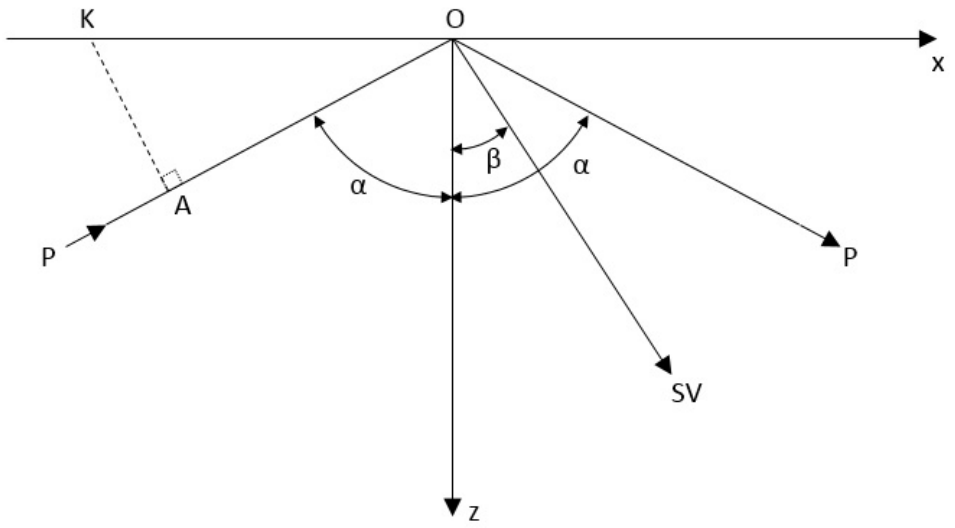

Figure 2.2: Reflection of a P-wave at the free surface of an elastic solid

reference axes, the plane P- and SV-waves can be described using only the displacements u and w. As a result, the waves depend only on ϕ and ψ_2. The functions for ϕ and ψ_2 must satisfy the wave equations (2.11).

In order to cope with the boundary conditions at $z = 0$, solutions to the wave equations (2.11) will be sought for in the form:

$$\begin{aligned} \phi &= f(z)e^{ik(ct-x)} \\ \psi &= g(z)e^{ik(ct-x)} \end{aligned} \tag{2.13}$$

Substituting the expression for ϕ and ψ_2 in (2.11) results in:

$$\begin{aligned} \frac{\delta^2 f}{\delta z^2} + \left(\frac{c^2}{c_p^2} - 1\right) k^2 f = 0 \\ \frac{\delta^2 g}{\delta z^2} + \left(\frac{c^2}{c_s^2} - 1\right) k^2 g = 0 \end{aligned} \tag{2.14}$$

The general solutions for $f(z)$ and $g(z)$ can then be found as:

$$\begin{aligned} f(z) &= A_1 e^{\left(ik\sqrt{\frac{c^2}{c_p^2}-1}z\right)} + A_2 e^{\left(-ik\sqrt{\frac{c^2}{c_p^2}-1}z\right)} \\ g(z) &= B_1 e^{\left(ik\sqrt{\frac{c^2}{c_s^2}-1}z\right)} + B_2 e^{\left(-ik\sqrt{\frac{c^2}{c_s^2}-1}z\right)} \end{aligned} \tag{2.15}$$

Using (2.15), (2.13) can be written in the form:

$$\begin{aligned} \phi &= A_1 e^{\left[ik\left(ct+\sqrt{\frac{c^2}{c_p^2}-1}z-x\right)\right]} + A_2 e^{\left[ik\left(ct-\sqrt{\frac{c^2}{c_p^2}-1}z-x\right)\right]} \\ \psi_2 &= B_1 e^{\left[ik\left(ct+\sqrt{\frac{c^2}{c_s^2}-1}z-x\right)\right]} + B_2 e^{\left[ik\left(ct-\sqrt{\frac{c^2}{c_s^2}-1}z-x\right)\right]} \end{aligned} \tag{2.16}$$

In equation (2.16), c should be interpreted as an apparent velocity along the surface. If in figure 2.2, KA represents the P-wave front and AO represents the distance travelled by the P-wave front in a unit time (c_p), then the distance traced by the wave front in unit time along the surface is $OK = c$. It follows then that, similar to Snell's law:

$$c = \frac{c_p}{\sin\alpha} = \frac{c_s}{\sin\beta} \tag{2.17}$$

If only incident P-waves are considered, $B_1 = 0$ in (2.16). The remaining constants can be determined using the free surface boundary conditions:

$$\begin{aligned} \sigma_{zz}(z=0) &= 0 \\ \sigma_{xz}(z=0) &= 0 \end{aligned} \tag{2.18}$$

Using the kinematic equations (2.1), the constitutive equations (2.2), the displacements expressed in terms of potentials (2.12) and the assumption of a plane wave $\left(\frac{\delta}{\delta y} = 0\right)$, the boundary conditions can be expressed as follows:

$$\begin{aligned} [\sigma_{zz}]_{z=0} &= \lambda\left(\frac{\delta^2\phi}{\delta x^2} + \frac{\delta^2\phi}{\delta z^2}\right) + 2\mu\left(\frac{\delta^2\phi}{\delta z^2} + \frac{\delta^2\psi_2}{\delta x \delta z}\right) = 0 \\ [\sigma_{xz}]_{z=0} &= \mu\left(2\frac{\delta^2\phi}{\delta x \delta z} + \frac{\delta^2\psi_2}{\delta x^2} - \frac{\delta^2\psi_2}{\delta z^2}\right) = 0 \end{aligned} \tag{2.19}$$

Using the boundary conditions, the angles as shown in figure 2.2 and $\kappa = c_p/c_s$, the coefficients of the reflected P- and SV-wave with respect to the incident P-wave can be determined as [26].

$$\begin{aligned} \frac{A_2}{A_1} &= \frac{\sin 2\alpha \sin 2\beta - \kappa^2 \cos^2 2\beta}{\sin 2\alpha \sin 2\beta + \kappa^2 \cos^2 2\beta} \\ \frac{B_2}{A_1} &= \frac{2\kappa \sin 2\alpha \cos 2\beta}{\sin 2\alpha \sin 2\beta + \kappa^2 \cos^2 2\beta} \end{aligned} \tag{2.20}$$

Three important conclusions can be drawn from equation (2.20). First, because $\sin\beta = \kappa^{-1}\sin\alpha$, the amplitude ratios depend only on the angle of the incident wave and the constant κ. Second, an incident P-wave is reflected solely as a P-wave if $\alpha = 0°$, or $\alpha = 90°$. Third, if $\sin 2\alpha \sin 2\beta = \kappa^2 \cos^2 2\beta$, the incident P-wave is reflected solely as an SV-wave.

An incident SV-wave can be considered by taking $A_1 = 0$ in equation (2.16). Using the angles as specified in figure 2.3 and the boundary conditions as shown above, the solutions are:

$$\begin{aligned} \frac{A_2}{B_1} &= \frac{\kappa \sin 4\beta}{\sin 2\beta \sin 2\alpha + \kappa^2 \cos^2 2\beta} \\ \frac{B_2}{B_1} &= \frac{\sin 2\beta \sin 2\alpha - \kappa^2 \cos^2 2\beta}{\sin 2\beta \sin 2\alpha + \kappa^2 \cos^2 2\beta} \end{aligned} \tag{2.21}$$

From equation (2.21) it becomes clear that the coefficient for the reflected P-wave (A_2) is zero for incident angles $\beta = 0$, $\beta = \pi/4$, $\beta = \pi/2$. For these angles an incident SV-wave is reflected as an SV-wave. An incident SV-wave would reflect fully as a P-wave if $A_2 = 0$. However, the relation between α and β:

$$\sin\alpha = \kappa \sin\beta \tag{2.22}$$

shows that α is only real-valued if

$$\beta < \sin^{-1}\kappa^{-1} \tag{2.23}$$

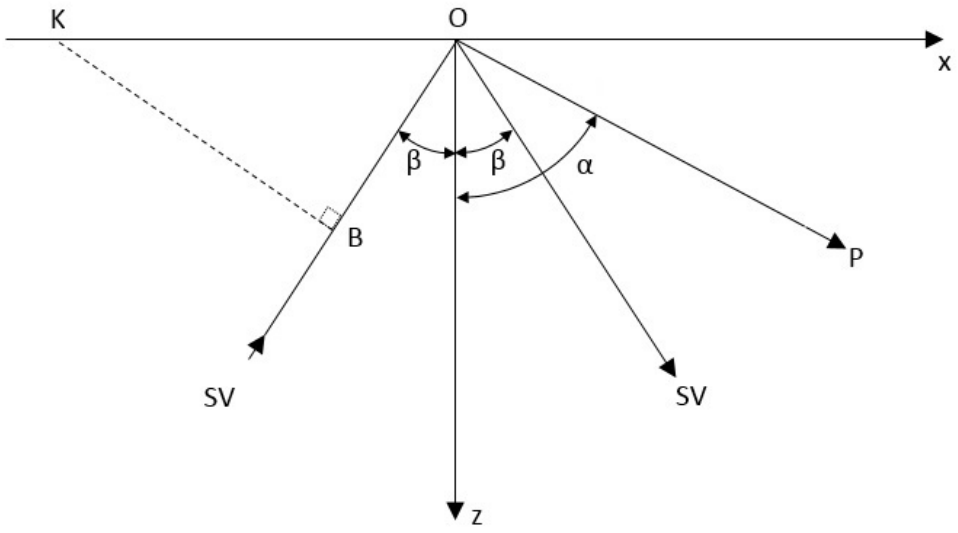

Figure 2.3: Reflection of an S wave at the free surface of an elastic solid

If β is greater than this critical angle, α becomes complex. The consequence of this is that in equation (2.17), $\sin\alpha > 0$ and as a result $c < c_p$. In equation (2.16), $\sqrt{c^2/c_p^2 - 1}$ becomes complex, leading to a P-wave that propagates in x-direction, with an amplitude that decays with increasing depth. A wave of this type is called a surface wave [26].

2.3.2 Interface waves

Interface waves have two important properties [24]:

- The wave propagates along the interface (which is the surface for a homogeneous half-space or the interface between two layers).
- The amplitude of the wave decreases with distance to the interface.

Different interface waves exist. The one that is most relevant for this thesis is the Rayleigh wave. The Rayleigh wave is a surface wave. In addition to the properties mentioned above, Rayleigh waves also have the property that the disturbance is independent of the coordinates perpendicular to the travelling direction [25]. The Rayleigh wave is especially important for the considered cases as most of the energy resulting from a vertical point load at the surface on a 3D model is radiated as a Rayleigh wave [27]. While this thesis uses an infinite line load, the Rayleigh wave is still expected to hold a significant part of the energy.

A function can be formulated that meets all conditions mentioned above:

$$f(z) = A_1 e^{\left(-k\sqrt{1-\frac{c^2}{c_p^2}}z\right)} + A_2 e^{\left(k\sqrt{1-\frac{c^2}{c_p^2}}z\right)} \tag{2.24}$$

The potentials should approach zero as z approaches ∞. Assuming that $c < c_s < c_p$, it can be seen that $A_2 = 0$. A similar result is acquired for $g(z)$, leading to the following solutions for

ϕ and ψ_i:

$$\begin{aligned}\phi &= Ae^{\left(-k\sqrt{1-\frac{c^2}{c_p^2}}z\right)}e^{ik(ct-x)} \\ \psi_j &= B_j e^{\left(-k\sqrt{1-\frac{c^2}{c_s^2}}z\right)}e^{ik(ct-x)} \quad \text{for} \quad j=1,2,3\end{aligned} \tag{2.25}$$

The constants can be determined by using appropriate boundary conditions. A half-space was assumed with a free surface at $z = 0$. The accompanying boundary conditions are that the stresses must be zero at $z = 0$ (in addition to the condition that the displacement approaches zero as z approaches ∞). The following conditions are used:

$$\begin{aligned}[\sigma_{zz}]_{z=0} &= \lambda\left(\frac{\delta^2\phi}{\delta x^2}+\frac{\delta^2\phi}{\delta z^2}\right)+2\mu\left(\frac{\delta^2\phi}{\delta z^2}+\frac{\delta^2\psi_2}{\delta x\delta z}\right)=0 \\ [\sigma_{xz}]_{z=0} &= \mu\left(2\frac{\delta^2\phi}{\delta x\delta z}+\frac{\delta^2\psi_2}{\delta x^2}-\frac{\delta^2\psi_2}{\delta z^2}\right)=0 \\ [\sigma_{yz}]_{z=0} &= \mu\left(\frac{\delta^2\psi_1}{\delta z^2}-\frac{\delta^2\psi_3}{\delta x\delta z}\right)=0\end{aligned} \tag{2.26}$$

Inserting the solutions for ϕ and ψ_i into (2.26) and using (2.7) gives:

$$\begin{aligned}\left(2-\frac{c^2}{c_s^2}\right)A-2\sqrt{\frac{c^2}{c_s^2}-1}B_2=0 \\ 2\sqrt{\frac{c^2}{c_p^2}-1}A+\left(2-\frac{c^2}{c_s^2}\right)B_2=0\end{aligned} \tag{2.27}$$

and:

$$i\sqrt{1-\frac{c^2}{c_s^2}}B_3+\left(\frac{c^2}{c_s^2}-1\right)B_1=0 \tag{2.28}$$

B_1 and B_3 cannot be solved due to a lack of boundary conditions. However, entering (2.28) into the potentials (2.25) and inserting the result into the expression for displacement v (2.12) shows that $v = 0$. Therefore, the displacement v and the accompanying constants (B_1, B_3) need not be considered.

A nontrivial solution for A and B_2 can only be found if the determinant of (2.27) is equal to zero, meaning:

$$\left(2-\frac{c^2}{c_s^2}\right)^2-4\sqrt{1-\frac{c^2}{c_p^2}}\sqrt{1-\frac{c^2}{c_s^2}}=0. \tag{2.29}$$

After expanding (2.29), $\frac{c^2}{c_s^2}$ can be factored out:

$$\frac{c^2}{c_s^2}\left(\frac{c^6}{c_s^6}-8\frac{c^4}{c_s^4}+24\frac{c^2}{c_s^2}-16\frac{c^2}{c_p^2}+16\frac{c_s^2}{c_p^2}-16\right)=0. \tag{2.30}$$

Surface waves can exist if $0 < c < c_s < c_p$ and in that case a root to equation (2.30) can always be found [25]. Denoting c as c_R, because it represents the phase velocity of Rayleigh waves, c_R can be approximated by the function [26]:

$$c_R=\frac{0.862+1.14\nu}{1+\nu}c_s, \tag{2.31}$$

where ν is Poisson's ratio and c_R increases monotonically from $0.862c_s$ to $0.955c_s$.

Importance of Rayleigh waves

In the paper investigating the surface-waves, Lord Rayleigh already mentioned the likely importance of the surface-waves in earthquakes and the collision of solids, due to their divergence in only two dimensions [28]. Here the decay of the amplitude due to spatial spreading will be discussed to highlight the importance of the Rayleigh waves. To do this, first the energy present in a harmonic wave with length λ is required. Adding both the kinetic and the potential energy results in an equation for the total mechanical energy [24]:

$$E_{mech} = \frac{1}{2} A \lambda \rho \omega^2 \hat{u}^2 \tag{2.32}$$

Important in equation (2.32) is the relation between energy and amplitude $\left(E \propto \hat{u}^2\right)$. If decay due to internal friction and reflection is ignored, the only decay is due to spatial spreading of the energy. For body waves resulting from a point load, the energy is spread over a shell with increasing radius R. The volume of a spherical shell can be approximated by multiplying the outer surface area of the shell with the thickness of the shell: $\left(V \approx 4\pi R^2 \lambda\right)$. The result is that the energy is inversely proportional to the distance travelled squared: $E \propto \frac{1}{R^2}$. Taking into account the quadratic relation between the amplitude and the energy, the amplitude of body waves is inversely proportional to simply the distance travelled:

$$\hat{u} \propto \frac{1}{R} \tag{2.33}$$

In contrast, the energy of surface waves is spread over the volume of a cylinder with increasing radius. The volume for a cylindrical shell can be determined using: $V = \pi h R t$, where R is the center radius, rather than the outer radius. In a similar reasoning as above, the proportional relation between the amplitude and the distance travelled can be determined for surface waves as:

$$\hat{u} \propto \frac{1}{\sqrt{R}} \tag{2.34}$$

Although these relations are only valid in the far field, the much lower decay due to spatial spreading shows the importance of Rayleigh waves. In some literature it is claimed that waves generated by a road or railway can be modeled as a line load if the distance between the receiver and the load is less than approximately $\frac{1}{\pi}$ times the length of the road or train [29]. This would mean that spatial spreading for body waves would occur as a cylindrical shell (2.34), while Rayleigh waves would experience no spatial spreading at all.

2.3.3 Lamb's Problem

Up to this point only free propagating waves have been discussed. In a very influential paper, Lamb discussed the propagation of waves over the surface of an elastic solid resulting from a force at the surface [30]. In this paper multiple closely related problems were discussed, but one in particular is especially relevant to this thesis: the displacements at the surface resulting from the application of a harmonic vertical point load on a 2D soil.

Lamb used an approach similar to that shown previously for determining reflections and free Rayleigh waves. The only difference was the addition of a distributed normal force at $z = 0$. The used boundary conditions then become:

$$[\sigma_{xz}]_{z=0} = 0, \qquad [\sigma_{zz}]_{z=0} = Y e^{ikx} \tag{2.35}$$

Note that the time-dependent term is excluded. It is included again in the final expression for the displacements. Combining these conditions with the expression for the displacements

(equation 2.8) and the solutions for ϕ and ψ in equation 2.25 gives the following expression for the displacements at $z = 0$:

$$\begin{aligned} u_0 &= \frac{ik\left(2k^2 - k_s^2 - 2\sqrt{k^2 - k_p^2}\sqrt{k^2 - k_s^2}\right)e^{ikx}}{\left(2k^2 - k_s^2\right)^2 + 4k^2\sqrt{k^2 - k_p^2}\sqrt{k^2 - k_s^2}}\frac{Y}{\mu} \\ w_0 &= \frac{k_s^2\sqrt{k^2 - k_p^2}e^{ikx}}{\left(2k^2 - k_s^2\right)^2 + 4k^2\sqrt{k^2 - k_p^2}\sqrt{k^2 - k_s^2}}\frac{Y}{\mu} \end{aligned} \tag{2.36}$$

In order to evaluate the effects of a concentrated force Q instead of the distributed force Y, Fourier's Theorem was used showing that in the expressions above it was required to write $Y = Q\,dk/2\pi$ and integrate with respect to k from $-\infty$ to $+\infty$. This resulted in the expression:

$$\begin{aligned} u_0 &= -\frac{iQ}{2\pi\mu}\int_{-\infty}^{\infty}\frac{k\left(2k^2 - k_s^2 - 2\sqrt{k^2 - k_p^2}\sqrt{k^2 - k_s^2}\right)e^{ikx}}{\left(2k^2 - k_s^2\right)^2 + 4k^2\sqrt{k^2 - k_p^2}\sqrt{k^2 - k_s^2}}dk \\ w_0 &= \frac{Q}{2\pi\mu}\int_{-\infty}^{\infty}\frac{k_s^2\sqrt{k^2 - k_p^2}e^{ikx}}{\left(2k^2 - k_s^2\right)^2 + 4k^2\sqrt{k^2 - k_p^2}\sqrt{k^2 - k_s^2}}dk \end{aligned} \tag{2.37}$$

These integrals are difficult to evaluate analytically as the denominator of the expressions vanishes for certain real values of k. In order to circumvent this, Lamb used contour integration and an expansion in asymptotic form. This method results in a form for the displacements at the surface that has terms for the Rayleigh wave, the shear wave and the compression wave. The first terms of this expansion are:

$$\begin{aligned} u_0 = &-\frac{Q}{\mu}\frac{-k_r\left(2k_r^2 - k_p^2 - 2\sqrt{k_r^2 - k_p^2}\sqrt{k_r^2 - k_s^2}\right)e^{i(\omega t - k_r x)}}{(8(2k_r^2 - k_s^2))k_r - 8k_r\sqrt{k_r^2 - k_p^2}\sqrt{k_r^2 - k_s^2} - 4k_r^3\frac{\sqrt{k_r^2 - k_t^2}}{\sqrt{k_r^2 - k_p^2}} - 4k_r^3\frac{\sqrt{k_r^2 - k_p^2}}{\sqrt{k_r^2 - k_s^2}}} \\ &+ \frac{Q}{\mu}\sqrt{\frac{2}{\pi}}\sqrt{1 - \frac{k_p^2}{k_s^2}}\frac{e^{i\left(\omega t - k_s x - \frac{1/4}{\pi}\right)}}{(k_s x)^{\frac{3}{2}}} \\ &- \frac{Q}{\mu}\sqrt{\frac{2}{\pi}}\frac{k_p^3 k_s^2\sqrt{k_s^2 - k_p^2}}{\left(k_s^2 - 2k_p^2\right)^3}\frac{ie^{i\left(\omega t - k_p x - \frac{1/4}{\pi}\right)}}{(k_p x)^{\frac{3}{2}}} \end{aligned} \tag{2.38}$$

$$\begin{aligned} w_0 = &-\frac{iQ}{\mu}\frac{k_s^2\sqrt{k_r^2 - k_p^2}e^{i(\omega t - k_r x)}}{(8(2k_r^2 - k_s^2))k_r - 8k_r\sqrt{k_r^2 - k_p^2}\sqrt{k_r^2 - k_s^2} - 4k_r^3\frac{\sqrt{k_r^2 - k_t^2}}{\sqrt{k_r^2 - k_p^2}} - 4k_r^3\frac{\sqrt{k_r^2 - k_p^2}}{\sqrt{k_r^2 - k_s^2}}} \\ &+ \frac{2Q}{\mu}\sqrt{\frac{2}{\pi}}\left(1 - \frac{k_p^2}{k_s^2}\right)\frac{ie^{i\left(\omega t - k_s x - \frac{1}{4}\pi\right)}}{(k_s x)^{\frac{3}{2}}} \\ &+ \frac{Q}{2\mu}\sqrt{\frac{2}{\pi}}\frac{k_p^2 k_s^2}{\left(k_s^2 - 2k_p^2\right)^2}\frac{ie^{i\left(\omega t - k_p x - \frac{1}{4}\pi\right)}}{(k_p x)^{\frac{3}{2}}} \end{aligned} \tag{2.39}$$

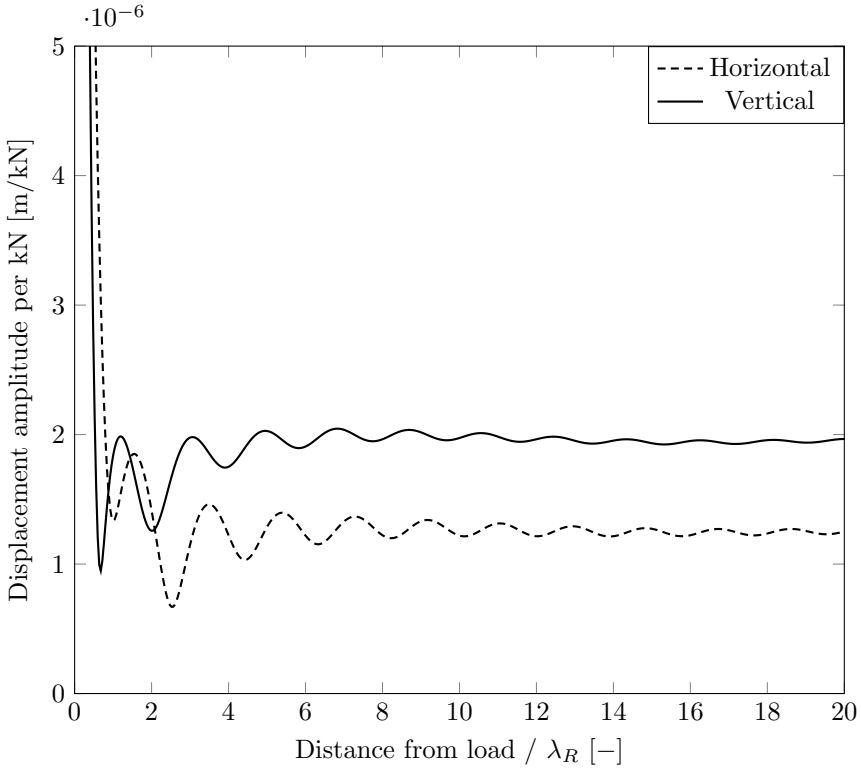

Figure 2.4: Example of the horizontal and vertical displacements at the surface resulting from a concentrated harmonic vertical force at x = 0.

This expression for the displacements is especially informative as it is separated into terms concerning the Rayleigh wave number (k_r), the S-wavenumber (k_s) and the P-wavenumber (k_p). From this expression it becomes clear that the terms with the S-wavenumber and the P-wavenumber diminish with increasing distance from the source as $x^{-\frac{3}{2}}$. More terms can be added from the asymptotic form, but each new term decreases even faster with increasing x. It should be noted that due to the approximation, this analytical solution is only valid for large x. The resulting displacements for a soil with Young's modulus = $2.13e8\,N/m^2$, density = $2000\,kg/m^3$ and Poisson's ratio = 0.33 are given in figure 2.4.

2.4 Wave propagation in layered media

In the derivation for body waves, an unbounded medium was assumed. Extending the situation to a half-space, or a layered half-space introduces reflections and transmission at the interfaces between the layers and at the free surface. A second important consequence of a layered soil model is the dispersion of Rayleigh waves. These two effects are further discussed to show the importance of using an inhomogeneous soil model when designing wave barriers.

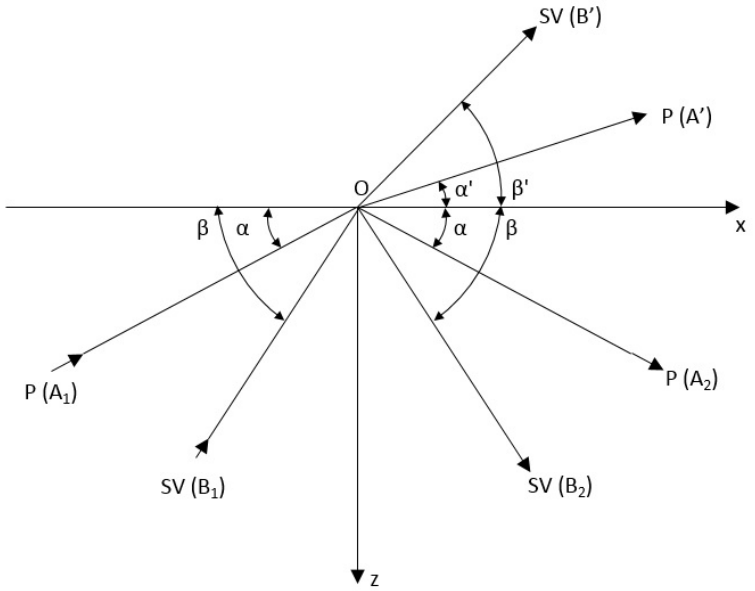

Figure 2.5: Reflection and refraction of waves at the interface surface of two elastic solids

2.4.1 Reflection and refraction of plane waves

Figures 2.2 and 2.3 show that P- and SV-waves encountering a free surface generally produce both reflected P- and SV-waves. When encountering an interface this is still true, but either incoming wave can also produce refracted P- and SV-waves in the ajacent medium (figure 2.5). The consequence of an interface is that two additional equations are required in addition to those given in 2.16:

$$\begin{aligned} \phi' &= A' e^{\left[ik\left(ct+\sqrt{\frac{c^2}{c_{p2}^2}-1}\,z-x\right)\right]} \\ \psi_2' &= B' e^{\left[ik\left(ct+\sqrt{\frac{c^2}{c_{s2}^2}-1}\,z-x\right)\right]} \end{aligned} \tag{2.40}$$

For clarity, the amplitudes from equations (2.16) and (2.40) are shown in figure 2.5 next to the corresponding plane wave. Note that the angles in figure 2.5 are with respect to the interface, where previously the angles were with respect to the normal. The conditions at the interface ($z = 0$) are assumed to be independent of x and t. This means that c and k must be the same in each equation. As a result the following is true for the angles of the reflected and refracted waves:

$$c = \frac{c_{p1}}{\cos\alpha} = \frac{c_{s1}}{\cos\beta} = \frac{c_{p2}}{\cos\alpha'} = \frac{c_{s2}}{\cos\beta'} \tag{2.41}$$

If the amplitudes of the incident waves are assumed to be known, equations 2.16 and 2.40 have four unknowns. These unknowns can be solved for using the following equality conditions at the

interface ($z = 0$):

$$\begin{aligned} u &= u' \\ w &= w' \\ \sigma_{xz} &= \sigma'_{xz} \\ \sigma_{zz} &= \sigma'_{zz} \end{aligned} \tag{2.42}$$

Solving this systems of equations gives relations of a similar nature as (2.20) and (2.21), albeit more complex. For illustrative purposes it is therefore more beneficial to show the energy equations that were derived for reflected and transmitted waves for an incident P-wave and an incident SV-wave [25]:

$$\begin{aligned} 1 &= \frac{A_2^2}{A_1^2} + \frac{\tan\beta B_2^2}{\tan\alpha A_1^2} + \frac{\rho' \tan\alpha' A'^2}{\rho \tan\alpha A_1^2} + \frac{\rho' \tan\beta' B'^2}{\rho \tan\alpha A_1^2} \\ 1 &= \frac{\tan\alpha A_2^2}{\tan\beta B_1^2} + \frac{B_2^2}{B_1^2} + \frac{\rho' \tan\alpha' A'^2}{\rho \tan\beta B_1^2} + \frac{\rho' \tan\beta' B'^2}{\rho \tan\beta B_1^2} \end{aligned} \tag{2.43}$$

A layered medium significantly changes the propagation of the body waves due to reflection and refraction. The effect is especially noticeable when comparing the energy decay due to spatial spreading. In a homogeneous model line load at the surface induces waves that decay due to spatial spreading in the form of a cylinder. For a layered medium the spatial spreading is altered. A larger percentage of the energy will be contained within the upper layers.

2.4.2 Stoneley waves

The presence of multiple layers also allows for the existence of another form of interface waves called Stoneley waves [31]. These are waves that propagate along the interface between two solids. Similar to a Rayleigh wave, these waves also decrease in amplitude with increasing distance from the interface. The wave velocity is between the Rayleigh wave velocity and the greater of the two shear wave velocities. The velocity can be determined using a characteristic equation similar to that found for the Rayleigh waves. However, the equation for Stoneley waves only has real roots for soils that have relatively similar properties and subsequently wave velocities [25]. When the velocities differ significantly and the material of greater density has a velocity greater than that of that of the material of lesser density, complex roots can be found that result in Stoneley waves that leak energy away from the interface as they propagate along it. This situation can occur when the material of greater density has a velocity of up to around three times that of the material of lesser density [32]. If the difference becomes even greater, the Stoneley wave root disappears.

2.4.3 Rayleigh wave dispersion

Previously, the existence of Rayleigh waves was shown using the boundary condition of no stress at the free surface and no displacements at infinite depth. When determining the phase velocity (c_R) of these waves, it became apparent that the transverse displacement perpendicular to both the depth and the travelling direction was inconsequential ($v = 0$). Using the remaining two potentials, equation (2.30) showed that the phase velocity can be determined using the shear wave velocity (c_s) and the compression wave velocity (c_p). If a layered medium is considered, two new potentials must be introduced for each layer. Because each potential has two unknown constants, a medium with N layers has $4N$ unknowns. The introduction of layers also allows for four matching conditions at each interface between two layers. These matching conditions

can be made for $\sigma_{zz}, \sigma_{xz}, u$ and w, for a total of $4(N-1)$ conditions. By including the four boundary conditions ($\sigma_{zz(z=0)} = \sigma_{xz(z=0)} = u_{(z=\infty)} = w_{(z=\infty)} = 0$) there are $4N$ conditions for $4N$ equations, meaning the constants can be solved for. Similar to the previous case, a non-trivial solution exists only if the determinant of the system of equations is zero. Using this, the phase velocity of the Rayleigh waves can be determined. In the homogeneous medium, the wave number could be factored out of the equation, showing that the Rayleigh waves were non-dispersive. This changes in a layered medium. The Rayleigh wave phase velocity is dependent on the wave number.

The dispersive nature of the Rayleigh waves can be inferred by looking at the graphs showing the displacement over depth (figure 2.6). The displacements are significant to a depth of approximately twice the Rayleigh wave length. With high wavenumbers, the displacements are contained mostly in the upper layer. The Rayleigh wave phase velocity then corresponds to the Rayleigh wave phase velocity of the upper layer. However, for lower wavenumbers the displacements associated with the Rayleigh wave are also significant in the deeper layers. The Rayleigh wave phase velocity is then also significantly affected by the properties of the these layers. The result is a frequency dependent phase velocity, showing the dispersive nature of Rayleigh waves.

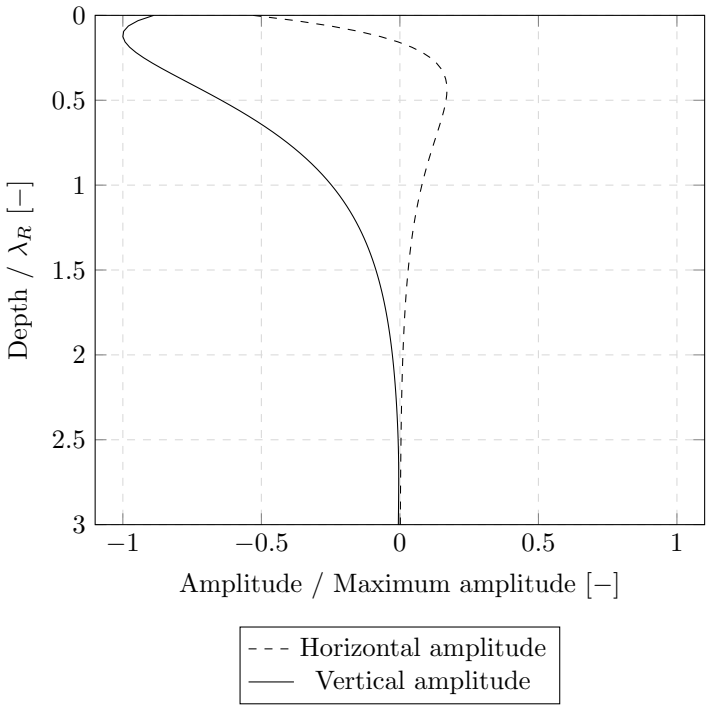

Figure 2.6: Relative Rayleigh wave amplitude over relative depth at 100 wavelengths from source.

The relation between phase velocity and frequency can be illustrated using a dispersion curve. Figure 2.7 shows an example of a dispersion curve for a stiff half-space with a soft upper layer. The properties are as specified in table 2.1. Two important characteristics can be inferred from the dispersion curve. First, the wave speed (phase velocity) of a particular wave can be determined by taking the slope of a line connecting the origin to a particular point on the curve ($c = \omega/k$). Second, the group velocity can be determined by taking the inverse of the slope at a

Layer	Depth (m)	E mod. ($10^6 N/m^2$)	Density (kg/m^3)	Poisson ratio	P-wave speed (m/s)	S-wave speed (m/s)	R-wave speed (m/s)
1	2.0	60	0.44	1500	360	118	112
HS		360	0.49	2000	1755	245	233

Table 2.1: Soil properties of half-space with soft layer

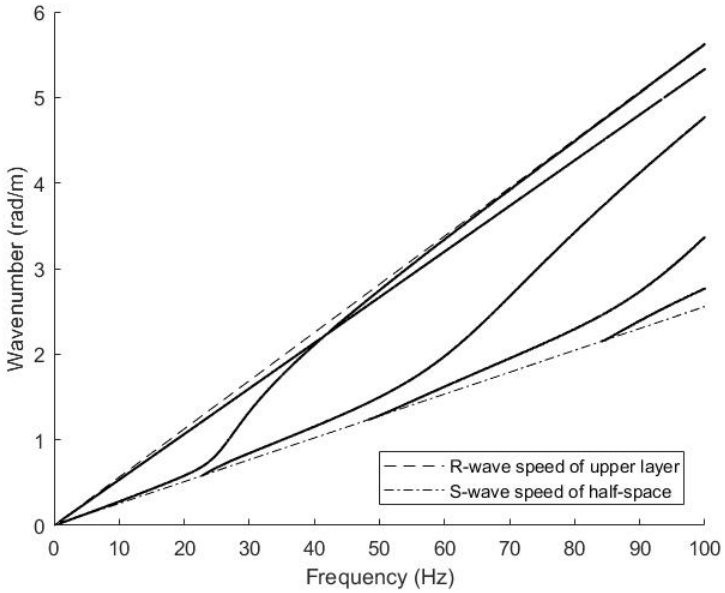

Figure 2.7: Dispersion curve example

point on the curve ($c_g = \delta\omega/\delta k$).

Chapter 3

Topology optimization

3.1 Structural optimization background

The design of structures often involves an iterative-intuitive process during which specific designs are suggested, tested and when necessary adapted. Structural optimization is a mathematical approach to this process. The requirements and goals of the structure are given in a mathematical problem form. The mathematical problem form allows for the use of mathematical algorithms to optimize the structure. This offers many benefits. Not the least of which is the ability to produce structures that perform much more efficiently than their counterparts produced by the traditional iterative-intuitive process. Topology optimization is one of three classes of structural optimization methods (see also figure 3.1):

Sizing optimization: In sizing optimization problems, the design variable x is the size of a structural element. Examples of sizing variables are the thickness distribution of a linearly elastic plate or the cross-section areas of truss members.

Shape optimization: In shape optimization problems, the design variable x represents the form or contour of the boundary of a structure or the location of the nodes of a truss. During the optimization process the boundaries or node locations can be changed. However, the connectivity of the structure is not adaptable. This means that boundaries or nodes cannot disappear, nor can new boundaries or nodes emerge. As a result, shape optimization approaches are not capable changing the topology of the structure, for example by introducing new holes in the structure.

Topology optimization: In topology optimization problems features such as the number, location and shape of holes and the connectivity are determined. The main difference between shape and topology optimization is that the layout concept is known in advance in shape optimization, while it is subject to change in a topology optimization problem.

3.2 Topology optimization

3.2.1 Topology optimization problem form

The formulation of an optimization problem generally uses the following elements [33]:

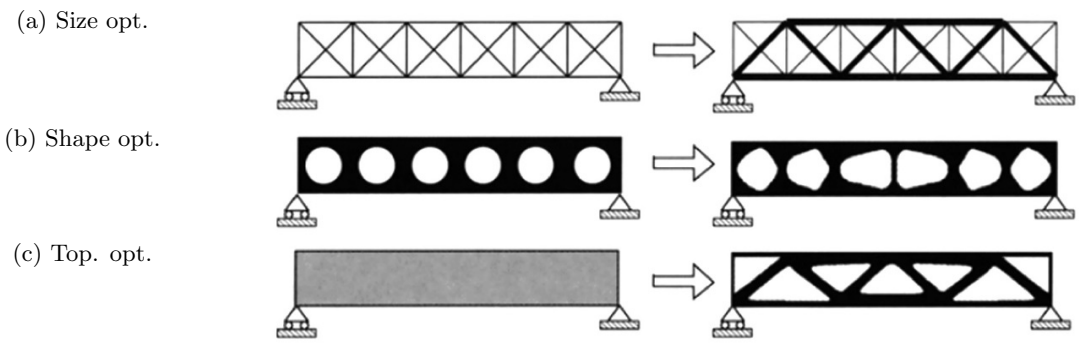

FIGURE 3.1: The three classes of structural optimization [2].

Objective function (f): The objective function returns a scalar value that can be used to describe the quality of the design. Generally, the function is described such that a lower value indicates a higher quality structure.

Design variable (x): The design variable is a function or vector that describes the design (e.g. the thickness of elements or the location of nodes). The variable is adapted in order to optimize the structure.

State variable (y): The state variable is a function or vector that describes the response of the structure (e.g. stress, displacement).

Constraints (g): The constraints are functions that describe the requirements of the structure. Constraints that are a function of a state variable are called behavioral constraints. Constraints that are a function of a design variable are called design constraints. Additionally, there are constraints to ensure equilibrium. These are appropriately named equilibrium constraints. In dynamic structural optimization problems, equilibrium should be seen as dynamic equilibrium.

There are two main ways of formulating the structural optimization problem. A simultaneous and a nested formulation. If equilibrium is solved simultaneously with the optimization problem, it is called a simultaneous formulation. If the equilibrium constraint can be used to determine y from a given x, it is possible to use a nested formulation where $y(x)$ is treated as a given function. As a result, the equilibrium constraint can be left out of the problem formulation. An example for a static problem would be the determination of the displacement as $\mathbf{u} = \mathbf{K}^{-1}\mathbf{F}$. For large discretized systems, the equilibrium constraint in the simultaneous formulation introduces a large number of extra constraints. As a result, it is generally more computationally efficient to use the nested formulation. The same approach is used throughout this thesis. An example of a problem form is given below:

$$\begin{aligned} \min_{\mathbf{x}} \quad & f(\mathbf{x}, \mathbf{u}(\mathbf{x})) \\ \text{s.t.} \quad & g_i(\mathbf{x}, \mathbf{u}(\mathbf{x})) \leq 0 \end{aligned}$$

The problem form should be read as the minimization of the objective function f using the variables x, such that the constraint variables g_i are smaller than or equal to zero.

3.2.2 Topology optimization approaches

The topology optimization problem was initially approached with the homogenization method [34]. Since then, a large number of different methods have been developed. Among these are the density [35, 36, 37] and the evolutionary approaches [38] and boundary variation methods such as the level set [39, 40, 41] and the phase field [42] approach. It should be noted that according to some reviews, many of the approaches that claim to be new and different are but small variations on the same general method [43, 44].

Density based methods

The density approach uses a fixed mesh. The elements of this mesh are given a variable density that influences its properties [45]. By varying the density between 0 and 1 the design can be changed. In general if the density variable equals 1, the properties of the element correspond to the material properties that are used. If the density variable equals zero, the properties of the element equal the absence of the target material. The initial topology optimization approach, the homogenization approach was a density based approach. The major downside to the homogenization approach was that density variable allowed to vary continuously between 0 and 1. As a result, optimized designs also showed elements with densities varying between 0 and 1. In general these fictitious materials with intermediate densities do not have a physical equivalent. In order to remedy this flaw, the SIMP (Simplified Isotropic Material with Penalization) method was introduced [35]. This method uses a power-law penalty for the density to reduce the effectiveness of material with an intermediate density. The goal of this power-law penalty was to force the density to go to values of either 0 or 1. It has been noted that the SIMP method only works well when used in conjunction with some form of volume constraint or objective function, as this forces the optimization to use material as effectively as possible.

Evolutionary methods

The initial Evolutionary Structural Optimization (ESO) method only allowed for the removal of elements. Later a Bi-directional ESO (BESO) was proposed that also allowed for the addition of elements. Within the ESO/BESO methods two different categories exist [44]. The hard-kill method and the soft-kill method. Both methods use a design variable that is only allowed to be either 0 or 1, where 0 represents the absence and 1 the presence of an element. For the hard-kill method, if the variable is 0, the element is completely removed from the model. The removal criteria was generally heuristic and based on for instance which element had the lowest stress. When using the soft-kill BESO, an element is not completely removed, but instead replaced by a very soft element. The retention of the void element in the model allows for the use of analytical sensitivities with respect to the densities to determine which elements are added or removed. Recently, methods were proposed that used a penalized density measure similar to the SIMP density-based method. The similarities are present to such an extent that it is argued that the BESO approach should not be categorized as a separate approach, but rather seen as a discrete update version of the SIMP scheme [43]. The BESO approach has also been criticized for failing in certain situations caused by the discrete density updates and for a lack of algorithmic convergence [43].

Boundary variation methods

The level set and the phase field approaches are similar in many aspects [44]. Both approaches can be categorized as boundary variation methods. A boundary variation method approaches

the topology optimization problem from a shape optimization perspective. The methods use implicit functions that define the structural boundaries as opposed to an explicit parametrization of the entire design domain [44]. The major difference setting these methods apart from shape optimization is the ability to not only move the boundary, but also to create or remove void regions. The most prominent developing boundary variation techniques are the level-set method and the phase field method. The major benefit of boundary variation methods is that they produce clear boundaries as opposed to the boundaries produced by density based methods. However, boundary variation methods have been criticized for their difficulty in forming manufacturing constraints and ensuring fast and stable convergence behavior [46].

3.2.3 Complications and limitations

Topology optimization can be a powerful tool in developing new designs. However, the methods is not without its disadvantages. Forming adequate and accurate objective functions and constraints can be difficult. If the user has multiple objectives, the objective function needs include all different objectives. Difficulties can arise if the objectives are abstract or complex. For instance, a seemingly simple objective of reducing the costs of a structure might be accomplished by optimizing the material volume used in the design. However, this could lead to designs that are very difficult to construct, inadvertently increasing the construction costs.

The second disadvantage follows from the nature of structural optimization to optimize specifically for the supplied objective function and constraints. If the design is optimized for a single load condition (e.g. point load), performance of the design could vary wildly when even small adjustments are made to the load condition. It is therefore often necessary to supply multiple load conditions. It then befalls the user to choose whether to optimize for average performance over the load conditions, for the worst performing load condition or perhaps a different option. The selection of load conditions is limited by the computation time. Each added load condition requires an additional equilibrium to be solved, greatly increasing computation time.

Apart from these difficulties, the modelling of the structure introduces its own problems when combined with structural optimization. Because of the mathematical form of the problem, the structural optimization is prone to producing optimized designs that are physically impossible, but perform better according to the numerical model. Methods exist to ensure a physically realizable design when the optimization has converged. These methods are often not completely sufficient. If this is the case, a post-processing is required to ensure a fully physically possible design.

Part III

Method

Chapter 4

Finite Element Method

In order to achieve the goals of this thesis, the construction of a topology optimization tool for wave barriers is required. In chapter 3, four basic elements of a topology optimization problem were discussed: objective function, design variables, state variables and constraints. The constraints included behavioral constraints, design constraints and equilibrium constraints. In this thesis the equilibrium constraints were applied using a nested formulation. The state variables (the displacements) are determined from the design variables (the densities) by applying the equilibrium constraints using the finite element method. The objective function then uses the state variables to determine the quality of the wave barrier design at each iteration. In this chapter the construction, the validation and the limitations of the finite element model used to determine the state variables are discussed. Section 4.1 shows the general outline of the model and element type that were used. Section 4.2 shows the type of soil model that was used. Section 4.3 discusses the boundary layer used in the model. Section 4.4 gives a more in-depth explanation of the chosen geometries and the reasoning behind them. In section 4.5, the model will be validated. As will become clear in chapter 5, the displacement amplitudes are sufficient for determining the wave barrier effectiveness. As such, the FEM analysis will be limited to a frequency domain analysis.

4.1 Model

The general soil model consists of two parts. An inner domain to model the propagation of waves and a boundary layer to prevent the reflection of waves at the edges of the model. The optimization process is enabled by dividing the inner domain into a passive soil domain and a design domain (see figure 4.1). The passive soil domain is dependent solely on the properties of the modelled soil. In contrast, the design domain is dependent on the properties of the soil, the barrier material and the design density variables. These density variables can be changed during the optimization process to influence the wave propagation. This will be discussed in more detail in chapter 5.

The model was constructed using 2D four-noded quadrilateral elements. The choice for this element type was based largely on the required computation time. This is especially important because the optimization process requires a large number of evaluations of the model. The lower order elements used here have a lower number of degrees of freedom, allowing for a higher resolution than would be feasible with higher order elements. A higher resolution is preferred in the design domain as it allows the boundaries of the design to more accurately approach non-rectangular shapes.

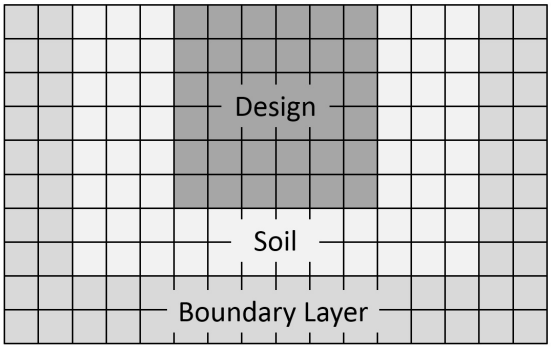

Figure 4.1: Mesh example

Only the properties of the elements in the design domain vary throughout the optimization process. The result is that only a relatively small part of the dynamic stiffness matrix changes during the iterations, while a large part remains the same. The matrix can therefore be split into two systems of equations [47]:

$$\begin{bmatrix} \mathbf{S}_{ss} & \mathbf{S}_{sd} \\ \mathbf{S}_{ds} & \mathbf{S}_{dd} \end{bmatrix} \begin{bmatrix} \hat{\mathbf{u}}_s \\ \hat{\mathbf{u}}_d \end{bmatrix} = \begin{bmatrix} \hat{\mathbf{P}}_s \\ \hat{\mathbf{P}}_d \end{bmatrix} \tag{4.1}$$

Here subscript s denotes the DOF of the surrounding domain, which includes both the surrounding passive soil elements and the boundary layer. Subscript d denotes the DOF of the design domain. In equation 4.1, only the term $\mathbf{S}_{dd}$ is dependent on the density variables. The first system of equations is therefore independent of the density variables and can be written as:

$$\hat{\mathbf{u}}_s = \mathbf{S}_{ss}^{-1}\hat{\mathbf{P}}_s - \mathbf{S}_{ss}^{-1}\mathbf{S}_{sd}\hat{\mathbf{u}}_d \tag{4.2}$$

Inserting this into the second system of equations gives:

$$\left(\mathbf{S}_{dd} - \mathbf{S}_{ds}\mathbf{S}_{ss}^{-1}\mathbf{S}_{sd}\right)\hat{\mathbf{u}}_d = \hat{\mathbf{P}}_d - \mathbf{S}_{ds}\mathbf{S}_{ss}^{-1}\hat{\mathbf{P}}_s \tag{4.3}$$

During the optimization process the most expensive calculations are those concerning the FEA. In order to reduce the computational time reserved for these calculations, $\mathbf{S}_{ss}^{-1}\hat{\mathbf{P}}_s$ and $\mathbf{S}_{ss}^{-1}\mathbf{S}_{sd}$ are determined before starting the iterations. During the iterations, only the much smaller system from equation 4.3 must be solved for $\hat{\mathbf{u}}_d$. The displacements $\hat{\mathbf{u}}_s$ from equation 4.2 can then be solved using computationally inexpensive matrix multiplication. For a single calculation this approach is a lot more time consuming, but because $\mathbf{S}_{ss}^{-1}\hat{\mathbf{P}}_s$ and $\mathbf{S}_{ss}^{-1}\mathbf{S}_{sd}$ only have to be determined once at the start of the optimization process, this approach significantly reduces the required computation time if many iterations are required.

4.2 Soil model

A linear elastic plane strain model with hysteretic damping was used in this thesis. This section discusses the reasons for these choices.

4.2.1 Linear elasticity

With the exception of a small area directly underneath the track, the strain levels resulting from railway-induced waves are relatively low. The soil itself is always under compression, except at

the surface. If the soil experiences tension, linear elasticity is no longer a valid approximation. Therefore, as long as the strain levels resulting from the wave are low, the soil will only experience tension at a very small distance beneath the surface, which can be neglected for waves of large wavelength relative to the depth in tension. Furthermore, even in situations where inelastic behavior of the track subgrade is of significant importance, such as for high speed trains on tracks supported by a very soft soil, the inelastic behavior is argued to have little impact on the vibration levels further away from the track [48]. When modelling the soil response it is therefore sufficient to assume linear elastic behavior of the soil.

4.2.2 Plane strain

The only degrees of freedom taken into account in the 2D model are horizontal and vertical displacements. As a result, the constitutive matrix can be reduced. This is done by assuming that the strain in the direction normal to the considered plane is zero. The accompanying plane strain constitutive matrix can be given in the form:

$$\mathbf{D} = \begin{bmatrix} (\lambda + 2\mu) & \lambda & 0 \\ \lambda & (\lambda + 2\mu) & 0 \\ 0 & 0 & \mu \end{bmatrix} \tag{4.4}$$

With:

$$\lambda = \frac{E\nu}{(1+\nu)(1-2\nu)} \tag{4.5a}$$

$$\mu = \frac{E}{2(1+\nu)} \tag{4.5b}$$

4.2.3 Hysteretic damping

Different damping models are available. Viscous damping is one of the most common damping models. For propagating waves, a viscous damping model results in an amplitude decay that is constant over distance and independent of frequency. Investigations of damping in soil found that the amplitude decay appeared to be constant per wave length. A viscous damping model would not accurately represent the phenomenon. A more accurate representation of the damping observed in soil is the hysteretic damping model [24]. A hysteretic damping model can be implemented by multiplying the Lamé parameters with a complex damping coefficient [49], resulting in:

$$\lambda^* = \lambda(1 + 2i\eta_d) \tag{4.6a}$$

$$\mu^* = \mu(1 + 2i\eta_d) \tag{4.6b}$$

The adapted constitutive matrix then takes the form:

$$\mathbf{D}^* = \begin{bmatrix} (\lambda^* + 2\mu^*) & \lambda^* & 0 \\ \lambda^* & (\lambda^* + 2\mu^*) & 0 \\ 0 & 0 & \mu^* \end{bmatrix} \tag{4.7}$$

It should be noted that the functions used to determine wave barrier effectiveness consisted of reduction ratios. Initial optimization tests showed that as a result, the damping ratio had very little influence on the overall results. In addition, depictions of the displacements more clearly displayed the phenomena when the damping ratio was set to 0. As such, this was the value used throughout this thesis for all soils.

4.3 Perfectly matched layer

4.3.1 Background

For the problems that are considered, the dimension of the soil are nearly infinite in comparison to the wavelengths. An essential condition of the model is therefore the absence of reflections. Multiple options exist that approach the zero reflection condition. Among these options are methods based on boundary integral equations, infinite element methods, non-reflecting boundary conditions and absorbing layers. The perfectly matched layer (PML) is an example of an absorbing layer. The method is named after its ability to perfectly match the inner domain of the model. Most absorbing boundary layers change parameters in small increments to reduce the reflections caused by the interface. In contrast, in its analytical form, the perfectly matching property of the PML ensures the absence of reflections at the interface by perfectly matching the boundary layer to the inner domain. The amplitude of a wave decays as it propagates through the PML. Then, after the wave reflects from the edges of the model, it decays further still as it propagates back towards the inner domain. If the parameters of the PML are chosen correctly, the reflected waves are damped to such an extent that their amplitude is negligible as they re-enter the inner domain [50].

PMLs have several advantages over other absorbing or non-reflective boundaries [51]. The PMLs are relatively simple to implement. They can be applied to a great number of equations without much additional complexity (including acoustics, electromagnetism and elastodynamics). They also provide remarkable performances in many applications, even when the theory does not completely predict it. However, despite their advantages, the PMLs are not perfect. One of the relevant disadvantages is that the material in the layers must be invariant in the direction normal to the interface [52]. Additionally, under certain conditions, the PML can fail completely [53]. The conditions under which this occurs and a measure to control for this failure are discussed in subsection 4.3.4. First the construction and implementation of the PML is discussed.

4.3.2 Construction

PMLs can be constructed in multiple ways. The most intuitive method is through complex coordinate stretching [52]. This method involves three steps.

- Analytic continuation of the solution and equations to a complex x contour.
- Coordinate transformation back to the real x.
- Truncating the domain.

The three steps are illustrated using a plane wave travelling in the x-direction:

$$W(y,z)\, e^{i(\omega t - kx)}$$

Analytical continuation of x into the complex domain yields:

$$e^{-ik\,x} = e^{-ik(\mathrm{Re}\{x\} + i\,\mathrm{Im}\{x\})} = e^{-ik\,\mathrm{Re}\{x\}}\, e^{k\,\mathrm{Im}\{x\}}$$

Assuming $k > 0$, if $\mathrm{Im}\{x\} < 0$, the result leads to an exponentially decaying function with increasing x.

The next step is to transform the complex formulation back to the real x. If the stretched coordinate is assumed as $\tilde{x}(x) = x + if(x)$, where $f(x)$ is a function indicating how the coordinate is stretched, the only thing that is needed is formulating the change of $\tilde{x}$ as a function of x. The result is:

$$\delta\tilde{x} = \left(1 + i\frac{df}{dx}\right)\delta x$$

As the PML is assumed to be located in $x \in [0, L]$, the plane wave becomes:

$$W(y,z)\, e^{-ik\left(\int^x 1 + i\frac{df}{dx}(\hat{x})\, d\hat{x}\right)} = e^{-ik\,x}\, e^{\frac{k}{\omega}\int^x \frac{df}{dx}(\hat{x})\, d\hat{x}}$$

Then $\frac{\sigma_x}{\omega}$ is taken for $\frac{df}{dx}$. The equation for the plane wave becomes:

$$W(y,z)\, e^{-ik\,x}\, e^{\frac{k}{\omega}\int^x \sigma_x(\hat{x})\, d\hat{x}} = W(y,z)\, e^{-ik\,x}\, e^{\frac{1}{c_p}\int^x \sigma_x(\hat{x})\, d\hat{x}}$$

It can be easily seen that the wave will decay if $\sigma_x < 0$. Furthermore, the attenuation depends on the phase velocity. In a dispersionless material the phase velocity is a constant. The effect of this is that the attenuation is independent of frequency. All wavelengths decay at the same rate.

The last step involves truncating the domain. When the PML is formed starting from a certain point in the model, the solution is unchanged before that point and exponentially decays after that point. It then becomes possible to use boundary conditions (for instance Dirichlet boundary conditions) at the end of the PML.

4.3.3 Implementation

The implementation of the PML was done according to the method of Harari and Albocher [54]. This method uses an anisotropic formulation, which allows for relatively easy implementation into a finite element program.The mass matrix inside the PML is obtained by multiplying the integrand of the mass matrix of the elastic medium by the stretch functions. These stretch functions are of the form:

$$\psi_j = 1 + is_j \tag{4.8}$$

With the subscript j indicating a direction corresponding to an axis. Where s_j is an attenuation function that is determined by a set of parameters and is a function of the distance from the interface. For the mass matrix this yields:

$$\tilde{\mathbf{m}}_\mathbf{e} = \mathbf{1}\int_{\Omega_e} N^T\psi_1\psi_2\rho N d\Omega \tag{4.9}$$

Where N is the shape function of the element, Ω the domain occupied by the element and ρ density of the element. For the stiffness matrix, the matrix containing the derivatives of the shape functions and the constitutive matrix are adapted.

$$\tilde{\mathbf{k}}_\mathbf{e} = \int_{\Omega_e} \tilde{B}^T\tilde{D}\tilde{B} d\Omega \tag{4.10}$$

With:

$$\tilde{\mathbf{B}} = \begin{bmatrix} N_{1,1} & 0 & \cdots & N_{4,1} & 0 \\ 0 & N_{1,2} & \cdots & 0 & N_{4,2} \\ N_{1,2} & N_{1,1} & \cdots & N_{4,2} & N_{4,1} \\ N_{1,2} & -N_{1,1} & \cdots & N_{4,2} & -N_{4,1} \end{bmatrix} \tag{4.11}$$

$$\tilde{\mathbf{D}} = \begin{bmatrix} (\lambda^* + 2\mu^*)\frac{\psi_2}{\psi_1} & \lambda^* & 0 & 0 \\ \lambda^* & (\lambda^* + 2\mu^*)\frac{\psi_2}{\psi_1} & 0 & 0 \\ 0 & 0 & \frac{\mu^*}{4}(\frac{\psi_1}{\psi_2} + \frac{\psi_2}{\psi_1} + 2) & \frac{\mu^*}{4}(\frac{\psi_1}{\psi_2} - \frac{\psi_2}{\psi_1}) \\ 0 & 0 & \frac{\mu^*}{4}(\frac{\psi_1}{\psi_2} - \frac{\psi_2}{\psi_1}) & \frac{\mu^*}{4}(\frac{\psi_1}{\psi_2} + \frac{\psi_2}{\psi_1} - 2) \end{bmatrix} \tag{4.12}$$

Attenuation function

The attenuation function s_j is a function of the distance from the interface and a set of parameters. Consider a wave with wave number k propagating at an angle θ with respect to the x-axis. If the layer width is L, the reflection coefficient becomes [55]:

$$R = exp(-2kcos(\theta) \int_0^L s(x)dx) \tag{4.13}$$

At first sight, it seems most prudent to make the reflection coefficient as low as possible. Ineed, in a continuous setting this would be possible as the PML is, as its name suggests, perfectly matching and does not cause a reflection when waves enter the layer. However, when the PML is discretized it loses that property [56]. It then becomes necessary to slowly increase the attenuation factor. Guidelines suggest s_j, to at least be of second order [56]. Here a quadratic profile is used as suggested by Harari and Albocher [54]:

$$s(x) = s_{max} \left(\frac{x}{L}\right)^2, \quad 0 < x < L \tag{4.14}$$

Inserting (4.14) into equation (4.13) gives:

$$R = exp\left(\frac{-2kLs_{max}cos(\theta)}{3}\right) \tag{4.15}$$

Equation (4.15) can then be rearranged to give an expression for s_{max}:

$$s_{max} = \frac{-3ln(R)}{2kLcos(\theta)} \tag{4.16}$$

The choice for s_{max} depends on the angle between propagation direction and interface (θ), the wave number (k), the thickness of the PML (L) and the desired reflection coefficient (R). As stated previously, the PML loses some of its properties due to the discretization. This is seen when choosing a reflection coefficient as well. As can be expected, choosing a large reflection coefficient results in larger reflections. However, choosing a reflection coefficient that is too small can lead to spurious reflections at the boundary. Harari and Albocher [54] suggest taking a reflection coefficient that depends on the accuracy of the mesh. For instance, for an accuracy of 10^{-2}, a reflection coefficient of $10^{-4} \leq R \leq 10^{-3}$ is recommended. For the wave number a choice must be made between the longitudinal (k_p) and the transverse (k_s) wave number.

$$k_p = \sqrt{\frac{\rho\omega^2}{\lambda + 2\mu}}, \quad k_s = \sqrt{\frac{\rho\omega^2}{\mu}}, \tag{4.17}$$

From (4.17) it can be derived that, in the case of plane strain:

$$k_s = k_p\sqrt{\frac{2 - 2\nu}{1 - 2\nu}}. \tag{4.18}$$

When assuming reasonable values for ν:

$$\sqrt{2}k_p \leq k_s \leq \sqrt{6}k_p \quad for: \quad 0 \leq \nu \leq 0.4 \tag{4.19}$$

The transverse wave number was considered an appropriate 'middle-ground' to use for the determination of the attenuation function.

While optimizing, the wave propagation angles are not known in advance. Harari and Albocher [54] stated that an angle may be assumed without compromising the results because the choice of reflection coefficient was more influential. Harari and Albocher [54] assumed a value for θ, such that $\cos\theta = 0.5$ and the same approach will be applied here. For the reflection coefficient a value of $R = 1e^{-6}$ was chosen, resulting in the attenuation function:

$$s(x) = s_{max}\left(\frac{x}{L}\right)^2 \quad \text{with:} \quad s_{max} = \frac{18}{k_s L} \qquad 0 < x < L \tag{4.20}$$

4.3.4 Possible failure of PML

The beginning of this section briefly mentioned the possibility of the PMLs to fail under certain conditions. Specifically, a PML fails when both backward and forward propagating waves occur in the model. Backward propagating waves are characterized by opposite signs for the group velocity (v_g) and the phase velocity (v_p). This would indicate that the energy of the wave is travelling in the opposite direction of the peaks of the phase velocity of a single wave. How this causes failure follows logically from the way the PMLs are constructed.

In order to show this we return to a travelling wave of the form $W(y,z)e^{[}i\,(t-(k/\omega)x)]$. Applying the complex coordinate stretching and transformation back to the real x results in:

$$W(y,z)e^{i(t-(k/\omega)x)}e^{(df/dx)(k/\omega)x} = W(y,z)e^{i(t-(1/v_p)x)}e^{(df/dx)(1/v_p)x}$$

where v_p is the phase velocity. It can now be seen that for backward waves ($v_g > 0$ and $v_p < 0$), a wave travelling in the $+x$-direction ($v_g > 0$) will experience exponential growth instead of decay for $df/dx < 0$. If only backward waves exist, this can be remedied by taking $df/dx > 0$. However, if both backward and forward propagating waves occur simultaneously, there will always be one that grows exponentially. In the model of this thesis each FEA determines the displacement amplitudes of a single harmonic load. Three types of waves exist in the 2D model. Primary (compression) waves, secondary (shear) waves and Rayleigh waves. In layered soil, the Rayleigh waves are dispersive. The phase velocity of the Rayleigh waves is a function of the wave number. The result is that frequencies and soil properties can exist in which the group velocity becomes negative. If this occurs, the presence of the primary and secondary waves ensures that, regardless of the choice for df/dx, there are waves that will experience exponential growth in the PML. The phase velocity and group velocity over the frequency range can be observed from a dispersion curve (chapter 2, subsection 2.4.3). If the dispersion curve of a soil model shows that the signs of the two velocities differ over a certain frequency range, the FEA for those frequencies would not be accurate. This has consequences for the optimization process in that these frequencies can not be included in the objective function. Fortunately, the optimization process uses a discretization over the frequency range and careful selection of the considered frequencies would allow the user to avoid the frequency range for which the PML is expected to fail.

4.4 Model geometry

Figure 4.2 shows the model used throughout this thesis. The relative distances between the load and the design domain (x_{FD}) and the design domain and the receiver area (x_{DR}) as well as the

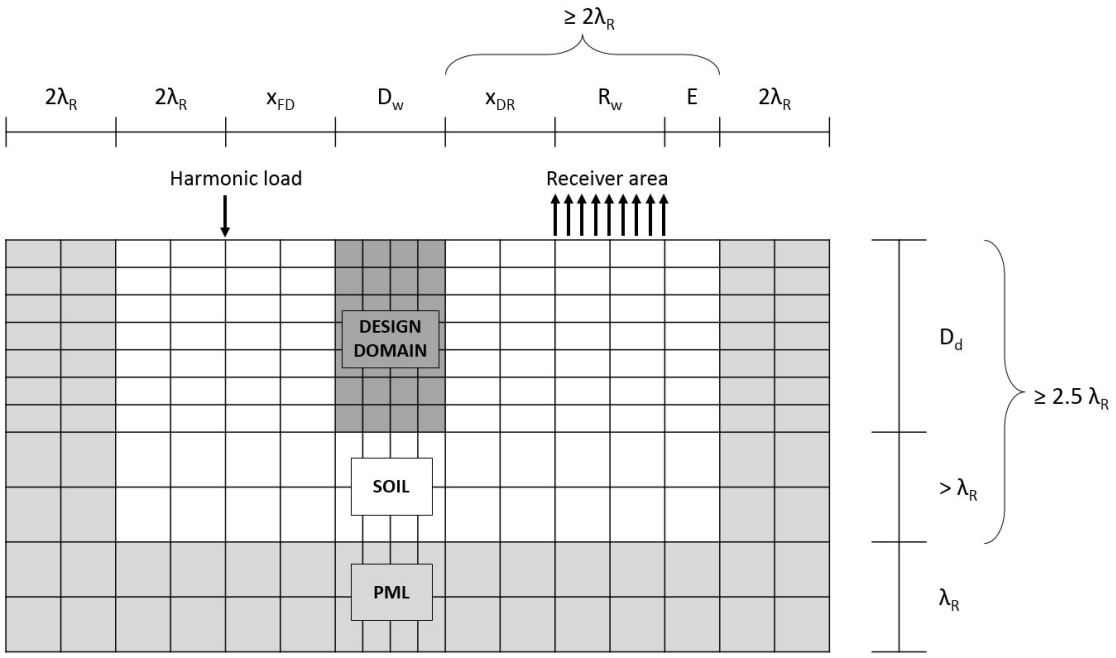

Figure 4.2: The geometry of the model, dependent on user input and Rayleigh wavelength (λ_R)

width (D_w) and depth (D_d) of the design domain and the width of the receiver area (R_w) depend on user input. The size of the inner domain as a whole is dependent on the maximum possible Rayleigh wavelength (λ_R). The depth from surface up to the PML is equal to or greater than 2.5 times λ_R. This is based on the graph of the displacements over depth of a Rayleigh wave in chapter 2, which showed that the displacements associated with a Rayleigh wave are significant up to this depth. Additionally, the minimum distance between the depth of the design domain to the start of the PML is taken as equal to or greater than $1\lambda_R$. The horizontal distance between the load and the PML, as well as the minimum distance between the edge of the design domain to the PML are set to equal $2\lambda_R$. This is based on the PML performance for interfaces close to the load. As will be demonstrated in the next section, loads close to the PML can lead to spurious reflections. The variable E is either set to 1 element to ensure that the receiver area is not in contact with the PML, or more elements to ensure that the minimum distance between the design domain and the PML is equal to or greater than $2\lambda_R$.

In the following chapters, different soil models will be used. Figures depicting the model geometries will only show the inner domain and will focus on the interrelated distances of the load, design domain and receiver, the depth of soil layer interfaces and the design area geometry. The wavelength dependent distances from figure 4.2 will be maintained throughout the thesis and are therefore omitted from this point onward.

Figure 4.2 also shows that the elements sizes were allowed to differ. In the design domain the resolution was fixed, and dependent on the desired resolution as well as the smallest wavelength expected to appear in the model. The optimization process forces the design variables to be the same across the different frequencies, and thus also the design domain mesh needs to be the same. Outside the mesh, the element sizes were allowed to vary based on the wavelengths. The maximum element size was determined based on a convergence study with Lamb's problem, which is discussed further in the next section.

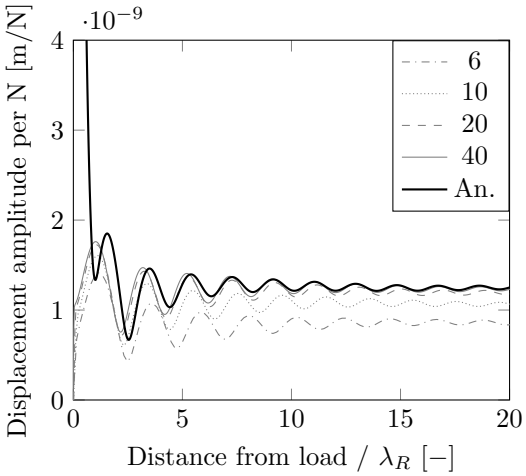

Figure 4.3: Horizontal displacement amplitude at surface calculated numerically with increasing number of elements per wavelength compared with the analytical approximation of the integral.

4.5 Validation

The FEM model is validated in three stages. First the FEM model is compared to the analytical solution to Lamb's problem (see section 2.3.3 on page 19 for the derivation of the analytical solution). Due to the asymptotic expansion used to arrive at the solution, the analytical solution is only valid for the far field. In order to validate the FEM model for the near field, a semi-analytical solution to Lamb's problem is used. Both the analytical and the semi-analytical solutions are only valid for a homogeneous soil model. However, if the FEM model is valid for a homogeneous soil model, the only concern regarding the accuracy of the model for an inhomogeneous soil model is the performance of the PML. To evaluate this performance the distance between the PML interface and the load is varied and the resulting displacements are compared.

4.5.1 Lamb's Problem: Analytical solution

The analytical solution to Lamb's Problem for a harmonic infinite line load will serve two purposes in this validation. First it will be used to validate the model that was used, second it will be used as a guideline for the element size. In general there is consensus that the maximum element size should be dependent on the wavelength of the modelled problem. The exact size of the element relative to the wavelength is a point of some discussion. Recommendations often vary between 6 and 10 elements per wavelength [57]. The previous studies into the effectiveness of wave barriers used a minimum resolution of 8 elements per smallest possible wavelength [19, 58].

In order to determine the maximum allowed element size used in this thesis, the numerical solution for the displacement amplitudes at the surface are compared to the analytical solution found by Lamb [30]. The results for the horizontal and vertical displacement amplitudes can be found in figures 4.3 and 4.4 respectively. In these figures it becomes clear that the FEM model converges with the analytical solution in the far field. The very fine mesh appears to have an almost perfect agreement with the analytical solution.

After considering the convergence visible in figures 4.3 and 4.4 a minimum element size corre-

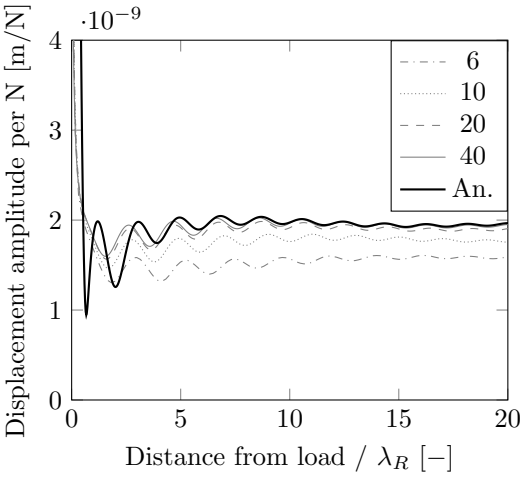

Figure 4.4: Vertical displacement amplitude at surface calculated numerically with increasing number of elements per wavelength compared with the analytical approximation of the integral.

sponding to 20 elements per wavelength was preferred. However, because the FEM calculations will occur many times throughout the optimization process, the computational time must be taken into account as well. The resolution of the design domain is required to be constant for all considered frequencies. This resolution in turn determines the element height or width for a large part of the model (figure 4.2). If the resolution for the higher frequencies is taken as 20 elements per wavelength, this would have significant consequences for the calculation time for the lower frequencies. As a result, some concessions must be made in terms of accuracy in order to reduce the computational time for the lower frequencies. For this thesis the minimum element size in the design domain is taken as 0.125 m × 0.125 m. For softer soils at higher frequencies that produce a Rayleigh wavelength of 1.25 m, this results in 10 elements per wavelength. For all element sizes not dependent on those of the design domain, a minimum element size of 10 elements per wavelength is used.

4.5.2 Lamb's problem: Semi-analytical solution

The semi-analytical solution to Lamb's problem consists of a numerical integration of an analytically derived integral. The numerical integration requires two changes compared to the analytical solution. The numerical integration has difficulty converging for the surface displacements, therefore the displacements must be determined at a certain depth below the surface. The numerical integration also requires a damping coefficient greater than zero. These changes result in integrals that differ slightly from the ones determined in section 2.3.3 as those integrals were valid for $z = 0$. Similar to previously, the approach starts by assuming a distributed load. The Helmholtz decomposition is used once more for the displacements in 2D:

$$\begin{aligned} u &= \frac{\delta\phi}{\delta x} - \frac{\delta\psi}{\delta z} \\ w &= \frac{\delta\phi}{\delta z} + \frac{\delta\psi}{\delta x} \end{aligned} \tag{4.21}$$

The general solutions for ϕ and ψ are also used again (equation 2.25):

$$\begin{aligned}\phi &= Ae^{\left(-k\sqrt{1-\frac{c^2}{c_p^2}}z\right)}e^{ik(ct-x)}\\ \psi &= Be^{\left(-k\sqrt{1-\frac{c^2}{c_s^2}}z\right)}e^{ik(ct-x)}\end{aligned} \tag{4.22}$$

The boundary conditions for the stress at the surface remain the same:

$$\begin{aligned}[\sigma_{zz}]_{z=0} &= \lambda\left(\frac{\delta^2\phi}{\delta x^2}+\frac{\delta^2\phi}{\delta z^2}\right)+2\mu\left(\frac{\delta^2\phi}{\delta z^2}+\frac{\delta^2\psi_2}{\delta x\delta z}\right)=Ye^{ikx}\\ [\sigma_{xz}]_{z=0} &= \mu\left(2\frac{\delta^2\phi}{\delta x\delta z}+\frac{\delta^2\psi_2}{\delta x^2}-\frac{\delta^2\psi_2}{\delta z^2}\right)=0\end{aligned} \tag{4.23}$$

By inserting the general solutions for ϕ and ψ into the boundary conditions, expressions for A and B can be derived. Using these expression for A and B and inserting the general solutions into the expressions for the displacements results in the following expressions:

$$\begin{aligned}u &= \frac{ik\left(\left(k^2+\beta^2\right)e^{-\alpha z}-2\alpha\beta e^{-\beta z}\right)}{k^4\lambda-k^2\alpha^2\lambda+k^2\beta^2\lambda-2k^2\alpha^2\mu+4k^2\alpha\beta\mu-\alpha^2\beta^2\lambda-2\alpha^2\beta^2\mu}Ye^{ikx}\\ w &= \frac{\left(k^2+\beta^2\right)\alpha e^{-\alpha z}-2k^2\alpha e^{-\beta z}}{k^4\lambda-k^2\alpha^2\lambda+k^2\beta^2\lambda-2k^2\alpha^2\mu+4k^2\alpha\beta\mu-\alpha^2\beta^2\lambda-2\alpha^2\beta^2\mu}Ye^{ikx}\end{aligned} \tag{4.24}$$

Here $\alpha=\sqrt{k^2-k_p^2}$, $\beta=\sqrt{k^2-k_s^2}$ and λ and μ are Lamé parameters. Using the same approach as in chapter 2, a concentrated force Q is evaluated by writing: $Y = Q\,dk/2\pi$ and integrating with respect to k from $-\infty$ to $+\infty$:

$$\begin{aligned}u &= \frac{Q}{2\pi}\int_{-\infty}^{\infty}\frac{ik\left(\left(k^2+\beta^2\right)e^{-\alpha z}-2\alpha\beta e^{-\beta z}\right)}{k^4\lambda-k^2\alpha^2\lambda+k^2\beta^2\lambda-2k^2\alpha^2\mu+4k^2\alpha\beta\mu-\alpha^2\beta^2\lambda-2\alpha^2\beta^2\mu}e^{ikx}\,dk\\ w &= \frac{Q}{2\pi}\int_{-\infty}^{\infty}\frac{\left(k^2+\beta^2\right)\alpha e^{-\alpha z}-2k^2\alpha e^{-\beta z}}{k^4\lambda-k^2\alpha^2\lambda+k^2\beta^2\lambda-2k^2\alpha^2\mu+4k^2\alpha\beta\mu-\alpha^2\beta^2\lambda-2\alpha^2\beta^2\mu}e^{ikx}\,dk\end{aligned} \tag{4.25}$$

These expression are rewritten using symmetry to allow for integration from 0 to ∞:

$$\begin{aligned}u &= \frac{2Q}{2\pi}\int_{0}^{\infty}\frac{ik\left(\left(k^2+\beta^2\right)e^{-\alpha z}-2\alpha\beta e^{-\beta z}\right)}{k^4\lambda-k^2\alpha^2\lambda+k^2\beta^2\lambda-2k^2\alpha^2\mu+4k^2\alpha\beta\mu-\alpha^2\beta^2\lambda-2\alpha^2\beta^2\mu}i\sin ikx\,dk\\ w &= \frac{2Q}{2\pi}\int_{0}^{\infty}\frac{\left(k^2+\beta^2\right)\alpha e^{-\alpha z}-2k^2\alpha e^{-\beta z}}{k^4\lambda-k^2\alpha^2\lambda+k^2\beta^2\lambda-2k^2\alpha^2\mu+4k^2\alpha\beta\mu-\alpha^2\beta^2\lambda-2\alpha^2\beta^2\mu}\cos ikx\,dk\end{aligned} \tag{4.26}$$

These expressions were numerically integrated using a script provided by Dr. Ir. K.N. van Dalen. A comparison between the resulting displacements at $z = 0.75\,\text{m}$ and the results from the FEM model is depicted in figures 4.5 and 4.6 for the horizontal and vertical displacements respectively. It is now clear that the FEM solution shows convergence in the near field as well. However, the effects seen in the comparison to the analytical solution persist. There is still a significant improvement in the accuracy of the solution when increasing the number of elements per wavelength from 10 to 20.

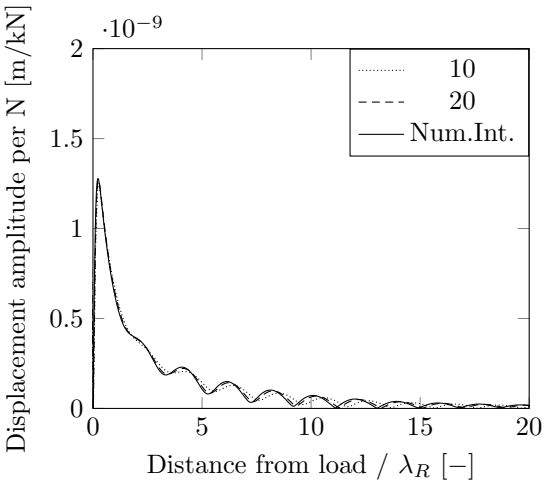

Figure 4.5: Horizontal displacement amplitude at surface calculated numerically with increasing number of elements per wavelength compared with the numerical integration of the integral.

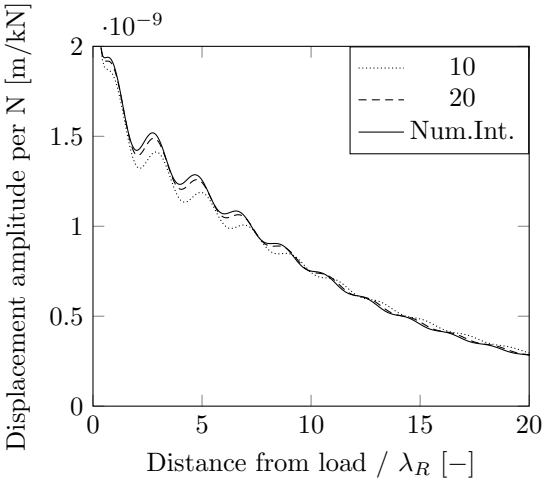

Figure 4.6: Vertical displacement amplitude at surface calculated numerically with increasing number of elements per wavelength compared with the numerical integration of the integral.

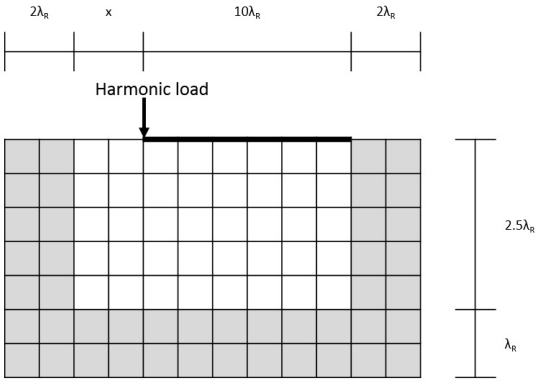

Figure 4.7: Model used to validate the PML. Surface displacements to the right of the harmonic load were compared for different values for the variable x.

4.5.3 Validation layered soil model

Lamb's problem is valid for a homogeneous soil model. The introduction of a layered soil model only consists of changing the properties of the elements in the model. For the inner domain simply changing the properties of a selection of elements should have no effect on the accuracy of the model. However, the continued performance of the PML as an absorbing boundary layer was still of some concern in a layered soil.

Aside from the possibility of failure due to backward and forward travelling waves, the performance of the model can also suffer from spurious reflections at the interface of the PML if the parameters are not chosen properly [54]. The ability of the PML to simulate an infinite domain in a layered soil profile will be validated here by comparing the displacements at the surface of models with varying distances between the PML and the load (see figure 4.7). The underlying thought process is that, if the PML does not accurately simulate an infinite domain, the location of the interface would have an effect on the displacements. Then if the distance between the PML and the load varies, the displacements found in the inner domain would as well.

A layered soil profile was used, based on experimental cone penetration tests (table 4.1). The only parameter that was changed was the damping coefficient in order to avoid amplitude decay influencing possible spurious reflections.

Figure 4.8 shows the displacements at the surface for a model with the interface at a distance of $0.5\lambda_R$, $1\lambda_R$, $2\lambda_R$ and $4\lambda_R$ from the load. Here λ_R represents the maximum possible Rayleigh wavelength. The difference in the absolute displacements is nearly impossible to discern with the naked eye. Figures 4.9 and 4.10 show the difference of the displacements at the surface for a model with the interface at different distances from the load in percentages. The figure shows relatively large differences between interface/load distances $0.5\lambda_R$ and $1\lambda_R$. The difference between $1\lambda_R$ and $2\lambda_R$ is much smaller, while the difference between $2\lambda_R$ and $4\lambda_R$ is smaller still. This seems to indicate that the performance of the PML suffers when the interface is located too close to the load. The maximum difference in vertical displacement amplitude between an interface located at $2\lambda_R$ and $4\lambda_R$ from the source was 0.4%. As a result, the model will use a minimum distance of twice the maximum possible Rayleigh wavelength between the interface and the load (see figure 4.2).

Layer	Max Depth (m)	E mod. ($10^6 N/m^2$)	Density (kg/m^3)	Poisson's ratio	Damping ($-$)
1	1.0	45.9	1800	0.48	0
2	2.0	36.0	1550	0.48	0
3	3.0	33.9	1300	0.49	0
4	4.0	20.7	1400	0.48	0
5	5.0	17.3	1400	0.48	0
6	6.0	52.6	1300	0.49	0
7	7.0	47.6	1300	0.49	0
8	8.0	45.0	1300	0.49	0
9	9.0	16.4	1400	0.48	0
10	10.0	19.3	1400	0.48	0
11	11.0	20.8	1400	0.48	0
12	12.0	18.0	1500	0.48	0
13	13.0	29.6	1900	0.45	0
14	14.0	94.2	2100	0.48	0
15	15.0	63.1	2000	0.48	0
16	16.0	411.0	2000	0.45	0
17	17.0	414.0	2000	0.45	0
18	18.0	215.0	1900	0.45	0
19	19.0	183.0	1900	0.45	0
HS		235.0	1900	0.45	0

Table 4.1: Soil properties of validation soil

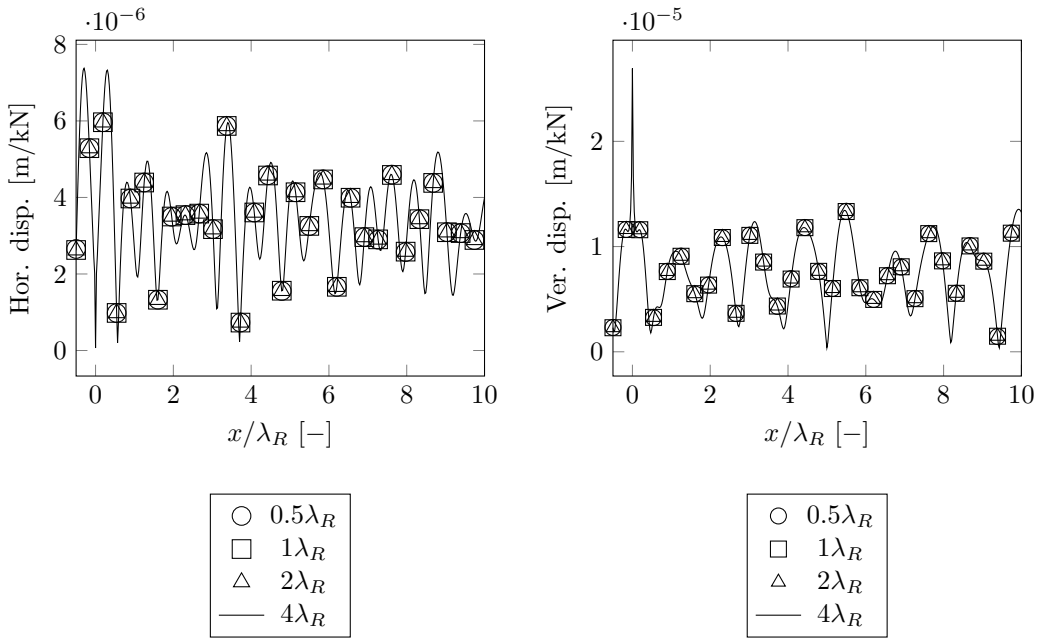

(a) Horizontal displacement amplitude

(b) Vertical displacement amplitude

Figure 4.8: Displacement amplitudes at the surface for different interface/load distances

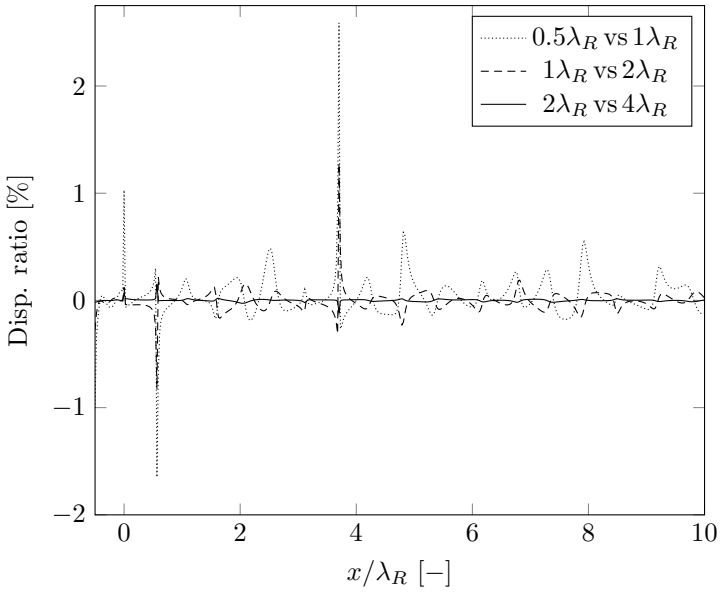

Figure 4.9: Horizontal displacement amplitude ratios between different interface/load distances in percentages

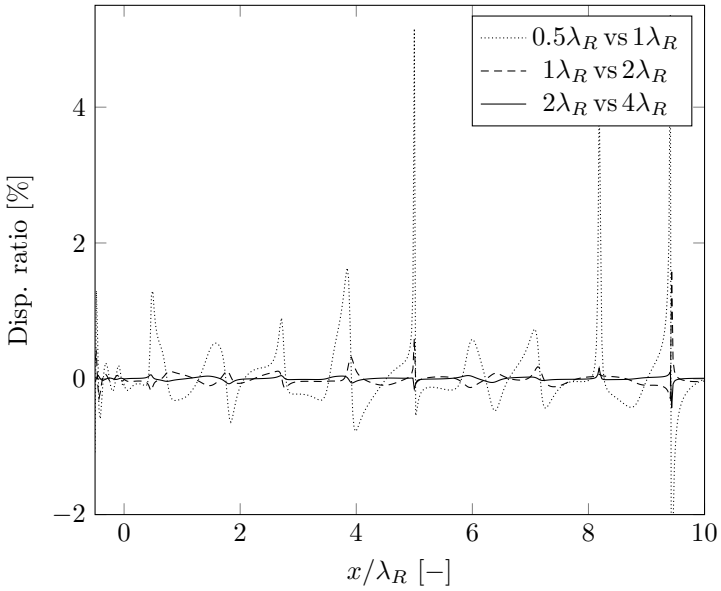

Figure 4.10: Vertical displacement amplitude ratios between different interface/load distances in percentages

Chapter 5

Topology optimization of wave barriers

5.1 Overview of optimization process

Part II discussed a few of the most prominent approaches to topology optimization. The boundary variation methods were criticized for the difficulty with which they could accommodate manufacturing constraints and their lack of reliable and stable convergence. The evolutionary methods were similar to regular density based methods, but lacked algorithmic convergence. Combining this with the fact that the density based method has already been successfully used for the optimization of wave barriers, it appears to be the optimal choice. This chapter focuses on the application of the density based approach to the topology optimization of wave barriers.

Like all other structural optimization methods, density based topology optimization is an iterative method (see figure 5.1). Before the process starts, initial values for the design variables must be supplied. In order to mitigate certain complications, these design variables are filtered. The resulting filtered variables are used to determine the material properties of the elements in the design domain in the FEA using an interpolation method called the Simplified Isotropic Material with Penalization (SIMP). The FEA returns the displacements at the receiver area under a user specified load for the current state of the wave barrier. These displacements are used to determine the values for the objective function (i.e. energy reduction), while the filtered densities are used to ensure that the constraints are not violated (i.e. whether or not maximum volume is exceeded). A sensitivity analysis then gives the sensitivity of the objective function and constraints to changes of each design variable. The information about the objective function, constraints and the sensitivities is then used by the optimization algorithm to determine an improved version of the design. After the design variables are updated the process returns to the filter step. In this chapter the steps shown in the flowchart are further elaborated.

5.2 Three-field SIMP

While density based topology optimization is a useful tool for finding optimal designs, it is not without complications. If not properly accounted for, designs can suffer from mesh-dependence, checkerboard designs and "gray" areas [45]. Mesh-dependence is problematic because different mesh sizes can lead to qualitatively different designs. A common form of this problem is an increased number of holes for a finer mesh. In general, a structure becomes stiffer when a volume

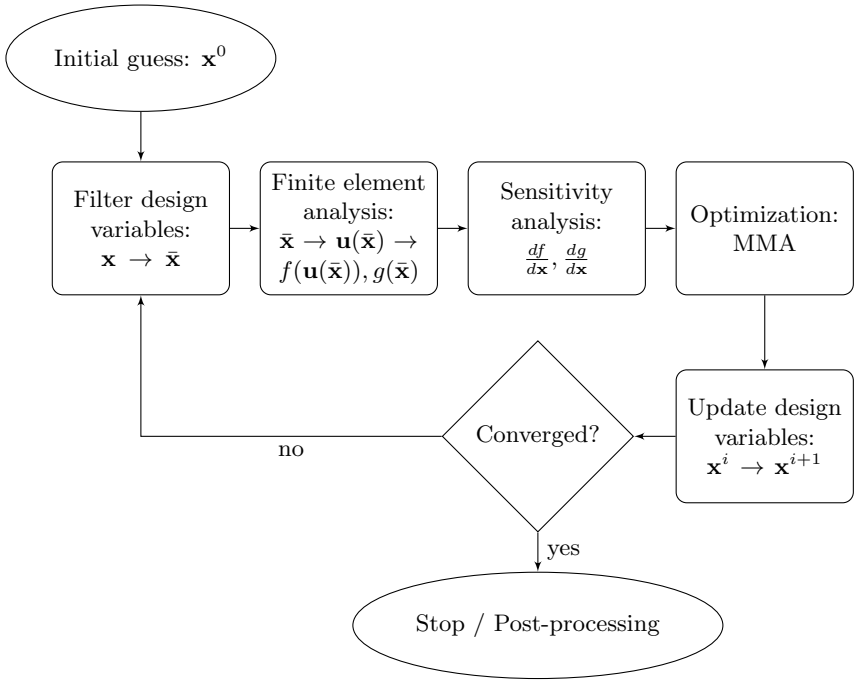

Figure 5.1: Flowchart of the optimization process

of voids is dispersed over multiple smaller holes, rather than one large hole. The most extreme form of this problem is a checkerboard design. These are designs with alternating filled and void elements. This leads to a numerically stiff, but practically useless design. A second issue is the "gray" area problem. Density based topology optimization uses fictitious materials with material properties based on an interpolation of the specified possible materials (e.g. soil and concrete). These fictitious materials are present as long as elements have a design density variable that is neither zero nor one, but somewhere in between. Ideally, when the optimization converges, all elements have a design density of either zero or one, representing either of the real materials. However, if not accounted for, it often occurs that when the optimization process has converged, some elements still have intermediate densities and thus represent a fictitious combination of the two materials. Fortunately, all these complications can be subverted by using filters. Multiple filters exist. Here a number of interventions are combined in a method coined the three-field SIMP [43]. This method involves a penalty factor used in the interpolation of material properties, the application of a density filter and a density projection. The name follows from the use of the design variable field ρ, the filtered field $\tilde{\rho}$ and the projected field $\bar{\rho}$.

5.2.1 SIMP

The SIMP approach was the first response to mitigate the intermediate densities found in final designs [35, 59]. In chapter 4, it was explained that the elements of the design domain depended on the soil properties, the barrier properties and the design variable. The SIMP approach uses an interpolation between two materials with a penalization that results in intermediate densities being less efficient. The following interpolation function is used for the material properties [19]:

$$\alpha = \alpha_{soil} + \rho_e^p \left(\alpha_{barrier} - \alpha_{soil}\right) \tag{5.1}$$

In the above function, p is the penalty factor. This penalty factor ensures that intermediate densities are less effective. When combined with a volume constraint, the intermediate densities are inefficient as the increased material properties are penalized, but the contribution to the total volume remains the same. Previous studies penalized the contribution to the stiffness matrix with a factor $p = 3$. The contribution to the mass matrix was not penalized. As this was proven effective, the same approach is applied in this thesis.

5.2.2 Density filter

Multiple options exist to reduce mesh-dependency. Among these options are perimeter constraints, sensitivity filters and density filters [45]. Here the choice was made for a density filter. The density filter is formulated as [60]:

$$\tilde{\rho}_e = \frac{\sum\limits_{i \in N_e} w(\mathbf{x}_i) v_i \rho_i}{\sum\limits_{i \in N_e} w(\mathbf{x}_i) v_i}, \tag{5.2}$$

where v_i is the volume of element i, ρ_i is the density of element i, $\mathbf{x}_i$ is the spatial (center) location of element i, N_e is the neighborhood of element e, consisting of elements that have centers within a predefined filter radius R and $w(\mathbf{x}_i)$ is the weighting function given by

$$w(\mathbf{x}_i) = R - \|\mathbf{x}_i - \mathbf{x}_e\| . \tag{5.3}$$

When using this filter, the density of each element is a function of the density of that element and the densities of its neighboring elements within a certain radius. This effectively prevents mesh-dependence and checkerboard designs by setting a length-scale for the structure.

5.2.3 Threshold projection

An unwanted side-effect of the density filter is an increased amount of "gray" elements. The penalty on the stiffness is incapable of counteracting the intermediate densities resulting form the density filter. Initial studies introduced a Heaviside function that slowly forced elements above $\rho_{e,min}$ to go to 1 [61]. The downside of this Heaviside filter was that the volume was increased when the Heaviside function was applied. In response, a volume preserving Heaviside function was created [60]. This function was later adapted into a continuous function of the form [1, 43, 62]:

$$\bar{\rho}_e = \frac{\tanh(\beta\eta) + \tanh(\beta(\tilde{\rho}_e - \eta))}{\tanh(\beta\eta) + \tanh(\beta(1 - \eta))} \tag{5.4}$$

where η is the projection threshold and β is the projection parameter. As the projection parameter approaches infinity, the function approaches a Heaviside function (see figure 5.2). During the optimization process, the projection threshold is kept at 0.5, while the projection parameter starts at 1 and is exponentially increased until it reaches 32. This allows a larger amount of freedom in the at earlier iterations, while reducing the gray areas of the final design.

5.3 Objective function and constraints

For the formulation of the problem for topology optimization of wave barriers two approaches seem promising. The optimization can be aimed at minimizing the vibrations such that the volume remains below a maximum volume. Another possibility is minimizing the volume such

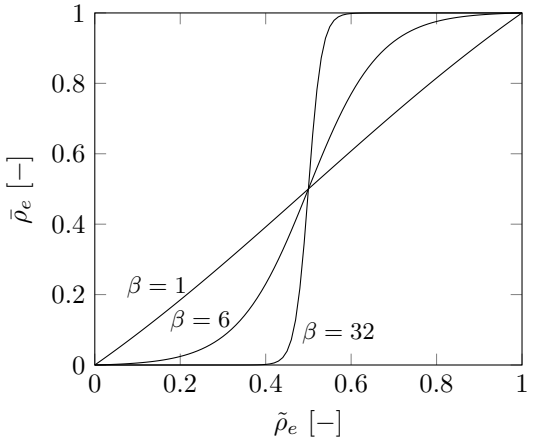

Figure 5.2: Projected density ($\bar{\rho}_e$) as a function of the filtered density ($\tilde{\rho}_e$) for different projection parameters (β) and projection threshold $\eta = 0.5$.

that the vibrations remain below certain vibration criteria. Both approaches were showcased in previous studies [19, 20]. If the goal is to design a wave barrier that satisfies the criteria for the lowest possible volume of material, the second approach appears to be the preferred method. However, the second approach appears to be much more dependent on an accurate modelling of the source. In engineering practice, information on the loading will often be limited to a measured spectrum at the receiver. If a criterion such as a maximum velocity is used, information about the phase difference between the amplitudes of each frequency is required as well. Also taking into account the limitations of the model that is used, the determination of the optimal lay-out of material for a given volume is considered to be a more reliable approach. This can then be used to estimate the maximum reduction that is possible or as a tool to suggest geometries that might not be thought of otherwise.

5.3.1 Objective function

The previous studies used three objective functions for the maximization of vibration reduction using topology optimized wave barriers. The objective functions all catered to different goals. A commonality between the objective functions was the use of the insertion loss at a single point in the model to determine the effectiveness of the barrier [19, 20]:

$$\mathrm{IL} = 10 \log_{10} \left(\frac{\left| \hat{u}^{out,x}_{\mathrm{orig}}(f_n) \right|^2 + \left| \hat{u}^{out,y}_{\mathrm{orig}}(f_n) \right|^2}{\left| \hat{u}^{out,x}(f_n) \right|^2 + \left| \hat{u}^{out,y}(f_n) \right|^2} \right) \tag{5.5}$$

The insertion loss is a logarithmic function that determines the amplitude reduction in dB where $\hat{u}$ represents the complex displacements resulting from the frequency domain analysis, f_n represents the frequency, subscript *orig* represents the values without wave barrier and x and y represent the horizontal and vertical displacements respectively. A greater insertion loss indicates a better performing barrier. The optimizer that was used was designed for a minimization problem. In order to allow for a minimization, the objective function was reformulated as the negative

insertion loss:

$$\mathrm{F} = -\mathrm{IL} = 10\log_{10}\left(\frac{\left|\hat{u}^{out,x}(f_n)\right|^2 + \left|\hat{u}^{out,y}(f_n)\right|^2}{\left|\hat{u}^{out,x}_{\mathrm{orig}}(f_n)\right|^2 + \left|\hat{u}^{out,y}_{\mathrm{orig}}(f_n)\right|^2}\right) \tag{5.6}$$

This negative insertion loss function was used in three different objective functions. The first was a function suitable for situations in which the load is of a single known harmonic frequency. In this situation, the insertion loss function as given above is sufficient. The second objective function is suitable for situations in which the load is of a single unknown frequency within a certain frequency range. In this situation, a min-max form of the problem was used, where equation 5.6 was used to determine the effectiveness of the wave barrier for each frequency. In each step, the design was optimized for the frequency that produced the least insertion loss. The third approach is suitable for situations in which a uniform broadband spectrum within a given frequency range is expected. For this situation the objective function was changed to the average insertion loss over the considered frequency range:

$$\mathrm{F} = \frac{1}{f_u - f_l}\int_{f_l}^{f_u} -\mathrm{IL}(f)\mathrm{d}f = \frac{10}{f_u - f_l}\int_{f_l}^{f_u} \log_{10}\left(\frac{\left|\hat{u}^{out,x}(f_n)\right|^2 + \left|\hat{u}^{out,y}(f_n)\right|^2}{\left|\hat{u}^{out,x}_{\mathrm{orig}}(f_n)\right|^2 + \left|\hat{u}^{out,y}_{\mathrm{orig}}(f_n)\right|^2}\right)\mathrm{d}f \tag{5.7}$$

As the FEM only determines the displacement amplitudes for single frequencies, equation 5.7 had to be discretized:

$$\mathrm{F} = \frac{10}{\mathrm{N}_f}\sum_{n=1}^{\mathrm{N}_f} \log_{10}\left(\frac{\left|\hat{u}^{out,x}(f_n)\right|^2 + \left|\hat{u}^{out,y}(f_n)\right|^2}{\left|\hat{u}^{out,x}_{\mathrm{orig}}(f_n)\right|^2 + \left|\hat{u}^{out,y}_{\mathrm{orig}}(f_n)\right|^2}\right) \tag{5.8}$$

In this thesis, similar approaches will be used, but with a different objective function. The reason for this comes from certain unwanted aspects of the logarithmic function that might influence the design. These aspects become apparent when investigating the derivative of the objective function for the average insertion loss in 5.8. Assuming u is a scalar, the derivative of the objective function is:

$$\frac{\mathrm{dF}}{\mathrm{dx}} = \frac{10}{\mathrm{N}_f}\sum_{n=1}^{\mathrm{N}_f}\left[\frac{1}{\frac{U(f_n)^2}{U_{\mathrm{orig}}(f_n)^2}\log(10)}\frac{\mathrm{d}}{\mathrm{dx}}\left(\frac{U(f_n)^2}{U_{\mathrm{orig}}(f_n)^2}\right)\right] \tag{5.9}$$

It can be seen that the derivative will increase for lower values of the amplitude reduction ratio (u/u_{orig}). This increases the influence of frequencies for which the barrier already reduces the amplitude the most in determining the sensitivities. The optimized design will then be skewed towards the frequencies for which the design performs well in earlier iterations. For objective functions taking an average over multiple frequencies it is therefore preferable to use a non-logarithmic function. In this thesis the objective was therefore changed to the reduction ratio of the amplitude squared. Considering that the chapter 2 showed that the mechanical energy is proportional to the amplitude squared, this is essentially equal to the energy reduction ratio. A second change to the objective function is concerned with the receiver. Previous studies only considered the objective function for a single node. In this thesis the objective function will be considered for an area at the surface to prevent the possibility of the decrease of vibrations at the target location at the cost of an increase at locations close to the target location. The goal then

is to achieve the largest possible reduction of the energy over an area. For the single harmonic source and the average of multiple sources the objective functions then become:

$$F_{sng} = \frac{\int_{x_1}^{x_2} U(x)^2 \mathrm{d}x}{\int_{x_1}^{x_2} U_{\mathrm{orig}}(x)^2 \mathrm{d}x} \tag{5.10}$$

$$F_{avg} = \frac{1}{f_2 - f_1} \int_{f_1}^{f_2} \frac{\int_{x_1}^{x_2} U(x)^2 \mathrm{d}x}{\int_{x_1}^{x_2} U_{\mathrm{orig}}(x)^2 \mathrm{d}x} \mathrm{d}f \tag{5.11}$$

These are discretized as:

$$F_{single} = \frac{\sum_{e \in \mathbb{R}} U_e^2}{\sum_{e \in \mathbb{R}} U_{e,\mathrm{orig}}^2} \tag{5.12}$$

$$F_{avg} = \frac{1}{N_f} \sum_{n=1}^{N_f} \frac{\sum_{e \in \mathbb{R}} U_e(f)^2}{\sum_{e \in \mathbb{R}} U_{e,\mathrm{orig}}(f)^2} \tag{5.13}$$

where N_f is the number of frequencies considered and $\mathbb{R}$ is the set containing all degrees of freedom for which the vibrations are to be reduced. During this thesis the frequency range is discretized into 16 equidistant frequencies ranging from 5 to 80 Hz. The discretized objective function for the min-max objective is:

$$F_{max} = \max_{f_n} \frac{\sum_{e \in \mathbb{R}} U_e(f)^2}{\sum_{e \in \mathbb{R}} U_{e,\mathrm{orig}}(f)^2} \tag{5.14}$$

$$\tag{5.15}$$

As stated, these objective functions are intended for sources of a single known frequency, a single unknown frequency (min-max) or a uniform broadband frequency spectrum (average). However, when considering the environmental sources, there is hardly ever a single harmonic frequency (known or unknown) nor a uniform broadband spectrum. More likely is a broadband spectrum containing more energy at the lower frequencies. In order to optimize for such sources, a weighted average objective function is introduced. This objective function is discretized as:

$$F_{wtd} = \frac{1}{\sum_{n=1}^{N_f} w_n} \sum_{n=1}^{N_f} \left(w_n \frac{\sum_{e \in \mathbb{R}} U_e(f)^2}{\sum_{e \in \mathbb{R}} U_{e,\mathrm{orig}}(f)^2} \right) \tag{5.16}$$

The frequency weight distribution that will be used throughout this thesis is given in figure 5.3.

5.3.2 Constraints

Two types of constraints are used in this topology optimization: equilibrium constraints and a volume constraint. Due to the nested formulation of the problem, the equilibrium constraints

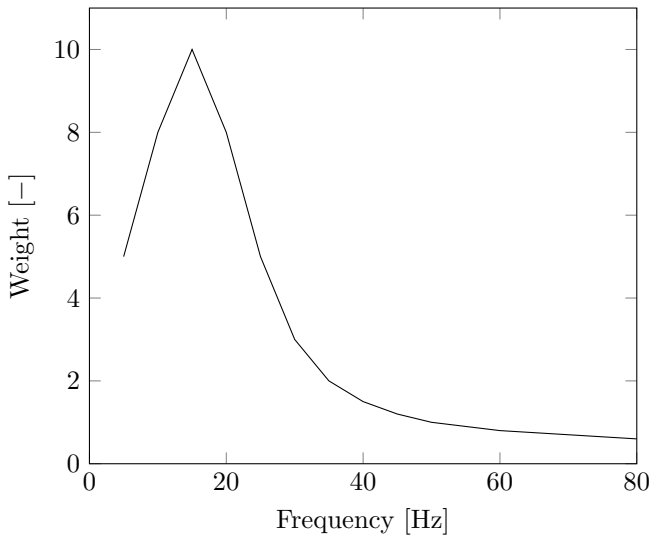

Figure 5.3: Frequency weight distribution

will not be featured in the problem formulation. Instead, the equilibrium constraints will be applied through the FEM model. The volume constraint simply states that the volume of used material should be lower than a specified maximum volume:

$$V \leq V_{max} \tag{5.17}$$

5.3.3 Problem formulation

The mathematical forms of the objective functions and constraint can now be used to form the topology optimization problem in the form shown in chapter 3. As the written algorithm uses matrix formulation to solve the problem, the topology optimization problem is given in a matrix formulation as well. Using $\mathbf{u}$ for the vector containing the displacements for all degrees of freedom and $\mathbf{L}$ for a diagonal matrix with nonzero components only for the degrees of freedom that are of interest (i.e. the DOF associated with the specified receiver area), the problem for a single harmonic frequency can then be written as:

$$\begin{aligned} \min_{\rho} \quad & \frac{\mathbf{u}^H \mathbf{L}\mathbf{u}}{\mathbf{u}_{\text{orig}}{}^H \mathbf{L}\mathbf{u}_{\text{orig}}} \\ \text{s.t.} \quad & \sum_{e=1}^{N_e} V_e \bar{\rho}_e \leq V_{max} \end{aligned}$$

5.4 MMA - Method of Moving Asymptotes

With the problem now fully defined, what remains is a method to solve the problem. Many solvers exist for different optimization problems. Which solver to use depends in part on the type of problem. The optimization of wave barriers is a nonlinear optimization problem. Concerning structural optimization, two methods have seen widespread use. The optimality criteria method (OC) and the method of moving asymptotes (MMA) [45]. A study into the performance of different solvers for nonlinear optimization showed that more recent solvers show similar performances

when compared to OC and MMA, in some cases even outperforming them [63]. However, this benchmark focused on minimum compliance, minimum volume and compliant mechanism design problems. The present problem is of a different nature, and therefore the choice was made to use the MMA solver, as this method has already been proven effective in previous studies concerning the optimization of wave barriers [20, 19]. Additionally, the MMA is capable of handling a large number of constraints and more complex problem formulations such as the minimization of the maximum of a number of different functions [64]. The original version of the MMA has been improved into a globally converging version (GCMMA) [65, 66, 67]. The latter version shows a significant improvement in performance and was therefore the version that was implemented [63]. It should be noted that the fact that the method is globally converging does not imply that the method finds the global optimum. The resulting optimum is still a local optimum that may or may not be the global optimum.

Validation of GCMMA implementation

The implementation of GCMMA was validated by comparing the solution to a number of test problems provided in the original article [66]. Both the objective function value and the design variable distribution agreed perfectly for all problems.

5.5 Sensitivity analysis

The MMA requires information from the first order derivative of the objective function and constraints with respect to the design variables ρ_e. The sensitivity of the volume constraint to the design variables is easy to obtain as this is a linear constraint. In contrast, the sensitivity analysis for the objective function and nonlinear constraints are more complex. When the problem has more variables than response functions, the adjoint method for the design sensitivity analysis is computationally efficient [68]. It should also be noted that due to the three density fields following from the density filter and threshold functions, the gradient of the objective function with respect to the design variables has the form:

$$\frac{\delta F}{\delta \rho_e} = \sum_{i \in N_e} \frac{\delta F}{\delta \bar{\rho}_i} \frac{\delta \bar{\rho}_i}{\delta \tilde{\rho}_i} \frac{\delta \tilde{\rho}_i}{\delta \rho_e}. \tag{5.18}$$

$\frac{\delta F}{\delta \bar{\rho}_i}$ was determined using the adjoint sensitivity analysis. The other derivatives were simply determined from their respective functions.

5.5.1 Adjoint sensitivity analysis

The sensitivity analysis used here is based on the method as described by Tortorelli and Michaleris [68] and Van Hoorickx et al. [19], but applied to the objective function described above.

When a function is of the form $F(u(\bar{\rho}_i), \bar{\rho}_i)$ and $u(\bar{\rho}_i)$ is part of a linear elliptical system of the form $S(\bar{\rho}_i)u(\bar{\rho}_i) = p(\bar{\rho}_i)$, the adjoint sensitivity analysis can be formulated as [68]:

$$F^{adj} = F + \lambda^T (S\hat{u} - \hat{p})), \tag{5.19}$$

It should be noted that the adjoint formulation is equal to the regular problem as $S\hat{u} - \hat{p} = 0$. As such, the sensitivities for the adjoint function are equal to those for the regular function. The Lagrange coefficient (λ) is used at a later stage to eliminate partial derivatives that are difficult to determine. For complex systems equation 5.20 can be expanded to [19]:

$$F^{adj} = F + \lambda^T (S\hat{u} - \hat{p}) + \lambda^H (S^* \hat{u}^* - \hat{p}^*), \tag{5.20}$$

where $[^*]$ denotes the complex conjugate and $[^H]$ denotes the complex conjugate transpose. From this it follows that:

$$\begin{aligned}\frac{\delta F^{adj}}{\delta \bar{\rho}_i} =& \frac{\delta F}{\delta \hat{u}^R}\frac{\delta \hat{u}^R}{\delta \bar{\rho}_i} + \frac{\delta F}{\delta \hat{u}^I}\frac{\delta \hat{u}^I}{\delta \bar{\rho}_i} \\ &+ \lambda^T\left(\frac{\delta S}{\delta \bar{\rho}_i}\hat{u} + S\frac{\delta \hat{u}}{\delta \bar{\rho}_i}\right) \\ &+ \lambda^H\left(\frac{\delta S^*}{\delta \bar{\rho}_i}\hat{u}^* + S^*\frac{\delta \hat{u}^*}{\delta \bar{\rho}_i}\right)\end{aligned} \tag{5.21}$$

Considering that $\hat{u} = \hat{u}^R + i\hat{u}^I$ and $\hat{u}^* = \hat{u}^R - i\hat{u}^I$, equation 5.21 can be expanded to:

$$\begin{aligned}\frac{\delta F^{adj}}{\delta \bar{\rho}_i} =& \frac{\delta F}{\delta \hat{u}^R}\frac{\delta \hat{u}^R}{\delta \bar{\rho}_i} + \frac{\delta F}{\delta \hat{u}^I}\frac{\delta \hat{u}^I}{\delta \bar{\rho}_i} \\ &+ \lambda^T\frac{\delta S}{\delta \bar{\rho}_i}\hat{u}^R + i\lambda^T\frac{\delta S}{\delta \bar{\rho}_i}\hat{u}^I \\ &+ \lambda^T S\frac{\delta \hat{u}^R}{\delta \bar{\rho}_i} + i\lambda^T S\frac{\delta \hat{u}^I}{\delta \bar{\rho}_i} \\ &+ \lambda^H\frac{\delta S^*}{\delta \bar{\rho}_i}\hat{u}^R - i\lambda^H\frac{\delta S^*}{\delta \bar{\rho}_i}\hat{u}^I \\ &+ \lambda^H S^*\frac{\delta \hat{u}^R}{\delta \bar{\rho}_i} - i\lambda^H S^*\frac{\delta \hat{u}^I}{\delta \bar{\rho}_i}\end{aligned} \tag{5.22}$$

This is rearranged to give:

$$\begin{aligned}\frac{\delta F^{adj}}{\delta \bar{\rho}_i} =& \left(\frac{\delta F}{\delta \hat{u}^R} + \lambda^T S + \lambda^H S^*\right)\frac{\delta \hat{u}^R}{\delta \bar{\rho}_i} \\ &+ \left(\frac{\delta F}{\delta \hat{u}^I} + i\lambda^T S - i\lambda^H S^*\right)\frac{\delta \hat{u}^I}{\delta \bar{\rho}_i} \\ &+ \lambda^T\frac{\delta S}{\delta \bar{\rho}_i}\hat{u} + \lambda^H\frac{\delta S^*}{\delta \bar{\rho}_i}\hat{u}^*\end{aligned} \tag{5.23}$$

The derivatives $\frac{\delta \hat{u}^R}{\delta \bar{\rho}_i}$ and $\frac{\delta \hat{u}^I}{\delta \bar{\rho}_i}$ are inconvenient to determine and can be eliminated from equation 5.23 if:

$$\frac{\delta F}{\delta \hat{u}^R} + \lambda^T S + \lambda^H S^* = 0 \tag{5.24a}$$

$$\frac{\delta F}{\delta \hat{u}^I} + i\lambda^T S - i\lambda^H S^* = 0 \tag{5.24b}$$

Now the Lagrange coefficient must be determined such that the partial derivatives are eliminated. To do this first equation 5.24b is multiplied with i and added to equation 5.24a:

$$\left(\frac{\delta F}{\delta \hat{u}^R} + \lambda^T S + \lambda^H S^*\right) - i\left(\frac{\delta F}{\delta \hat{u}^I} + i\lambda^T S - i\lambda^H S^*\right) = 0 \tag{5.25}$$

$$\tag{5.26}$$

Assuming $S^T = S$, 5.25 can be simplified to:

$$\lambda = -\frac{1}{2}S^{-1}\left(\frac{\delta F}{\delta \hat{u}^R} + i\frac{\delta F}{\delta \hat{u}^I}\right)^T \tag{5.27}$$

In order to determine the Lagrange coefficient, the derivatives of the objective function with respect to $\hat{u}^R$ and $\hat{u}^I$ must be determined. As a reminder, the objective function is given below:

$$F = \frac{\hat{u}^H L \hat{u}}{\hat{u}^H_{orig} L \hat{u}_{orig}} \tag{5.28}$$

The derivative with respect to $\hat{u}^R$ then becomes:

$$\begin{aligned} \frac{\delta F}{\delta \hat{u}^R} &= \frac{1}{\hat{u}^H_{orig} L \hat{u}_{orig}} \frac{\delta}{\delta \hat{u}^R} \left(\hat{u}^H L \hat{u} \right) \\ &= \frac{1}{\hat{u}^H_{orig} L \hat{u}_{orig}} \nabla \left(\hat{u}^H \cdot \hat{u}^T \right) L \\ &= \frac{1}{\hat{u}^H_{orig} L \hat{u}_{orig}} \left(J^T_{\hat{u}^T, \hat{u}^R} \hat{u}^H + J^T_{\hat{u}^H, \hat{u}^R} \hat{u}^T \right) L, \end{aligned} \tag{5.29}$$

where $J^T_{a,b}$ is the Jacobian of a with respect to b. Here the Jacobian is equal to the identity matrix of size $[n \times n]$.

$$J^T_{\hat{u}^T, \hat{u}^R} = J^T_{\hat{u}^H, \hat{u}^R} = I_n. \tag{5.30}$$

Inserting 5.30 into 5.29 gives:

$$\frac{\delta F}{\delta \hat{u}^R} = \frac{1}{\hat{u}^H_{orig} L \hat{u}_{orig}} \left(\hat{u}^H + \hat{u}^T \right) L. \tag{5.31}$$

In a similar fashion, but with $J^T_{\hat{u}^T, \hat{u}^I} = -J^T_{\hat{u}^H, \hat{u}^I} = iI_n$:

$$\frac{\delta F}{\delta \hat{u}^I} = \frac{1}{\hat{u}^H_{orig} L \hat{u}_{orig}} \left(i\hat{u}^H - i\hat{u}^T \right) L. \tag{5.32}$$

Inserting these results into equation 5.27 gives an expression for the Lagrange coefficient that can be determined from the dynamic stiffness matrix and the displacements calculated using the FEM:

$$\begin{aligned} \lambda &= -\frac{1}{2} S^{-1} \left(\frac{\delta F}{\delta \hat{u}^R} - i \frac{\delta F}{\delta \hat{u}^I} \right)^T \\ &= -\frac{1}{2} S^{-1} \left(\frac{1}{\hat{u}^H_{orig} L \hat{u}_{orig}} \left(\hat{u}^H + \hat{u}^T \right) L - i \frac{1}{\hat{u}^H_{orig} L \hat{u}_{orig}} \left(i\hat{u}^H - i\hat{u}^T \right) L \right)^T \\ &= -S^{-1} \left(\frac{\hat{u}^H L}{\hat{u}^H_{orig} L \hat{u}_{orig}} \right)^T \end{aligned} \tag{5.33}$$

Now that the Lagrange coefficient can be determined from equation 5.33, equation 5.23 can be reduced to:

$$\frac{\delta F^{adj}}{\delta \bar{\rho}_i} = \lambda^T \frac{\delta S}{\delta \bar{\rho}_i} \hat{u} + \lambda^H \frac{\delta S^*}{\delta \bar{\rho}_i} \hat{u}^* = 2 \operatorname{Re} \left\{ \lambda^T \frac{\delta S}{\delta \bar{\rho}_i} \hat{u} \right\} \tag{5.34}$$

In equation 5.34, the Lagrangian can be determined using equation 5.33, the displacements can be determined using the FEM and the derivative of the dynamic stiffness matrix S can be readily determined by taking into account the SIMP interpolation that was used.

5.5.2 Density filter derivative

The density filter was used to remove mesh-dependency and checkerboard problems. The density filter introduced the new density field $\tilde{\rho}_e$. The derivative of the density of element e with respect to the density of element i is:

$$\frac{\delta\tilde{\rho}_i}{\delta\rho_e} = \frac{w(\mathbf{x}_e)v_e}{\sum\limits_{j\in N_i} w(\mathbf{x}_j)v_j} \tag{5.35}$$

5.5.3 Density threshold derivative

The density threshold forces the density towards 0 or 1. It introduces a new density field $\tilde{\rho}_e$. The derivative is of the density threshold function is:

$$\frac{\delta\bar{\rho}_i}{\delta\tilde{\rho}_i} = \frac{\beta\,\mathrm{sech}\left(\beta\left(\tilde{\rho}_i-\eta\right)\right)^2}{\left(\tanh\left(\beta\left(1-\eta\right)\right)+\tanh\left(\beta\eta\right)\right)}. \tag{5.36}$$

Part IV

Research

Chapter 6

Optimization for low frequency waves

In chapter 1 it was stated that a large part of the energy of the vibrations caused by environmental sources (e.g. railway traffic) is contained in the lower frequencies (approximately 10 to 40 Hz). For very soft soils the most severe vibrations occur at even lower frequencies. These lower frequencies are expressed in waves with longer wavelengths that are often difficult to mitigate. Parameters studies investigating which factors are important for the effectiveness of wave barriers found that the ratio between the barrier dimensions and the wavelength was very important [58, 69]. In one of the studies it was argued that a width of 0.3 times the Rayleigh wavelength and a depth of 1.0 times the Rayleigh wavelength were required for a sufficiently effective barrier [69]. For lower frequencies this would require large wave barriers that would be either too expensive or would take up too much room in most situations. The wave barrier geometries that were investigated in these studies were very limited. Different geometries might allow for effective wave barriers with much smaller dimensions than those suggested. The previous studies into the topology optimization of wave barriers largely ignored the lower frequency range. This chapter therefore investigates the possibilities offered by topology optimization for the design of wave barriers for lower frequency sources. The use of topology optimization might lead to designs for lower frequencies that require less material or take up less space than wave barriers of a standard geometry. In section 6.1 wave barriers are optimized for different source frequencies. Section 6.2 illustrates the importance of the ratio between the allowed dimensions and volume of the barrier and the wavelength. Section 6.3 illustrates and discusses the implications of the findings for the applicability of the different objective functions.

6.1 Single harmonic frequency source

In this chapter a homogeneous soil model was used. The properties of the soil and the wave barrier were derived from a previous topology optimization study [19](see table 6.1). The model that was used is shown in figure 6.2. Wave barriers were optimized for three different single harmonic frequencies (5, 25 and 50 Hz) with a maximum allowed volume fraction equal to 20% of the design domain. A reference barrier was created as well in order to compare the effectiveness of the optimized wave barriers with a more general vertical wall wave barrier. The reference barrier is located at the center of the design domain and has a depth equal to the depth of the design domain and a width such that the volume of the reference barrier equals the maximum volume

Type	E mod. (MPa)	Density (kg/m^3)	Poisson's ratio (-)	C_p (m/s)	C_s (m/s)
Soil	250	2000	0.45	689	208
Barrier	1500	2000	0.25	949	548

Table 6.1: Soil properties

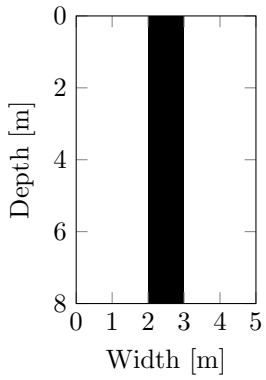

Figure 6.1: Reference wave barrier

constraint (see figure 6.1).

The resulting wave barrier shapes can be seen in figure 6.3 on the left. The performance of the barriers over a frequency range of 1-80 Hz is shown in the same figure on the right. In the performance figures, the optimized wave barrier is compared to the reference barrier. The frequency that was optimized for is indicated by the vertical dotted line. The first important thing to notice is that in all cases, the optimized barrier outperforms the reference barrier for the target frequency. When optimizing for a higher frequency source (50 Hz), the energy reduction ratio ($E_r = |U_{barrier}|^2 / |U_{orig}|^2$) is nearly zero for the target frequency. The barrier optimized for a 25 Hz source achieves a lesser, but still significant energy reduction ratio. In contrast, the energy reduction achieved for the 5 Hz source is limited, and only a marginal improvement over the reference barrier. As was expected, waves resulting from a lower frequency source were more difficult to mitigate.

The above is all valid when looking at the target frequencies, however it is important to note that the optimized barrier often performs worse than the reference barrier for other source frequencies. In the worst cases the E_r is greater than one, indicating that waves of those frequencies are actually amplified. This occurs to a great extent in the wave barrier optimized for 5 Hz. Over the frequency range of 25-80 Hz the energy is amplified with a factor up to 2.25. It appears that significant amplification is possible for frequencies other than the target frequency. This indicates that some care is required when selecting the frequency range that is optimized for when other objective functions are used. Here only single frequencies were optimized for, but when considering a frequency range, it would still be likely that frequencies outside of the considered range are amplified.

The diminishing effectiveness of the optimized wave barriers with decreasing frequencies confirms findings from literature indicating that waves resulting from lower frequency sources are more difficult to mitigate. The wavelengths induced by the source frequencies with the soil properties as described in table 6.1 are: $\lambda_{R(5)} = 39.3$m, $\lambda_{R(25)} = 7.9$m and $\lambda_{R(50)} = 3.9$m. In

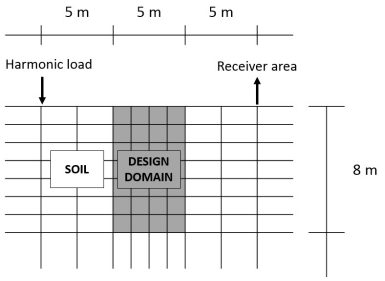

Figure 6.2: Inner domain of model

contrast, the design domain size was 5×8m and the maximum volume fraction of 20% lead to a maximum volume of 8m^2 per unit length of the wave barrier. These dimensions are large with respect to $\lambda_{R(50)}$, similar to $\lambda_{R(25)}$ and small compared to $\lambda_{R(5)}$. It is therefore argued that, while the more complex geometries designed through topology optimization are more effective than the reference barrier, topology optimized wave barriers are not exempt from the decrease in effectiveness when the considered wavelength is large compared to the dimensions of the wave barrier. However, here only a single example is taken that shows this trend. The following section further investigates the influence of the wavelength on the achievable energy reduction and attempts to give some insight into the dimensions required for an optimized wave barrier in order to achieve significant energy reduction.

6.2 Wavelength dependent model

For an optimized wave barrier, the dimensions of the final design are constrained by the design domain dimensions and the maximum allowed volume. In this section an attempt is made to give some insight into the effects of these constraints using a frequency independent model. This model is created by normalizing all geometries with respect to the Rayleigh wavelength. The resulting energy reduction ratio should then be frequency independent. The normalized geometries are depicted in figure 6.4. The element sizes were already dependent on the wavelength, except for those in the design domain. Here the design domain is always discretized in 50 elements in the horizontal and 50 elements in the vertical direction. This was done in order to prevent a very low resolution if the design domain dimensions were chosen to be small compared to the wavelength. The properties of the soil and the barrier remain the same as in the previous section.

The frequency independence of the model is illustrated by optimizing a wave barrier for two different source frequencies (5 and 50 Hz). The resulting wave barriers are compared in figure 6.5. In this figure the black areas indicate material found in both final designs, while the gray areas indicate that material was found there in only one of the final designs. For either source frequency, the same value for the energy reduction ratio was reached ($\text{E}_\text{r} = 0.83$). When comparing the topologies, the barriers are similar as well, with the only differences occurring near the edges of the design.

In order to gain some insight into the role of the design domain dimensions and the maximum allowed volume with respect to the wavelength, barriers were optimized while varying both parameters as a function of the Rayleigh wavelength. Four design domains were examined with sides as shown in figure 6.4 taking the values $\text{x}_\text{dd} = \text{z}_\text{dd} = [0.25, 0.5, 0.75, 1.0]$. For each design domain, the wave barrier was optimized with volume constraints varying between $0.0125\lambda_R^2$ and $0.2\lambda_R^2$. The largest design domain showed some of the limitations of the optimization algorithm

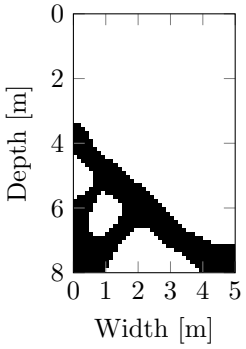

(a) Wave barrier for 5 Hz

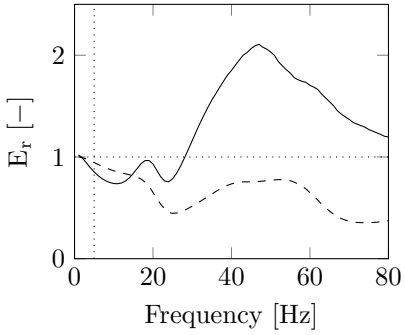

(b) E_r for 5 Hz

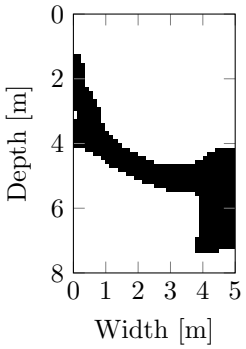

(c) Wave barrier for 25 Hz

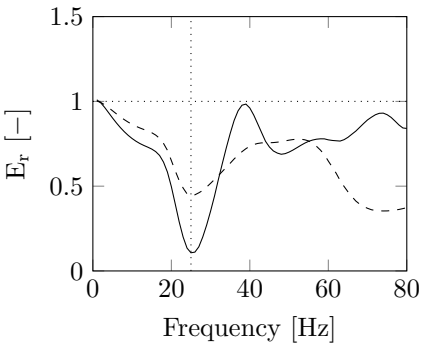

(d) E_r for 25 Hz

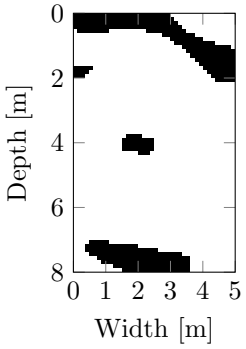

(e) Wave barrier for 50 Hz

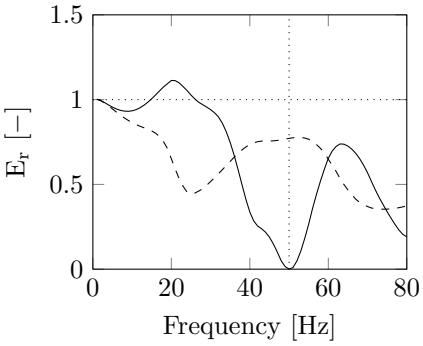

(f) E_r for 50 Hz

Figure 6.3: The optimized barriers for different source frequencies of 5 Hz, 25 Hz and 50 Hz. For (a), (c) and (e) black indicates barrier material and white indicates soil. (b), (d) and (f) show the energy reduction ratio of the optimized barrier (——) and the reference barrier (- - -).

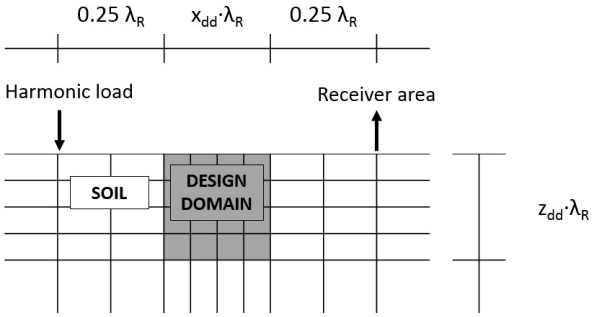

Figure 6.4: Inner domain of the wavelength dependent model

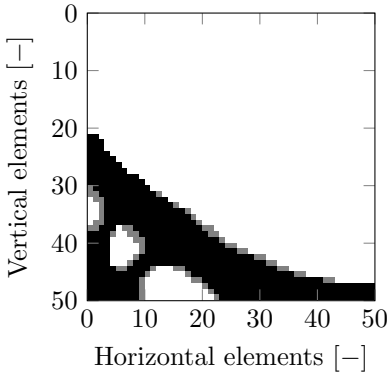

Figure 6.5: Difference between topology optimized wave barriers for 5 Hz and 50 Hz using a model normalized by the Rayleigh wavelength. Black indicates barrier material in both optimizations, white indicates soil in both optimizations and gray indicates a difference between the two optimizations.

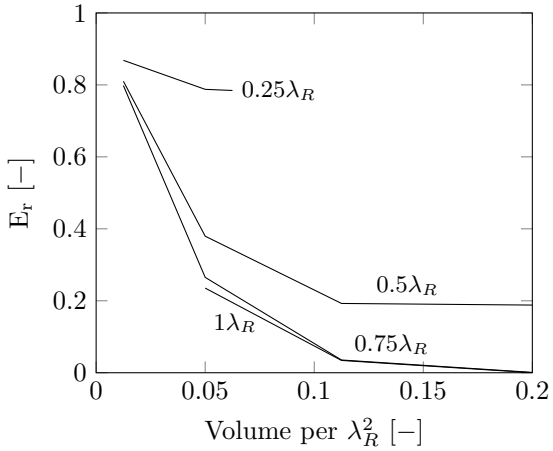

Figure 6.6: Comparison of the maximum achieved E_r for different normalized maximum volumes and square design domain side lengths.

as it was unable to find a solution for the lowest volume constraint.

The resulting energy reductions are shown in figure 6.6. The resulting topologies of the wave barriers can be found in appendix A. The results confirm what was expected: increasing the dimensions and maximum volume with respect to the Rayleigh wavelength increases the energy reduction of the optimized design. Some interaction between the volume constraints and the design domain constraints is visible as well. Identical volume constraints lead to more effective barriers if the design domain dimensions are larger. This is however only valid up to a certain point. For the soil and barrier material parameters that were used, design domain sizes larger than $0.75\lambda_R$ appear to contribute very little in terms of barrier effectiveness. This is resembled in the topologies, that remain very similar with increased design domain size.

It should be noted that figure 6.6 should not be used as a guideline for design domain dimensions or volume constraints. The values shown were determined for a specific set of soil and barrier material properties. The ratio between many of these respective properties (e.g. Young's modulus, shear modulus and density) were determined to be important for the wave barrier effectiveness as well [58, 69]. As such, the absolute values for the achievable energy reduction ratio as a function of the ratio between the volume and design domain constraints and the wavelength would not remain the same for different soil and barrier parameters. However, the general tendencies depicted in figure 6.6 can be expected for other soil and barrier parameters. The consequence of this is that, if significant energy reduction is required for waves with greater wavelengths, a sufficiently large design domain and volume constraint is required.

6.3 Average and min-max objective functions

The previous section established the difficulty in designing effective wave barriers for waves with greater wavelengths. This section illustrates and discusses the implications of this for the feasibility of the different objective functions that were discussed in chapter 5. Three different objective functions that optimize for a frequency range were discussed. The min-max objective function optimizes for the worst performing frequency within the frequency range at each iteration. This function is most appropriate for a sources of a single, unknown frequency. The average objective function optimizes the average energy reduction over all considered frequencies and is therefore

most appropriate for a uniformly distributed broadband source. The weighted average only differs from this by assigning different weights to the considered frequencies and is appropriate for a non-uniformly distributed broadband source.

A wave barrier was optimized for each of the three objective functions in the model as specified in section 6.1. As a reminder, the considered frequency range is 5-80 Hz and discretized in 16 equidistant frequencies. The weights that are assigned in the weighted average objective function were shown previously in figure 5.3, chapter 5. The resulting topology and energy reduction over the considered frequency range is depicted in figure 6.7. The wave barrier optimized using the min-max objective function shows the greatest energy reduction for the lower frequencies. This is a direct result of the difficulty for the wave barriers to reduce the energy transmitted by low frequency sources. The wave barriers generally perform worse for these lower frequencies, and as a result, the optimization algorithm will be fully focused on reducing the energy at these frequencies. However, when comparing to the wave barrier optimized for the single 5 Hz frequency source, the min-max objective function does prevent the design of a barrier that amplifies the energy for the higher frequencies. In stark contrast, the average objective function shows a nearly identical energy reduction for the lower frequencies as the reference barrier, while achieving much greater energy reductions for the higher frequencies. The weighted average objective functions shows the most even increase of the energy reduction over the considered range due to the larger weights assigned to the lower frequencies.

The spectrum of vibrations induced by environmental sources is expected to be of a non-uniform broadband nature. In these situations the weighted average objective functions is expected to be the most appropriate objective function. Other situations can be thought of where only a small spectrum of the vibrations is problematic due to structure properties. For these a single harmonic frequency might be used with constraints for the rest of the frequency range to prevent unwanted amplification of energy.

6.4 Summary

In this chapter the use of topology optimization to design barriers that aim to mitigate vibrations at lower frequencies is explored. Initial findings showed that, although the wave barriers always outperformed the reference barrier for the target frequency, the achievable energy reduction ratio suffered when the allowed barrier dimensions were small compared to the wavelengths. Wave barriers designed for very low frequencies marginally improve the energy reduction ratio at those frequencies, while greatly diminishing the energy reduction ratio for the greater frequencies. In the case observed here, the wave barrier designed for a 5 Hz source frequency actually amplified the energy with a factor of up to 2.25 for many frequencies other than the target frequency.

A frequency independent model was used to more carefully investigate the relation between the wave barrier dimensions and the wavelength, focusing on the interaction between the design domain dimensions and the volume constraint. It was shown that for relatively small design domains, an increase in the volume constraint has comparatively little effect. For larger design domains, an increase in the volume constraint has much more effect, while further increase of the domain size appear to be ineffectual.

It was also explored how the difficulty to mitigate waves of greater wavelengths with relatively small wave barriers affect the different objective functions. Both the min-max and the average objective functions showed some flaws. The addition of weights to the average objective function reduced some of the weaknesses and was determined to be the most appropriate for problems concerning environmental vibrations. This latter function will therefore be the focus in the following chapters whenever a frequency range is considered.

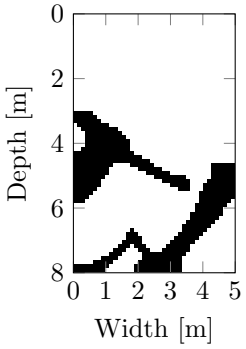

(a) Wave barrier for MINMAX

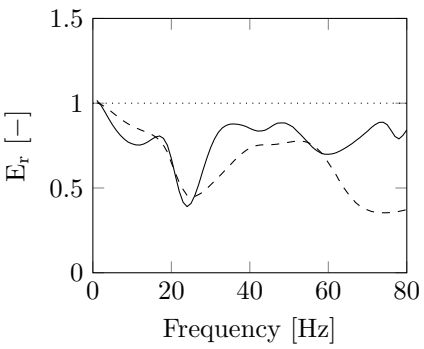

(b) E_r for MINMAX

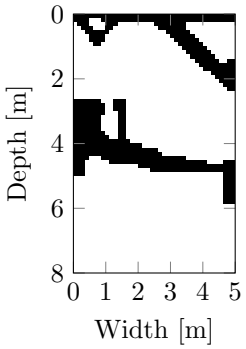

(c) Wave barrier for AVG

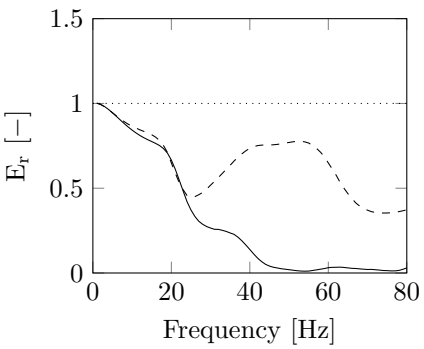

(d) E_r for AVG

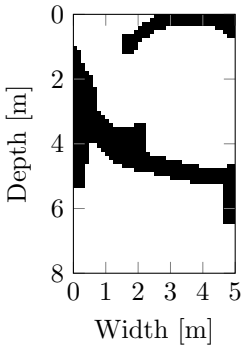

(e) Wave barrier for wAVG

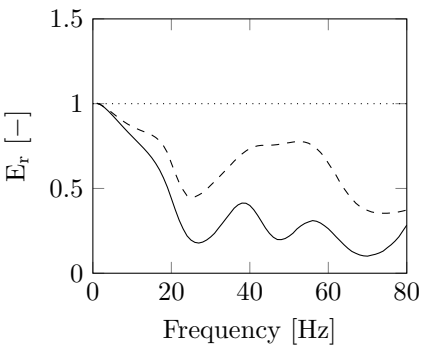

(f) E_r for wAVG

Figure 6.7: The optimized barriers and their performance (——) compared to the reference barrier (- - -) over the frequency range 1-80 Hz for the average reduction ratio (AVG), the weighted average (wAVG) and the minimization of the maximum reduction ratio (MINMAX) objective functions in a homogeneous soil.

Chapter 7

Optimization of wave barriers in layered soils

As a general rule, soils encountered in practice are hardly ever homogeneous. With this in mind, one of the main goals of this thesis is to create a model that can facilitate the optimization of wave barriers for layered soils, as this is necessary for a model usable in the engineering practice. Chapter 4 showed the creation of this model and the conditions that must be met to ensure the accuracy. This chapter will explore the optimization of the topology of wave barriers in layered soils.

In section 7.1 the topology of a wave barrier is optimized for a two-layered soil model comprised of a soft upper layer and a stiff half-space. Specific attention is paid to the differences between a barrier optimized for a homogeneous soil and a barrier optimized for the two-layered soil model. Section 7.2 explores the effect of the presence of a soft layer embedded at some depth in a stiff half-space. The possibility of the optimized barrier to use the soft layer as a wave guide is discussed as well as the possible dangers of the idealized representation of the interfaces.

7.1 Two-layered soil profile

The two-layered soil profile consists of a stiff half-space with a softer layer on top (figure 7.1). The soil properties of the soft and stiff soil are as specified in table 7.1. The interface between the two layers is located at a depth of either 4 m or 10 m. As the design domain reaches a depth of 8 m, the interface is located within the design domain for the shallow variant and below the design domain for the deeper variant.

The dispersion curves were determined to ensure that the PML will function as expected. Figure 7.2 shows the curves for both variants. The shapes of the curves found in both graphs are very similar. The main difference is that each mode starts at a lower frequency when the upper layer is deeper. Additionally, the fundamental mode that approaches the Rayleigh wave velocity of the upper layer with increasing frequency does so for lower frequencies with a deeper upper layer. This is related to figure 2.6 showing that the displacements resulting from a Rayleigh wave are significant up to a depth of about 2.5 times the Rayleigh wavelength. Higher frequencies result in shorter Rayleigh wavelengths. This resullts in a larger part of the significant displacements being contained within the upper layer. The Rayleigh wave velocity will therefore approach the Rayleigh wave velocity of the upper layer as the frequency increases and more of the energy of the Rayleigh wave is contained in the upper layer. For identical soil properties, this occurs for

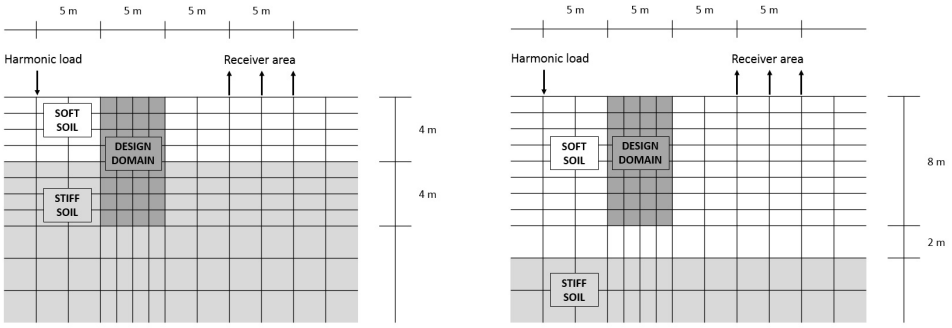

(a) Shallow upper layer (b) Deep upper layer

Figure 7.1: Inner domain of the two-layered soil profiles

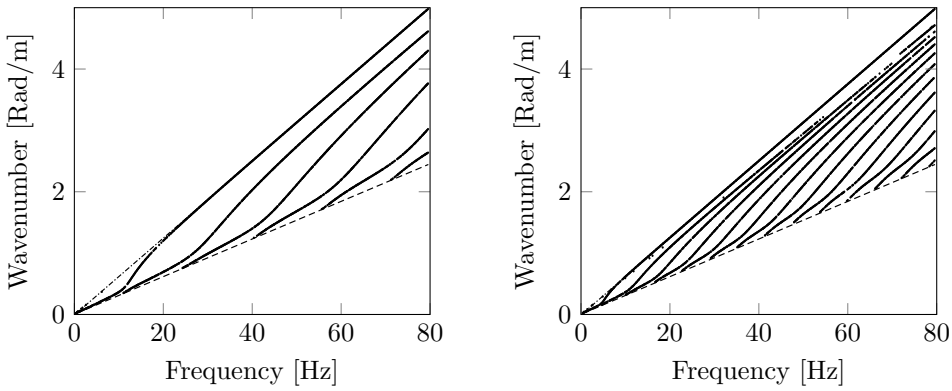

(a) Interface at 4 m (b) Interface at 10 m

Figure 7.2: Dispersion curves for two-layered soil profiles with the Rayleigh wave velocity of the upper layer (-·-·-) and the shear wave velocity of the half-space (- - -).

lower frequencies if the upper layer is deeper, explaining both the similarities and the differences between the two curves.

A second more important similarity between the two curves is the signs of the phase velocity (ω/k) and the group velocity ($d\omega/dk$). These are positive for all frequencies within the required range in both curves. The conditions set in chapter 4 for the usage of the PML as a boundary layer are therefore met for all considered frequencies.

Layer	E mod. (MPa)	Density (kg/m^3)	Poisson's ratio (-)	C_p (m/s)	C_s (m/s)
1	50	1500	0.45	356	107
HS	250	2000	0.45	689	208

Table 7.1: Soil properties of two-layered soil profile

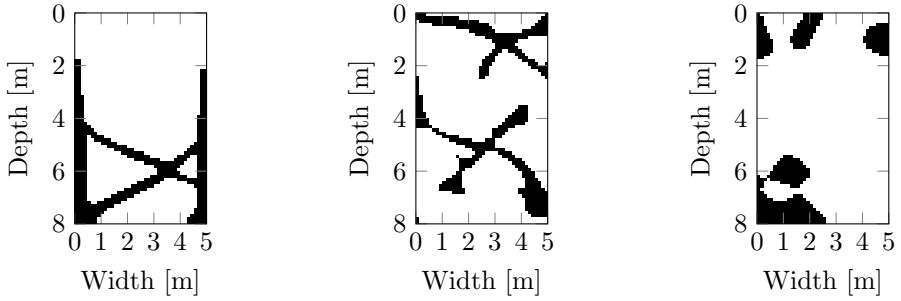

(a) Wave barrier for 5 Hz and deep upper layer

(b) Wave barrier for 25 Hz and deep upper layer

(c) Wave barrier for 50 Hz and deep upper layer

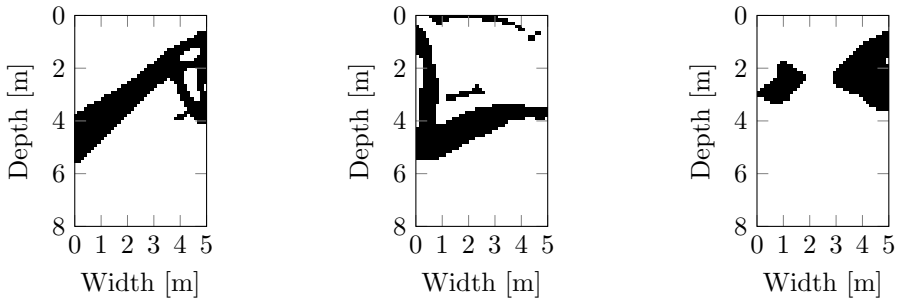

(d) Wave barrier for 5 Hz and shallow upper layer

(e) Wave barrier for 25 Hz and shallow upper layer

(f) Wave barrier for 50 Hz and shallow upper layer

Figure 7.3: Comparison of the topology of wave barriers optimized for single harmonic frequencies in different two-layered soil variants

7.1.1 Single harmonic frequency source

The topology of a wave barrier was optimized in both two-layered profiles for three single frequency objective functions (5, 25 and 50 Hz). The resulting topologies are depicted in figure 7.3. Full results of the barrier geometries and their performance over the frequency range 1-80 Hz can be found in appendix B. The topology of the optimized barriers differs significantly with the change of the interface depth, and with the change of source frequency. Comparing the topology between the shallow and deep upper layer variant, it appears that material tends to be placed more in the layer with the softer soil. For the profile with the shallow upper layer the wave barriers were more concentrated towards the upper parts of the design domain, while the barriers for the deep upper layer used the entire height of the design domain.

Possible factors in this are the stiffness ratio differences and the containment of energy in the upper layer. It was mentioned previously that greater stiffness ratios increased the performance of a wave barrier. It can then be expected that the optimization produces barriers with material located there where the stiffness ratios are the greatest. Furthermore, it was explained in chapter 2 that an interface will cause reflections that result in a larger part of the energy being contained in the upper layer compared to a homogeneous soil profile. It is feasible that optimization of wave barriers for the reduction of energy at a certain area will result in material placement at the locations with the greater part of the energy that would otherwise reach the receiver.

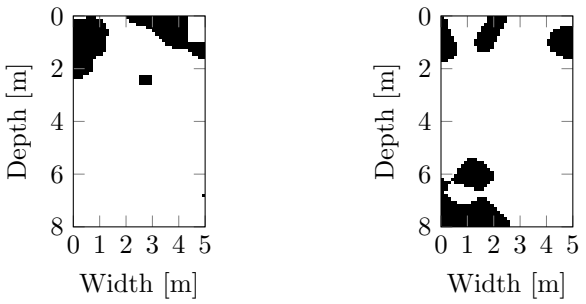

(a) Topology of wave barrier for homogeneous soil

(b) Topology of wave barrier for layered soil

Figure 7.4: Topology of optimized wave barriers for 50 Hz in a homogeneous and layered soil.

Influence of reflections at the interface

The effects of a horizontal interface are further illustrated here by examining wave barriers optimized for a source frequency of 50 Hz in a homogeneous and layered soil. Figure 7.4 shows the topology of a wave barrier that was optimized for a homogeneous soil with properties equal to the soft upper layer of the layered soil model as specified in table 7.1 (from this point on referred to as the homogeneous wave barrier) and the topology of a wave barrier optimized for the layered soil model of the same table (from this point on referred to as the inhomogeneous wave barrier). The topology of both wave barriers differs significantly. Compared to the homogeneous barrier, the topology of the inhomogeneous wave barrier has sacrificed material volume at the top of the design domain in order to place material near the bottom of the design domain. The reason for this becomes clear when examining the real part of the displacement amplitudes for both barriers.

Figures 7.5a and 7.5b show the real part of the displacement for the homogeneous soil model before and after introducing the homogeneous wave barrier. The figures show that most of the energy from the loading is propagated in two wavetypes: a Rayleigh wave and a shear wave. The Rayleigh wave is propagating along the surface, while most of the energy contained in the shear wave is propagating at an angle of around 40 to 45 degrees. It is clear that most of the energy that reaches the target receiver is contained in the Rayleigh wave travelling along the surface. The placement of stiff material near the surface by the optimization algorithm reflects and refracts a large part of the energy that would otherwise reach the receiver, resulting in a large energy reduction ratio.

Figures 7.5c and 7.5d show the real part for the same homogeneous barrier, but instead placed in the layered soil model. It becomes evident from the figure without barrier that much of the energy propagating as a shear wave is reflected from the interface. The reflected shear waves then reach the receiver. The wave barrier optimized for a homogeneous soil does not account for this, and does not impede the reflected energy in reaching the receiver.

Figure 7.5f shows the real part for the inhomogeneous wave barrier when applied in a layered soil. The shear waves that would reach the receivers after reflecting at the interface are instead reflected by the extra material placed near the bottom of the design domain preventing a large part of the energy from reaching the receivers.

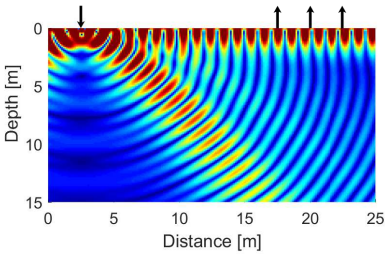

(a) $\hat{\mathbf{u}}_{\text{real}}$ for homogeneous soil model

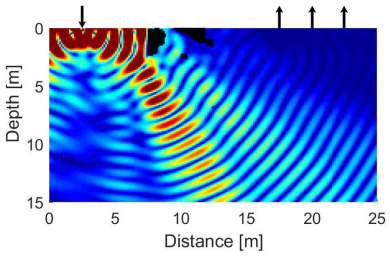

(b) $\hat{\mathbf{u}}_{\text{real}}$ for homogeneous soil model with wave barrier optimized for homogeneous soil

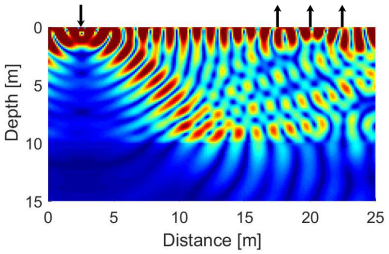

(c) $\hat{\mathbf{u}}_{\text{real}}$ for layered soil model

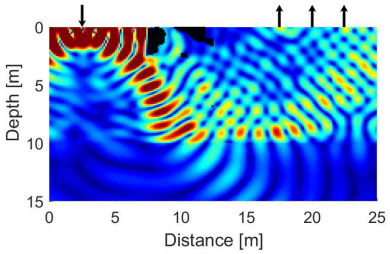

(d) $\hat{\mathbf{u}}_{\text{real}}$ for layered soil model with wave barrier optimized for homogeneous soil

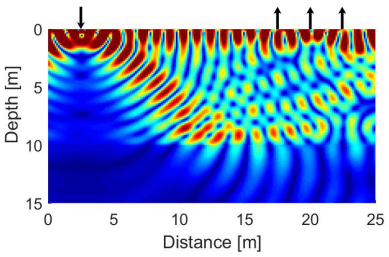

(e) $\hat{\mathbf{u}}_{\text{real}}$ for layered soil model

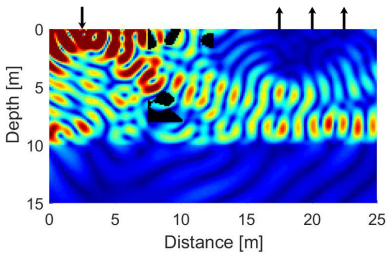

(f) $\hat{\mathbf{u}}_{\text{real}}$ for layered soil model with wave barrier optimized for layered soil

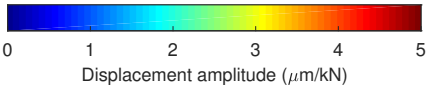

Figure 7.5: $\hat{\mathbf{u}}_{\text{real}}$ for wave barrier optimized for 50 Hz.

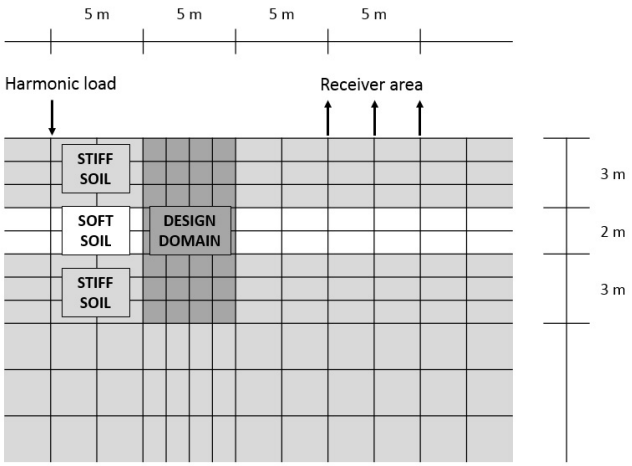

Figure 7.6: Inner domain of three-layered soil model

Layer	Depth (m)	E mod. (MPa)	Density (kg/m^3)	Poisson's ratio (-)	C_p (m/s)	C_s (m/s)
1	3	250	2000	0.45	689	208
2	5	50	1500	0.45	356	107
HS		250	2000	0.45	689	208

Table 7.2: Soil properties of three-layered soil profile

7.2 Three-layered soil profile

A three-layered profile was made to investigate the effects of a softer layer embedded within a stiff soil (figure 7.6). The material parameters that were used can be found in table 7.2. The dispersion curve for this soil model is depicted in figure 7.7. Similar to the previous curves, both the phase velocity and the group velocity are positive over the considered frequency range, meeting the conditions for the use of the PML as a boundary layer.

The topology and performance of the barrier optimized for the weighted average objective function are given in figure 7.8. The results for other objective functions can be found in appendix C. Similar to previous results, the optimized barrier uses a large part of its volume in the softer soil layer. Figure 7.9 shows the normalized difference in the absolute of the displacement after implementation of the optimized wave barrier. The depicted amplitude difference is a weighted summation of the amplitude difference over the discretized frequency range. This figure shows a possible danger of the objective function that was used. In literature the amplitude reduction at the surface is often used as an indicator for the effectiveness of a wave barrier [69, 19, 20, 5, 58]. For this thesis, a similar approach was used but instead the energy reduction at the surface was taken. However, figure 7.9 shows that an objective function using only the surface as a receiver area can result in a wave barrier that decreases the energy at the surface, while increasing the energy below the surface. If a structure is present that includes a basement or has a pile foundation, the increase of the energy transmitted below the surface will likely still affect the structure. Optimizing only for the vibrations at the surface can then not be considered an accurate representation of the expected vibration reduction in the structure.

Figure 7.10 shows the effects of the wave barrier optimized for the weighted average objective

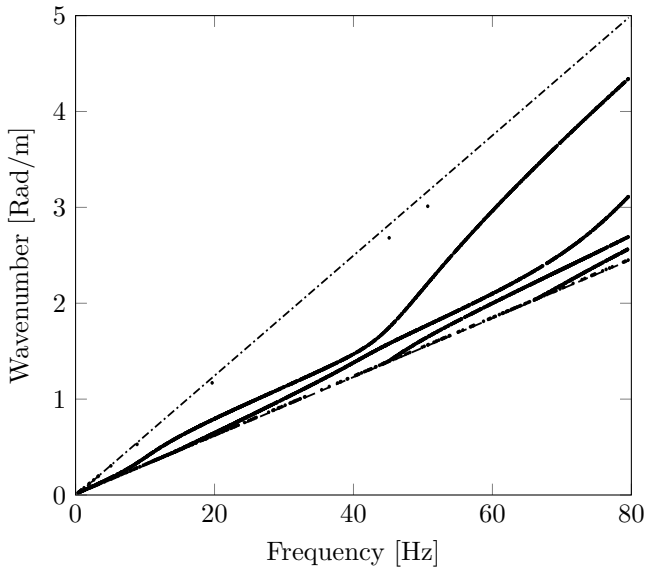

Figure 7.7: Dispersion curve for three layered soil profiles with the Rayleigh wave velocity of the soft soil layer (-·-·-) and the shear wave velocity of the stiff soil (- - -).

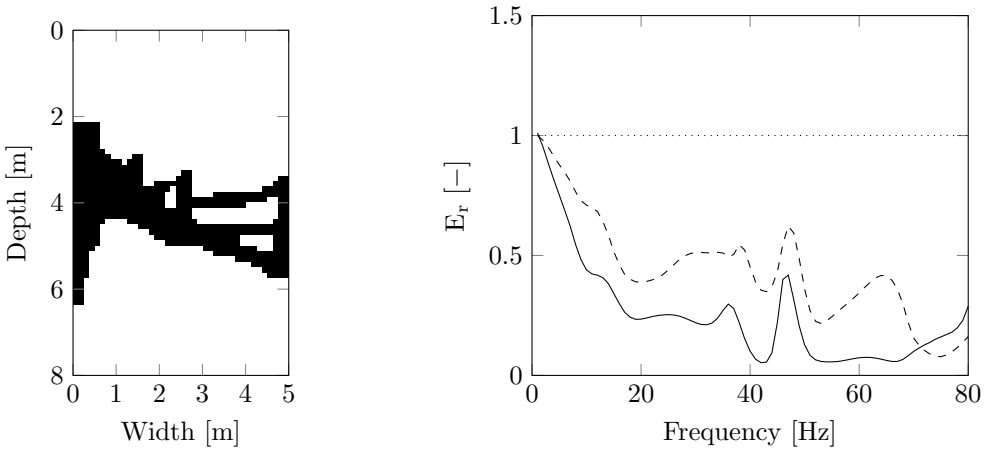

(a) Wave barrier for wAVG

(b) E_r for wAVG

Figure 7.8: The shape and performance of wave barriers optimized for the weighted average objective function (——) and the performance of the reference wave barrier (- - -) in the three-layered soil model.

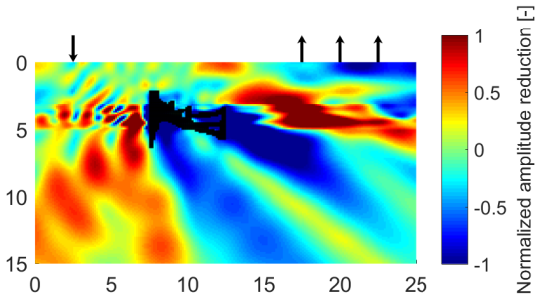

Figure 7.9: Normalized amplitude difference summed over the discretized frequency range

function on the real part of the displacement amplitude for a 50 Hz source. The figure shows the same decrease of the amplitudes at the surface and increase of the amplitudes of the softer layer. Interestingly, the waves travelling through the softer layer appear to have some characteristics that match interface waves. Specifically, the waves do not suffer geometric attenuation and show an amplitude that decays with distance perpendicular to the interface. The optimized wave barrier appears to use the softer layer as a waveguide. Much of the energy appears to be continuously reflected within the softer layer, never reaching the surface. This is possible for shear waves approaching the interface at an angle lower than the critical angle, resulting in a full reflection as a shear wave.

The interface wave appears to match the characteristics of a wavetype discussed previously: the Stoneley wave. In chapter 2 it was already discussed that the characteristic equation for this wavetype only had real roots when the wave velocities of the two layers were similar. Table 7.2 shows that this is not the case. However, it was also stated that if the velocities of the denser layer were below three times the velocities of the other layer, complex roots could still be found. This can be applied to the soil model used, as the velocities of the denser layer is roughly twice that of the less dense layer. The resulting Stoneley wave is one that leaks energy away from the interface as it propagates. This does appear to be the case here, as the waves travelling along the interface in figure 7.10 appear to lose amplitude as energy is propagated away from the interface, this energy then encounters another interface where it again appears to form a Stoneley wave that loses energy as it propagates. This effect appears to continue indefinitely, as there is no damping considered in this model.

This effect of the wave barrier does create some doubt about the reliability of the performance in a practical setting. The resulting fully reflecting waves appear to abuse the perfect horizontal interface as it is presented in the model. In reality, the interface will likely be far from perfectly horizontal. It should therefore be questioned whether this design would still be effective in a setting without perfectly horizontal layers. The performance of the barrier might suffer from imperfections or inclines in the interface.

7.3 Sensitivity to interface depth deviation

In the previous section it was shown that the introduction of multiple layers has significant effects on the optimal topology of the wave barriers. Moreover, the validity and robustness of the discrete and perfectly horizontal modelling of these interfaces with respect to the performance of the optimized wave barriers in practical settings was questioned. In practical settings the soil

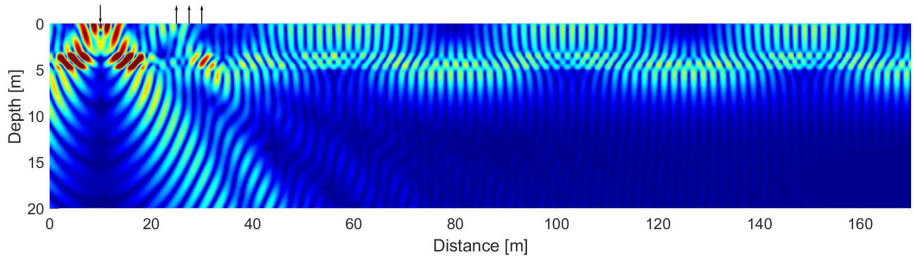

(a) $\hat{\mathbf{u}}_{\text{real}}$ without barrier

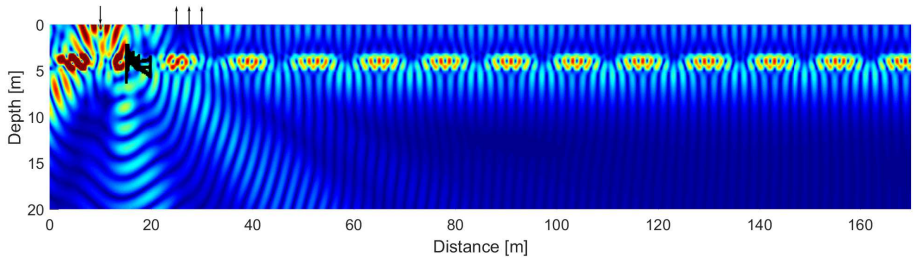

(b) $\hat{\mathbf{u}}_{\text{real}}$ with barrier

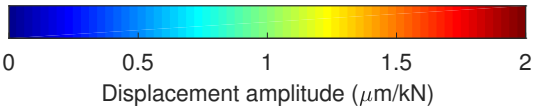

Figure 7.10: Comparison of $\hat{\mathbf{u}}_{\text{real}}$ with and without the barrier optimized for the wAVG objective function in the three-layered soil profile for a 50 Hz source.

properties are determined through on-site tests. Tests even small distances apart can result in relatively large variations in soil properties and layer depths. Layers will never be perfectly horizontal, have fully discrete interfaces or be at the exact depth as used in the model. Similarly, the material properties of the soil will never be exactly as used in the model. This section takes a first step into examining the sensitivity of the designed wave barriers to changes in the soil model.

The immediate concern here is reserved for deviations of the interface depths. The previous sections showed the significance of the addition of an interface. For the two-layered soils the interface impacted the design of a barrier largely through reflecting the shear waves back towards the receivers. For the three-layered soil profile the embedded layer of softer soil appeared to be used as a wave guide to ensure that the waves would no longer reach the receivers at the surface. Especially in this latter case, changes to the interface depth is expected to have a significant influence on the effectiveness of the barrier. The sensitivity was tested for the wave barriers optimized for the weighted average objective function for each of the three soil profiles. The value for the objective function was determined for the wave barriers by deviating the depth of the interface from 1 meter higher than modelled (-1 m) to 1 meter lower than modelled (+1 m). The results are depicted in figure 7.11 depicts the effect that deviations of the interface depth up to 1 m have on the effectiveness of the wave barrier.

Each of the wave barriers shows a diminished effectiveness resulting from deviations in the interface depth. It can be observed that the barriers for the two-layered profiles exhibit a much lower diminishing of effectiveness with deviation of the interface depth when compared to the barrier for the three-layered soil profile. The weighted average of the energy reduction ratio rises from 0.33 to 0.68 for the three-layered soil if the embedded soil layer deviates by 1 meter (see also table 7.3). In contrast, the weighted average energy reduction for the two-layered soil profiles changes very little with the same deviations. Moreover, for the two-layered soil profile with interface depth at 10 m, there is hardly any difference as the interface depth increases.

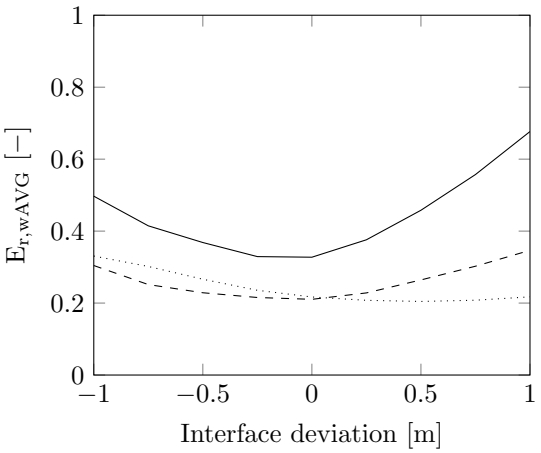

Figure 7.11: Sensitivity of the wAVG objective function value to deviation of the interface depth for the two-layer soil profile with interface at 10 m depth (·····), the two-layer soil profile with interface at 4 m depth (- - -) and the three-layer soil profile (——).

Deviation	Two-layer (10)	Two-layer (4)	Three-layer
-1	0.33	0.30	0.50
0	0.22	0.21	0.33
1	0.22	0.35	0.68

Table 7.3: Sensitivity of the wAVG objective function value to deviation of the interface depth for the different soil profiles

7.4 Summary

In order for a optimization tool for wave barriers to be useful in engineering practice, the implementation of a layered soil model is a necessity. The implementation of a layered soil model was successful, as long as the condition for the PML were met. These conditions were assured throughout this chapter by observing the dispersion curves for the soil models.

Chapter 2 showed that interfaces between layers result in reflections and refractions of plane waves. Additionally, the Rayleigh wave propagation would be affected The algorithm for the topology optimization of wave barriers was applied to three different soil profiles under a vertical load. For all three profiles the optimization generally resulted in the placement of a relatively large part of the allowed barrier volume in the softer soil layers. In each case, the optimized wave barrier showed an improvement on the objective function when compared to the reference barrier.

Comparison between a wave barrier optimized for a homogeneous soil with a wave barrier optimized for a two-layered soil profile showed that the wave barrier designed for the two-layered profile accounts for the reflections from the interface. Extra material was added to impede waves that would otherwise reflect from the interface. In contrast, the wave barrier optimized for a homogeneous soil ignored these waves allowing reflections from the interface to reach the receiver area.

In a three-layered soil profile the wave barrier appeared to divert a part of the energy that was initially present in the upper stiff layer to the embedded softer layer. This showed the necessity to include the displacements below the surface in the objective function if the structure in question is for instance founded on piles. It also indicated that the perfectly horizontally layered soil profile used in the optimization might be abused by the wave barrier. The latter point would require additional investigation to evaluate the influence of imperfections or inclinations in the interfaces on the effectiveness of the wave barriers designed using perfectly discrete interfaces.

Chapter 8

Manufacturability of optimized design

If the topology of all the optimized wave barriers discussed so far have one thing in common, it is that they would all be relatively difficult to manufacture. The optimized barriers were often of a complex, nondescript form. In some cases even containing shapes that fully enclosed a part of the soil. These forms would be difficult, if not impossible to construct. Especially considering the fact that the barriers would be constructed in the ground. Even if construction is possible, the cost-effectiveness when compared to regular straight barriers would be questionable. The optimization mtehod as-is is therefore not useable for practical application in the industry. With this in mind two methods were investigated that can be used to increase the manufacturability:

- Geometrically robust topology optimization
- Vertical density filter

The application of both methods is explained in further detail in the following two sections. The third section of this chapter shows the results when the methods are applied to the models shown in the previous chapter.

8.1 Geometrically robust topology optimization [1]

Previous studies showed that the optimized wave barriers could be very sensitive to geometric imperfections [19]. Small deviations in the design resulted in significant detrimental effects on the effectiveness of the wave barrier. In order to remedy this, a robust topology optimization approach was used. The robust approach consists of optimizing using three different projection threshold values in the projection filter (see subsection 5.2.3 on page 51). Recall that the projection filter forces densities above the projection threshold closer to one and below the projection threshold closer to zero. A lower projection threshold (0.25) results in a dilated version of the design, the regular projection threshold (0.5) results in an intermediate design and a higher threshold (0.75) results in an eroded version of the design (see figure 8.1).

In the robust topology optimization approach a min-max objective function is used that includes all three versions of the design. The effect of this is that in each iteration, the worst performing version is optimized for. The result is that the final design is much less sensitive to small geometric imperfections. A benefit of this is that it was possible to simplify the final design

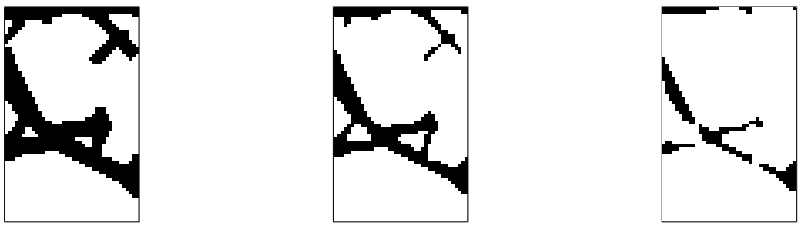

(a) Dilated
$F_{wAVG} = 0.23$

(b) Intermediate
$F_{wAVG} = 0.22$

(c) Eroded
$F_{wAVG} = 0.59$

Figure 8.1: Dilated, intermediate and eroded version of the design and their objective function value.

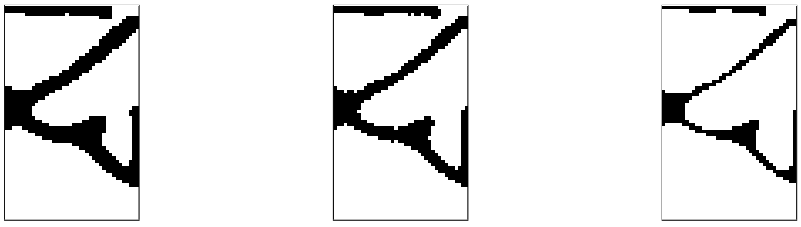

(a) Dilated
$F_{wAVG} = 0.28$

(b) Intermediate
$F_{wAVG} = 0.26$

(c) Eroded
$F_{wAVG} = 0.27$

Figure 8.2: Dilated, intermediate and eroded version of the design and their objective function value using robust topology optimization.

in a post-processing step, without heavily impacting the effectiveness of the barrier. This allowed a manual increase of the manufacturability of the wave barrier. Translated to an optimization problem this becomes (with the superscripts indicating **d**ilated, **i**ntermediate and **e**roded):

$$\begin{aligned} \min_{\rho} \quad & \max\left[F(\rho^d), F(\rho^i), F(\rho^e)\right] \\ \text{s.t.} \quad & S(\bar{\rho}^d)u^d = F \\ & S(\bar{\rho}^i)u^i = F \\ & S(\bar{\rho}^e)u^e = F \\ & \sum_{e=1}^{N_e} V_e \bar{\rho}_e \leq V_{max} \end{aligned}$$

The resulting wave barrier design shows a significant change in topology. The new designed has a reduced effectiveness but this is accompanied by a much lower sensitivity to changes in the thickness of the design (figure 8.2).

8.2 Vertically oriented barrier

The second approach is an adaptation of a density filter designed to incorporate maximum overhang constraints for additive manufacturing [70]. In order to enforce maximum overhang

constraints, each density is multiplied with a support factor. The support factor is based on the average density of a subset of elements related to the considered element. Which elements belong to the subset of support elements is defined based on a user-defined radius and the maximum overhang angle based on the print material. The weighted average density of this subset is determined using a function similar to the density filter described previously. Then a projection threshold function is used to approach a Heaviside function such that the support factor approaches 1 when the weighted average density of the supporting elements is above a certain value or approaches 0 when the weighted average is below a certain value. The result is that material is only placed in the optimization process when an element is considered supported and when material placement would improve the objective function.

A relaxed version of the method described above is applied here with some adaptations. First, the subset of supporting elements contains only the element directly above the considered element. Second, the density of the element above the considered element is not passed through a threshold function. This allows the optimization algorithm a greater freedom, improving the convergence. The result is that the density of each element is simply multiplied by the vertically filtered density of the element above. With $\hat{\rho}_j$ representing the vertically filtered density of element j, the vertical filter can be described as:

$$\hat{\rho}_j = \rho_j \hat{\rho}_i \qquad \text{for } i \in N_v^j \tag{8.1}$$

where an element is in N_v^j if $z_j - z_i = b$ and $|x_j - x_i| = 0$, with b as the element size of the design domain, z as the depth of the center of an element and x as the horizontal coordinate of an element.

This is effectively a penalization of elements for which the element above has a lower density, preventing any element from having a greater density than the element above. This should facilitate a vertically oriented wave barrier that should be easier to construct than barriers at random depths in the ground.

The sensitivity analysis is changed in the following way to incorporate the vertical filter:

$$\frac{\delta F}{\delta \rho_i} = \sum_{k \in N_V^i} \left(\sum_{j \in N_b^k} \left(\frac{\delta f}{\delta \bar{\rho}_j} \frac{\delta \bar{\rho}_j}{\delta \tilde{\rho}_j} \frac{\delta \tilde{\rho}_j}{\delta \hat{\rho}_k} \frac{\delta \hat{\rho}_k}{\delta \rho_i} \right) \right) \tag{8.2}$$

Note that the set $N_v^j \neq N_V^j$. The vertical subset indicated with a lower case v is as defined above and contains only the element directly above element j. The vertical subset indicated with an upper case V contains element j and all other elements directly below in a straight vertical line. The set N_e^k is the set of neighboring elements as defined previously for the density filter (see chapter 5) specified for element k.

The derivative of the vertically filtered $\hat{\rho}$ with respect to the density ρ is given as:

$$\frac{\delta \hat{\rho}_k}{\delta \rho_i} = \begin{cases} \hat{\rho}_l & \text{for } i = k \text{ and } l \in N_v^k \\ \rho_k \frac{\delta \hat{\rho}_l}{\delta \rho_i} & \text{for } i \neq k \text{ and } l \in N_v^k \\ 0 & \text{otherwise} \end{cases} \tag{8.3}$$

The second row in equation 8.3 shows the embedded nature of this approach. This can be easily dealt with by calculating the sensitivities of the vertically filtered density layer by layer.

Combining this vertical filter with the robust optimization approach described above should facilitate a greatly increased manufacturability of the optimized barriers. As a final step, in post-processing the barrier can be manually simplified. Because of the use of the robust topology optimization approach, the final design should be relatively insensitive to small changing made

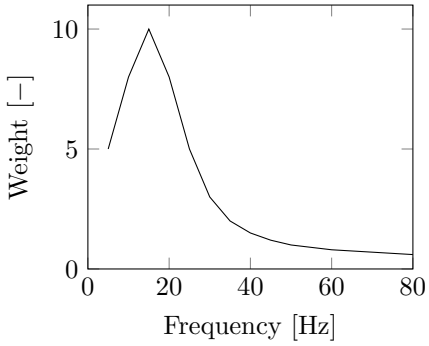

Figure 8.3: Frequency weight distribution

in this simplification step. Although some care must be taken as the greater the simplifications, the greater the effect on the wave barrier effectiveness will be.

8.3 Results

In this section the progression of the topology of the optimized wave barriers is shown when manufacturability is incrementally increased. First only the robust topology optimization is applied, followed by the combination with the vertical density filter. Lastly an example of a simplified version of the design is shown. This progression is shown for the following cases:

- Single harmonic frequency for the two-layered soil model with an interface at 10 meters depth
- Weighted average objective function for the two-layered soil model with an interface at 10 meters depth
- Weighted average objective function for the two-layered soil model with an interface at 4 meters depth
- Weighted average objective function for the three-layered soil model

As a reminder, the weights that are used in the weighted average objective function are depicted in figure 8.3.

Manufacturable barriers using the single harmonic frequency objective function

Figure 8.4 shows this progression for a wave barrier optimized for a 50 Hz source in a two-layered soil profile with the interface at a depth of 10 m. The leftmost figure shows the topology of the reference barrier for comparison. The final value of the objective function (energy reduction) is given below the figures as well. The topology of the geometrically robust wave barriers differs significantly from that of the standard optimized wave barrier. It is also visible that the vertical filter results in wave barriers that would allow for relatively easy construction using for instance a jet-grouting method. Moreover, the combination of a geometrically robust, vertical barrier allows for some simplifications without large detrimental effects to the barrier effectiveness. The energy reduction ratio achieved by the resulting simplified wave barrier is 0.04. Compared to the ratio of 0.12 for the reference wave barrier it shows that even with the heavily increased constraints to the design, a significant improvement over the reference barrier is still possible.

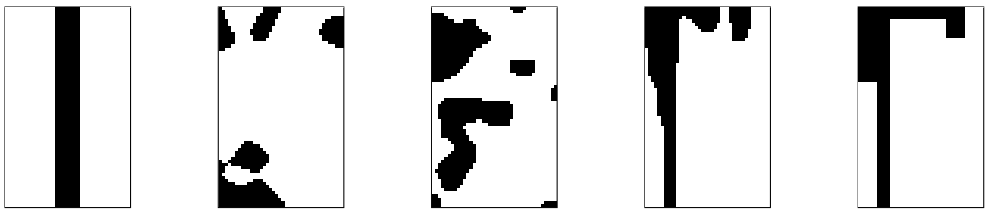

(a) Reference $F_{50} = 0.12$ (b) Standard $F_{50} < 0.01$ (c) Robust $F_{50} < 0.01$ (d) Vertical $F_{50} = 0.01$ (e) Simplified $F_{50} = 0.04$

Figure 8.4: The shape of wave barriers optimized for a 50 Hz source in a two-layer soil with interface at 10 m depth with different levels of manufacturability.

Manufacturable barriers using the weighted average objective function

The same process was applied to weighted average objective function in the same two-layer soil (figure 8.5). The frequency range and weights are identical to those used in the previous chapters. The final simplified wave barrier is of a relatively simple design while still providing a significant increase in the objective function ($F_{wAVG,ref} = 0.44$ to $F_{wAVG,simple} = 0.31$). The design is essentially a combination of two straight vertical barriers connected horizontally at the surface. Figure 8.6 compares the energy reduction ratio of the simplified optimized wave barrier with the reference barrier. Over the entire frequency range, the simplified optimized wave barrier appears to perform only marginally better than the reference barrier. However, when taking into account that the frequencies around 15 Hz were the most heavily weighted (figure 8.3, the simplified wave barrier shows a significant improvement over the reference barrier.

Figure 8.7 compares the effects of the reference and the simplified wave barrier on the real part and the absolute of the displacement found for a 15 Hz harmonic source. The real part of the displacements with the simplified barrier appears to suggest that there might be some correlation between the distance of the two vertical elements of the barrier and the wavelength associated with the most heavily weighted frequency. Increasing this frequency from 15 to 16 Hz did lead to a very similar topology that was slightly narrower. Specifically the width decreased from 4.625 m total width to 4.5 m total width. Table 8.1 compares the width of the wave barriers with the wavelengths. Interestingly, the ratio for the shear wavelength corresponds to the cosine of the 45 degree angle around which most of the energy of the shear wave was propagating and in which direction the width of the wave barrier would approach one full wavelength for both frequencies. However, further increase of the highest weighted frequency gave way to a topology that no longer featured two separate vertical elements.

Figures 8.8 and 8.9 show the same progression of the wave barrier for the shallow two-layered soil profile and the three-layered soil profile. In both profiles, due to the extra constraints, the final design hardly resembles the initial optimized wave barrier. Moreover, for the three-layered soil profile, it appears that, when taking into account the vertical constraints, the reference barrier is in fact the optimal topology. For the shallow two-layered profile the simplified wave barrier does differ significantly from the reference barrier. As seen in previous chapters, more material is located in the soft layer up to 4 meters depth. However, while the standard and robust optimization place material solely in this softer layer, the wave barrier designed through the vertical optimization penetrates the stiffer half-space.

	15 Hz		16 Hz	
	λ [m]	Ratio [-]	λ [m]	Ratio [-]
R-wave	6.8	0.68	6.3	0.71
S-wave	7.1	0.65	6.7	0.67

Table 8.1: Wavelength (λ) and ratio between wave barrier width and wavelength for with the frequency for which the energy reduction has the greatest weight shifting from 15 Hz to 16 Hz

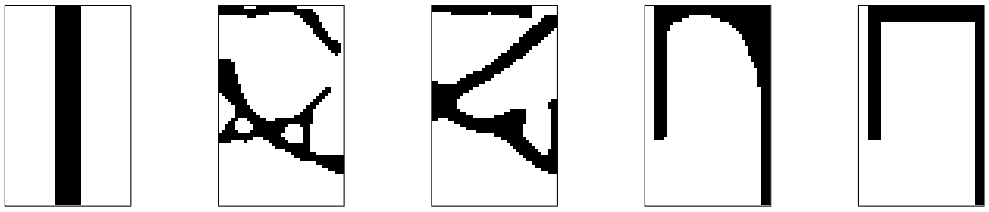

(a) Reference $F_{wAVG} = 0.44$ (b) Standard $F_{wAVG} = 0.22$ (c) Robust $F_{wAVG} = 0.26$ (d) Vertical $F_{wAVG} = 0.26$ (e) Simplified $F_{wAVG} = 0.31$

Figure 8.5: The shape of wave barriers optimized for the weighted average objective function in a two-layer soil with interface at 10 m depth with different levels of manufacturability.

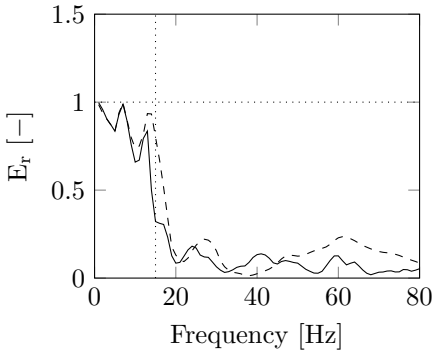

Figure 8.6: Performance of the wAVG simplified wave barrier (——) compared to the reference barrier (- - -)

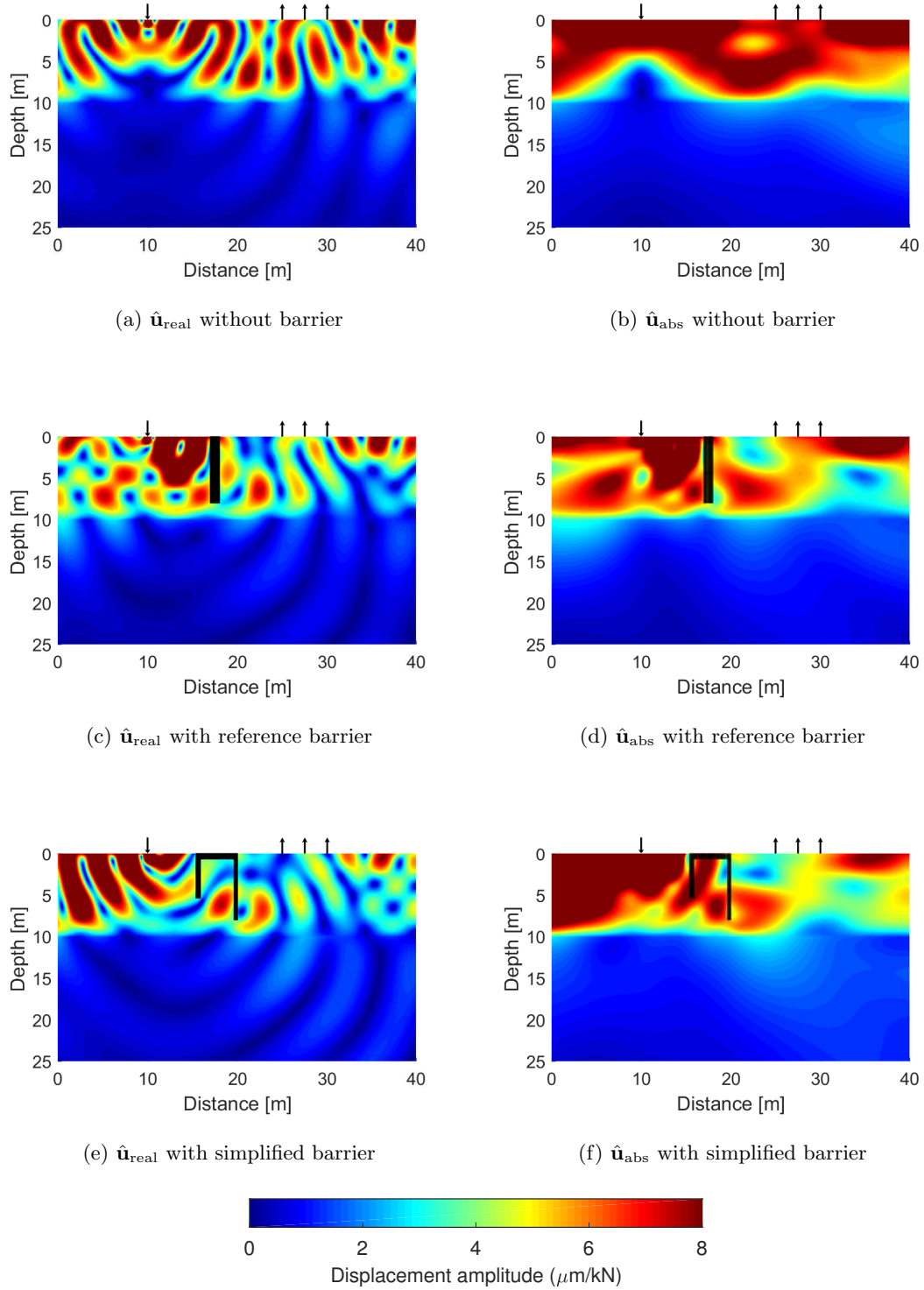

(a) $\hat{\mathbf{u}}_{\text{real}}$ without barrier

(b) $\hat{\mathbf{u}}_{\text{abs}}$ without barrier

(c) $\hat{\mathbf{u}}_{\text{real}}$ with reference barrier

(d) $\hat{\mathbf{u}}_{\text{abs}}$ with reference barrier

(e) $\hat{\mathbf{u}}_{\text{real}}$ with simplified barrier

(f) $\hat{\mathbf{u}}_{\text{abs}}$ with simplified barrier

Figure 8.7: $\hat{\mathbf{u}}_{\text{real}}$ and $\hat{\mathbf{u}}_{\text{abs}}$ for reference and simplified wave barrier subject to a 50 Hz source.

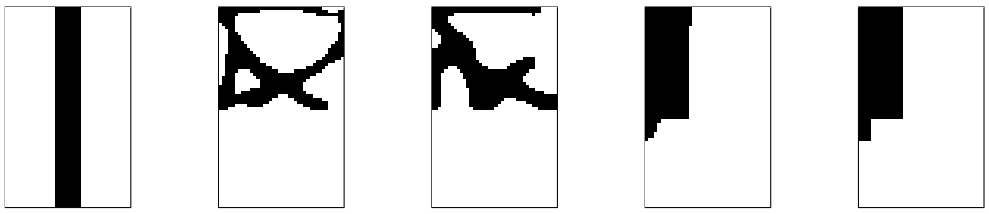

(a) Reference $F_{wAVG} = 0.53$ (b) Standard $F_{wAVG} = 0.21$ (c) Robust $F_{wAVG} = 0.22$ (d) Vertical $F_{wAVG} = 0.36$ (e) Simplified $F_{wAVG} = 0.36$

Figure 8.8: The shape of wave barriers optimized for the weighted average objective function in two-layer soil profile with interface depth at 4 m with different levels of manufacturability.

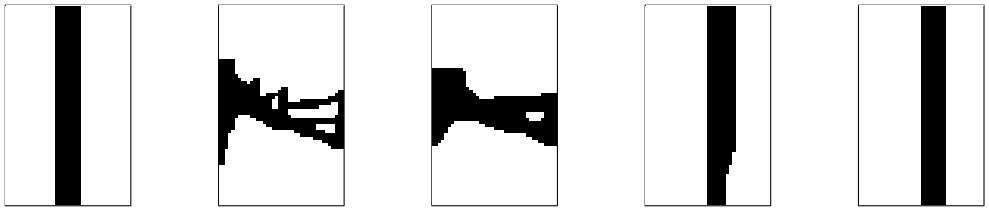

(a) Reference $F_{wAVG} = 0.52$ (b) Standard $F_{wAVG} = 0.33$ (c) Robust $F_{wAVG} = 0.35$ (d) Vertical $F_{wAVG} = 0.51$ (e) Simplified $F_{wAVG} = 0.52$

Figure 8.9: The shape of wave barriers optimized for the weighted average objective function in three-layer soil profile with different levels of manufacturability.

8.4 Summary

This chapter focused on increasing the manufacturability of the optimized barriers. The robust optimization approach was combined with a customized vertical filter. The resulting wave barriers showed a large increase in manufacturability, especially after a post-processing simplification step. However, the manufacturability did come at the cost of effectiveness. Still, for all considered cases the optimization algorithm converged to either a final design that was an improvement of the reference barrier or identical to the reference barrier. It can therefore still be used to give some suggestions about the optimal designs and to see if a different topology exists that is nearly as easy to construct as the reference barrier, but is more effective.

Part V

Discussion

Chapter 9

Discussion

9.1 Discussion of results

The goal of this thesis was to create a topology optimization tool that can be used to help design wave barriers in engineering practice. The tool was based on a method for topology optimization of wave barriers found in literature. It was established that, in order for the tool to be usable in engineering practice, improvements were required on two fronts:

- The model must be able to support the implementation of layered soils
- The manufacturability of the final designs for the wave barriers should be increased

It was shown that the implementation of a layered soil could be safely applied using the same boundary layers as Van Hoorickx et al. (2016), as long as it was monitored that forward and backward propagating waves would not occur simultaneously. This was done by determining the dispersion curves of each profile that was used. Observing these curves showed that for each case considered in this thesis, only forward propagating waves were found over the entire frequency range.

Considering the improvements that would be made to the model, as well as the need to reduce lower frequency vibrations, the following research questions were formed in the introduction of this thesis:

1. Does topology optimization offer significant benefits when the aim is to reduce low frequency vibrations?
2. In what ways does the introduction of a layered soil model affect the topology of an optimized wave barrier?
3. How sensitive are the designed wave barriers to changes of the interface depth?
4. How can the manufacturability of the designed barriers be increased and what effects does this have on the wave barrier effectiveness?

Each of these question and its relevant results are discussed in this section.

Does topology optimization offer significant benefits when the aim is to reduce low frequency vibrations?

The question regarding the reduction of low frequency vibrations was first investigated by comparing optimizations for different frequencies. It was observed that, in agreement with literature, lower frequency vibrations were more difficult to reduce than higher frequency vibrations. A wavelength dependent model was created to show that this effect was largely dependent on the encountered wavelengths. Again this was in agreement with literature, which argued for a minimum depth and width of wave barriers relative to the wavelength for adequate vibration reduction. By incrementally increasing the design domain dimensions and the volume constraint as a function of the wavelength, some insight was granted into the required dimensions. Increasing the design domain and allowed volume with regards to the wavelength resulted in a greater energy reduction. Interestingly, increasing the volume beyond 12% of the wavelength squared and increasing the depth and width beyond 0.75 times the wavelength was ineffectual. The result however, indicates that even when using the benefits of topology optimization, the maximum achievable effectiveness of a wave barrier remains heavily dependent on its dimensions relative to the wavelength. For waves with a greater wavelength, significant energy reduction using wave barriers of a concrete-like material does not appear to be possible without resorting to large dimensions.

In what ways does the introduction of a layered soil model affect the topology of an optimized wave barrier?

The implementation of the layered soil model allowed for the investigation of the effects of different layers on the topology of an optimized wave barrier. Three distinct observations could be made. Material appeared to be more beneficial in regions where the stiffness ratio was larger. This was in agreement with findings from parametric studies suggesting that barriers were more effective with higher stiffness ratios. It was however not determined whether the stiffness ratio itself is the deciding factor or perhaps some other ratio connected to the stiffness such as the impedance ratio or the wave speed ratios. The placement of material in the softer layer could also be related to the confinement of much of the energy to the softer layers in the models that were tested. Placement of material in regions where it will not interact with the energy propagating towards the receivers would likely be ineffective.

A second observation was made that pertained to the waves reflecting from the interface. Shear waves propagating at an angle of roughly 40-45 degrees, that could be ignored in a homogeneous soil model became important in a layered soil model as they would reach the receivers after reflecting from the interface. The optimization algorithm prevented this by placing material in the path of the downward propagating shear waves.

The three-layered soil model showed a third way in which multiple layers might affect the optimal topology of a wave barrier. In this soil model, the optimized wave barrier appeared to use the softer embedded layer as a waveguide by guiding more energy into this layer. The result was that much of the energy was contained within the softer layer, never reaching the receivers at the surface.

It was also expected that the introduction of a layered soil model would alter the propagation of the Rayleigh waves, but this was not observable in the models that were used. In the two-layered soil model, longer wavelengths approached the Rayleigh wave velocity of the stiffer

half-space, however, other interaction with the optimal topology such as the ratio of a stiffness like quantity between the barrier and the different soil layers interferes with observations that could be made about the effects the different Rayleigh wave velocities have on the barrier topology.

How sensitive are the designed wave barriers to changes of the interface depth?

In the introduction some concerns were stated about the robustness of the designs when a layered soil model would be introduced. The tool optimized wave barriers for a specific soil profile with specific material properties for both the barrier material and the soil. These parameters are often relatively uncertain. It was questioned whether the wave barriers that were designed would still function in soils that differed on certain aspects from the model that was used in the optimization.

In this thesis the investigation of the sensitivity was focused on issues introduced by the implementation of a layered soil. Specifically, it was investigated whether the effectiveness of the optimized wave barriers was sensitive to changes of the interface depth. The wave barriers optimized for the two-layered soil models showed relatively little sensitivity to the interface depth. In contrast, the wave barrier optimized for three-layered soil model was incredibly sensitive to changes of the interface depth. This is explained by observing the interaction between the wave barrier and the soil profile. For the two-layered soil, and the interface at a depth of 10 meters in particular, the wave barrier prevented the reflection of waves from the interface by placing material in the path of the shear wave. After placement of the wave barrier, the interaction between the layer interface and the propagating waves is minimized. Deviation of the depth of the interface still did not result in any significant interaction with the propagating waves, and thus did not significantly affect the wave barrier effectiveness. In contrast, the wave barrier designed for the three-layered soil appeared to make use of the embedded layer as a waveguide. After the wave barrier was introduced, the soil interface was interacting with the propagating waves and used to reduce vibration in the target area. The amount of interaction between the interface and the propagating waves after implementation of the wave barrier appears to be a large contributing factor for the sensitivity of the optimized wave barrier design to changes in the depth.

How can the manufacturability of the designed barriers be increased and what effects does this have on the wave barrier effectiveness?

The previous studies showed the increased effectiveness of wave barriers. Sadly the designs of the optimized wave barriers were often very complex, and would be very costly to manufacture. In this thesis the manufacturability of the optimized designs was increased by combining a robust topology optimization approach with a vertical density filter. The results were wave barriers that were relatively easy to manufacture, while still providing a significant increase in effectiveness. Except for the three-layered soil model where the manufacturable version of the wave barrier reverted to the reference barrier. A probable cause for this result is the discrepancy between the horizontally oriented initial optimized design and the vertical constraints added through the vertical density filter. Apparently, no vertical design that was more effective than the reference barrier could be found. In conclusion, the attempt at increasing the manufacturability was

met with moderate success. In each case the increased manufacturability came at the cost of effectiveness. In the two-layered soils, the final design was still a significant improvement over the reference barrier, without a significant increase in complexity, while in the three-layered soil the reference wave barrier was determined to be the optimal manufacturable wave barrier.

9.2 Limitations

It is important to realize that the model that was used made some concessions and assumptions because the subjects were either outside of the scope of this thesis or because of restrictions regarding the computation time. The most pressing limitations that are discussed here are:

- Reduced accuracy due to limited resolution
- 2D model and simplified loading
- Sensitivity of the topology optimization process to model changes
- No consideration of soil-structure interaction

Reduced accuracy due to limited resolution

The element size for the model used in this thesis was based on recommendations from literature. In general the consensus appeared to be that at least 6 elements per wavelength were necessary, while 8-10 elements was commonly recommended and applied. In this thesis a comparison was made with Lamb's problem using the soil parameters as prescribed in the previous optimization studies. A convergence study to the analytical solution to Lamb's problem showed that 20 elements per wavelength was still a significant improvement over 10 elements per wavelength. However, considering computational constraints and recommendations from literature, the decision was made to use a minimum of 10 elements per wavelength. It was thought that the amplitude differences between the analytical solution and the numerical solution with 10 elements per wavelength would not significantly affect the optimized topologies as the energy reduction ratio was used to formulate an objective function, rather than an absolute maximum vibration criterion.

In order to estimate the effects of the chosen resolution, the energy reduction ratios of the optimized design of the wave barrier designed for the two-layered soil model with an interface at 10 meters depth was determined using three different maximum element sizes corresponding to 10, 20 and 40 elements per wavelength. The ratios of the energy reduction over the frequency range between the different resolutions are given in figure 9.1. The differences between resolutions are very significant. In the worst case found here, the energy reduction ratio was 25% lower when using 20 elements per wavelength compared to 10 elements per wavelength.

The resolution problem was further examined by optimizing a wave barrier for the same soil using a resolution of 20 elements per wavelength. The resulting wave barriers are shown in figure 9.2. The topologies of both wave barriers are very similar as are the achieved objective function values. The difference between the barriers can be partly explained by the increased resolution of the design domain. This allows for more fluid curves in the design which can affect the use of material. Taking this into account, a tentative conclusion is drawn that, although the reduction ratios might differ with increasing resolutions, the topology of the design does appear to change significantly. The robustness of the optimization algorithm with respect to the increase of the resolution does require further investigation.

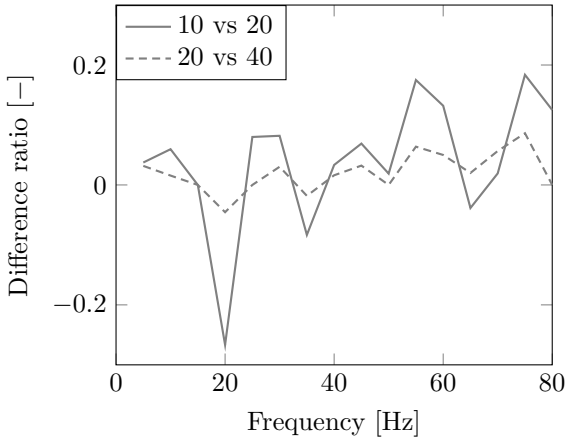

Figure 9.1: Difference in energy reduction between different resolutions

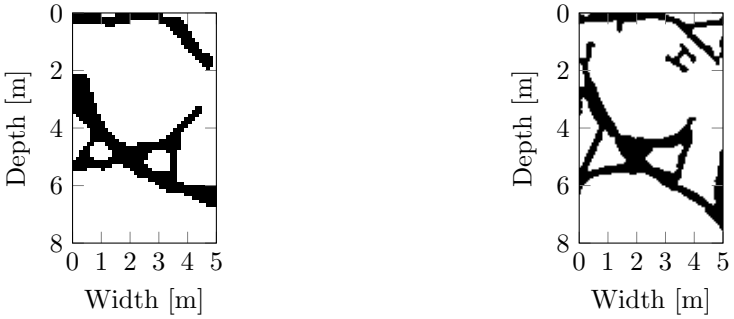

(a) Wave barrier for 10 elements per wavelength ($F_{wAVG} = 0.22$)

(b) Wave barrier for 20 elements per wavelength ($F_{wAVG} = 0.21$)

Figure 9.2: Comparison of the optimized topologies using a different minimum number of elements per wavelength

2D model and simplified loading

In order to limit the computation time a 2D model was used. This only allows for the optimization of the cross-section of the wave barrier. The use of a 2D model also forces a simplification of the loading. The environmental loading is always represented as an infinite line load. In reality, this would only be a valid approximation in cases where the distance between the source and the receivers is small relative to the length of the source. This might be true in some cases concerning railway traffic, but even then, an infinite line load is a significant simplification over the complex system involved in wave propagation induced by railway traffic.

The model also simplified the inhomogeneity of the soil as a number of horizontal layers. These layers were perfectly horizontal and of consistent thickness over the entire profile. Properties such as these might have allowed for abuse by the optimization algorithm. For instance, in the three-layered soil profile the embedded layer appeared to be used as a waveguide. Using an embedded layer in such a way might be dependent on the idealized representation in the model.

Sensitivity of the topology optimization process to model changes

Chapter 7 investigated the sensitivity of the optimized design to changes in the interface depths. The results showed that depending on the model, the optimized design could be very sensitive to these changes. Moreover, only one aspect was investigated with regards to the sensitivity of the model. Other aspects to which the optimized design might be sensitive include the material properties of the soil and the wave barrier, the angle of the interfaces, the discreteness of the interfaces and possibly more. In jet-grouting for instance, the properties of the wave barrier are often not uniform over the height. This could very well affect the optimized designs. The embedded layer in the three-layered soil model was used as a waveguide for some frequency sources. An angle in the interface might completely change the effects of the wave barrier. After the topology optimization therefore, possible sensitivities should always be considered.

No consideration of soil-structure interaction

In general, if a structure is present, the response of the soil due to an external load influences the response of the structure. However, the response of the structure also influences the response of the soil. This interdependent behaviour is called soil-structure interaction. In this thesis, no structure was modelled, and as a result the soil-structure interaction is not taken into account, affecting the accuracy of the optimized wave barrier.

The absence of a structure in the model also affects the optimized topology as it limits the variables that can be used in the objective functions. In this thesis, the effectiveness of the wave barriers was determined by evaluating the energy reduction at the surface. By including a structure in the model, the energy reduction within the structure can be used instead. Moreover, the results in this thesis already showed that the use of receivers at the surface was abused in some situations by guiding the energy away at a distance below the surface. If a building with foundation is present this energy would still reach the structure.

Whether the addition of a structure is necessary is dependent on mostly on the significance of the soil-structure interaction. In the case where foundation piles are present and the energy should be reduced below the surface as well, extending the receivers to a sufficient depth might prove to be an adequate solution if the soil-structure interaction is limited.

9.3 Future research

Recommended future research directions pertain in part to the limitations discussed above. Expanding the model to a 2.5D model would allow for the implementation of a moving load, increasing the accuracy of the loading. The soil-structure interaction too, can be interesting to investigate and would be relatively easy to introduce.

If safe application of a topology optimization tool for engineering practice is desired, the sensitivities require further exploration. Furthermore, it would be desirable to not only document the parameters to which the optimized designs are sensitive but also investigate methods to reduce these sensitivities. For the sensitivity of the optimized design to the deviation of the interface depth, the use of a robust topology optimization can be attempted. This robust optimization would implement three soil profiles. An intermediate profile representing the expected interface depths, and two deviating soil profiles. If the algorithm then optimizes for the soil profile variant in which the wave barrier performs the worst, it should result in an optimized design that is less sensitive to deviations of the interface depth.

The results also showed a novel approach to the use of wave barriers to mitigate vibrations. As seen in the three-layered soil profile, under the presence of a soft embedded layer between two

stiffer layers, a wave barrier can be designed that uses the embedded layer as a waveguide for certain frequencies. The results appeared to indicate that the embedded layer was only usable as a waveguide if the thickness of the layer was large enough with respect to the wavelength. In the Netherlands clay layers of significant thickness can be found, indicating the possible use of these layers as a waveguide for relatively low frequency waves. The possibility of a new type of wave barrier that focuses on using these layers as a waveguide warrants further investigation.

Appendix A

Topology of wave barriers for wavelength dependent domain and volume

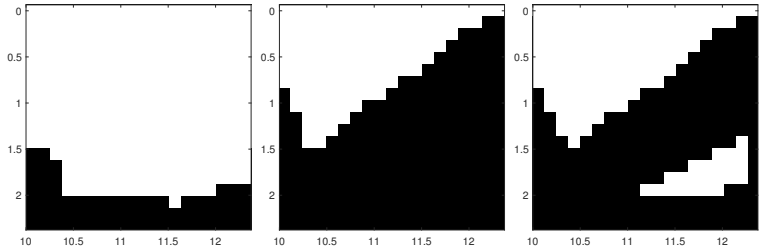

(a) $L_{\mathrm{D}} = 0.25\lambda_R$, $\mathrm{V}_{\max} = 0.0125\lambda_R^2$ (b) $\mathrm{L}_{\mathrm{D}} = 0.25\lambda_R$, $\mathrm{V}_{\max} = 0.0500\lambda_R^2$ (c) $\mathrm{L}_{\mathrm{D}} = 0.25\lambda_R$, $\mathrm{V}_{\max} = 0.0625\lambda_R^2$

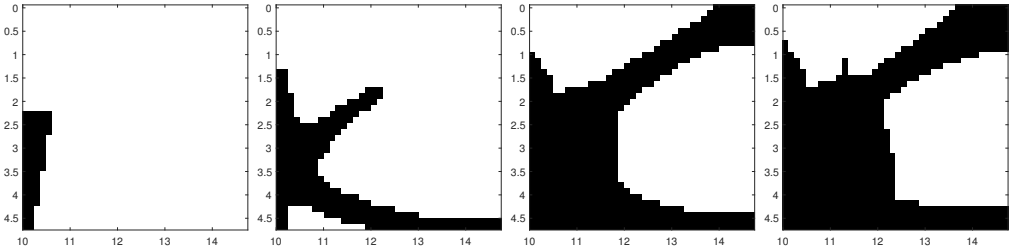

(d) $\mathrm{L}_{\mathrm{D}} = 0.5\lambda_R$, $\mathrm{V}_{\max} = 0.0125\lambda_R^2$ (e) $\mathrm{L}_{\mathrm{D}} = 0.5\lambda_R$, $\mathrm{V}_{\max} = 0.0500\lambda_R^2$ (f) $\mathrm{L}_{\mathrm{D}} = 0.5\lambda_R$, $\mathrm{V}_{\max} = 0.1125\lambda_R^2$ (g) $\mathrm{L}_{\mathrm{D}} = 0.5\lambda_R$, $\mathrm{V}_{\max} = 0.2000\lambda_R^2$

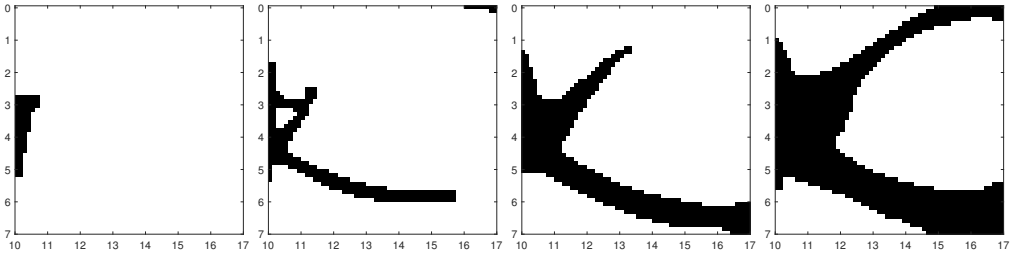

(h) $\mathrm{L}_{\mathrm{D}} = 0.75\lambda_R$, $\mathrm{V}_{\max} = 0.0125\lambda_R^2$ (i) $\mathrm{L}_{\mathrm{D}} = 0.75\lambda_R$, $\mathrm{V}_{\max} = 0.0500\lambda_R^2$ (j) $\mathrm{L}_{\mathrm{D}} = 0.75\lambda_R$, $\mathrm{V}_{\max} = 0.1125\lambda_R^2$ (k) $\mathrm{L}_{\mathrm{D}} = 0.75\lambda_R$, $\mathrm{V}_{\max} = 0.2000\lambda_R^2$

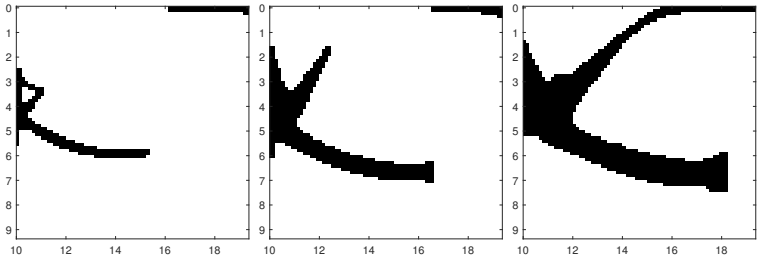

(l) $\mathrm{L}_{\mathrm{D}} = 1\lambda_R$, $\mathrm{V}_{\max} = 0.0500\lambda_R^2$ (m) $\mathrm{L}_{\mathrm{D}} = 1\lambda_R$, $\mathrm{V}_{\max} = 0.1125\lambda_R^2$ (n) $\mathrm{L}_{\mathrm{D}} = 1\lambda_R$, $\mathrm{V}_{\max} = 0.2000\lambda_R^2$

Figure A.1: Optimized wave barriers for different design domain and volume constraints.

Appendix B

Topology optimized wave barriers for two-layered soils

B.1 Soil profile 1

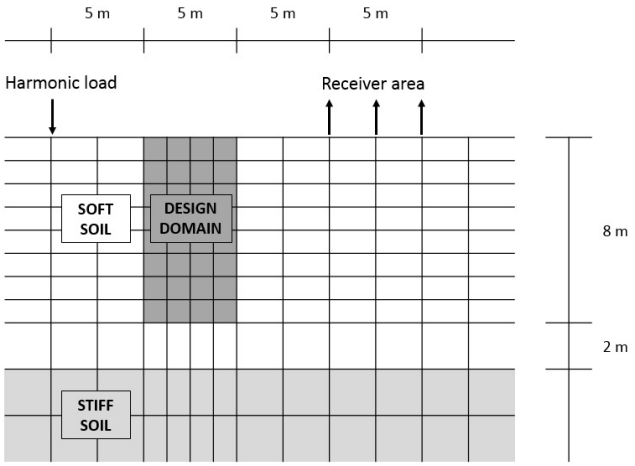

Figure B.1: Inner domain of model

Layer	Depth (m)	E mod. (MPa)	Density (kg/m^3)	Poisson's ratio (-)	C_p (m/s)	C_s (m/s)
1	10	50	1500	0.45	356	107
HS		250	2000	0.45	689	208

Table B.1: Soil properties of two-layered soil profile

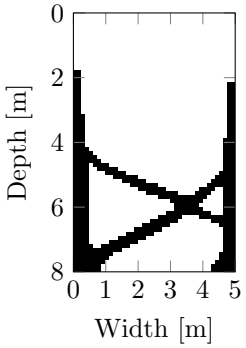

(a) Wave barrier for 5 Hz

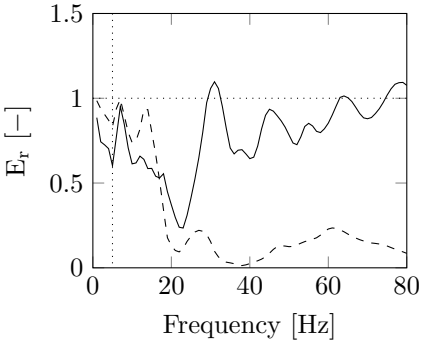

(b) E_r for 5 Hz

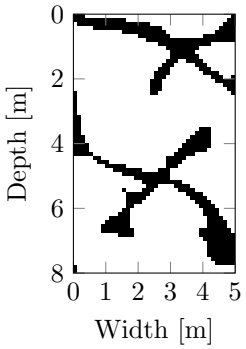

(c) Wave barrier for 25 Hz

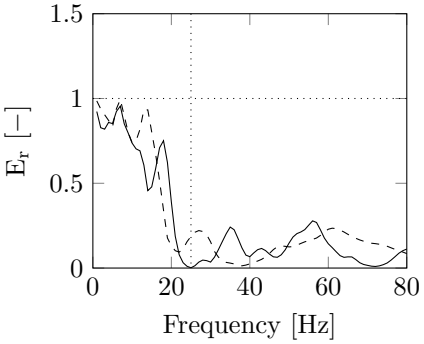

(d) E_r for 25 Hz

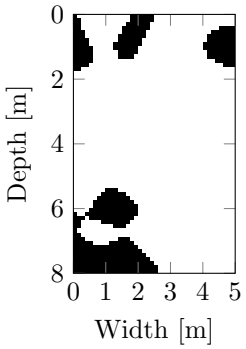

(e) Wave barrier for 50 Hz

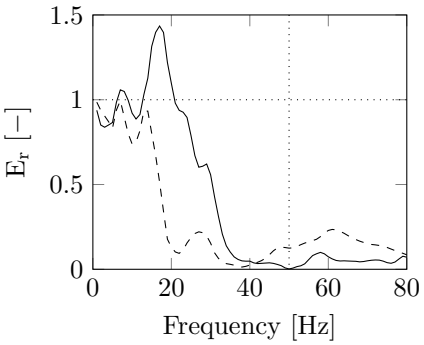

(f) E_r for 50 Hz

Figure B.2: The shape and performance of wave barriers optimized for single harmonic frequencies in a two-layer soil with interface at a depth of 10 m.

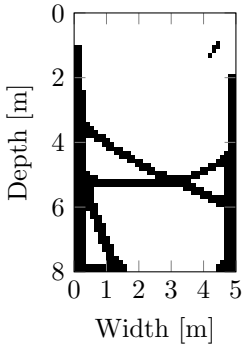

(a) Wave barrier for MINMAX

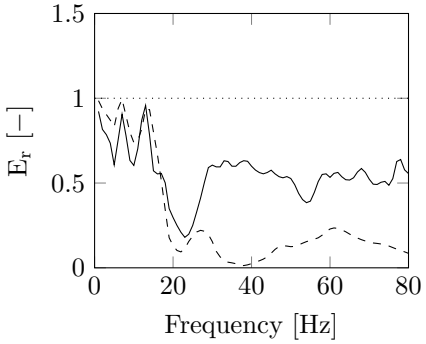

(b) E_r for MINMAX

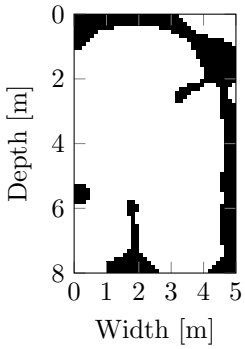

(c) Wave barrier for AVG

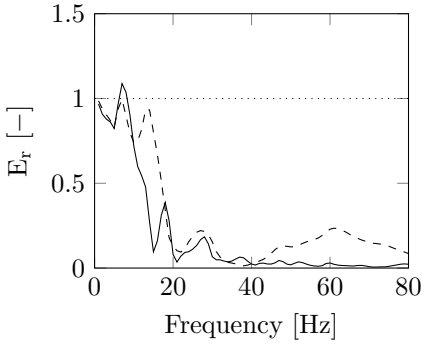

(d) E_r for AVG

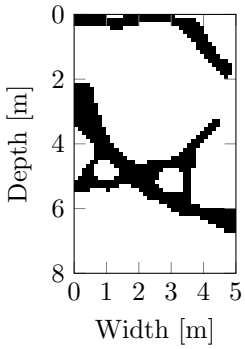

(e) Wave barrier for wAVG

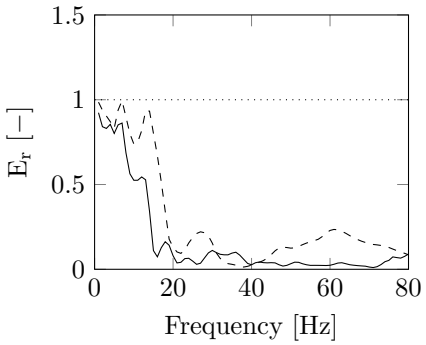

(f) E_r for wAVG

Figure B.3: The shape and performance of wave barriers optimized for single harmonic frequencies in a two-layer soil with interface at a depth of 10 m.

B.2 Soil profile 2

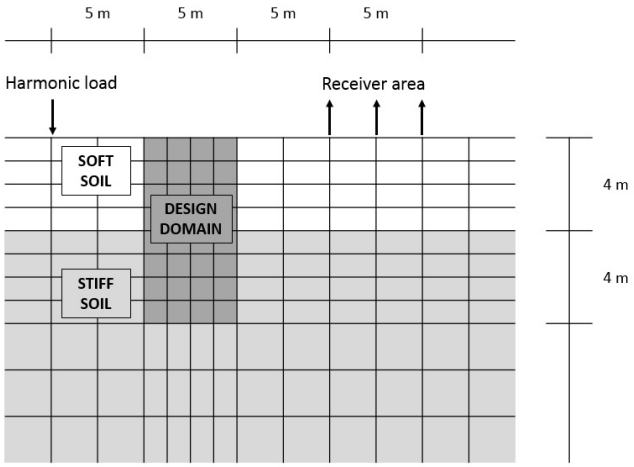

Figure B.4: Inner domain of model for soil profile 2

Layer	Depth (m)	E mod. (MPa)	Density (kg/m^3)	Poisson's ratio (-)	C_p (m/s)	C_s (m/s)
1	4	50	1500	0.45	356	107
HS		250	2000	0.45	689	208

Table B.2: Soil properties of two-layered soil profile 2

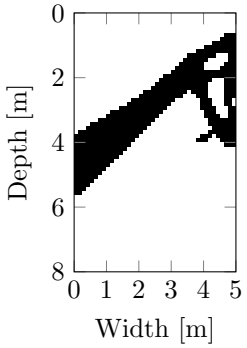

(a) Wave barrier for 5 Hz

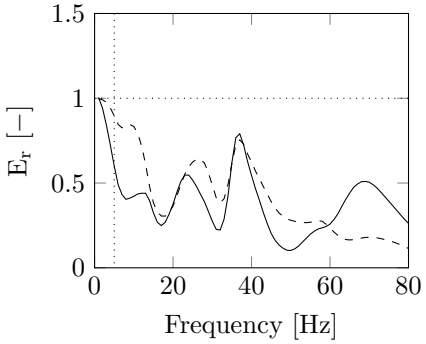

(b) E_r for 5 Hz

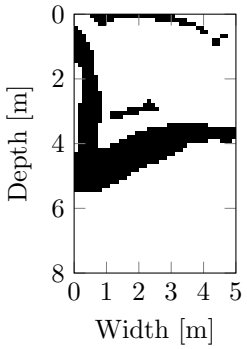

(c) Wave barrier for 25 Hz

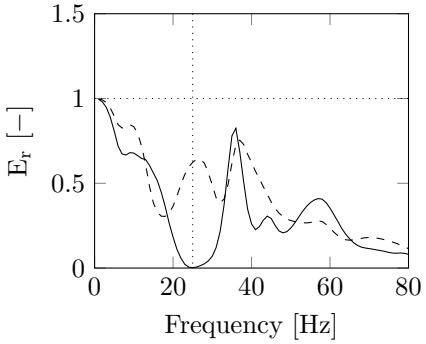

(d) E_r for 25 Hz

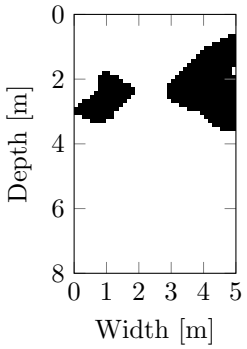

(e) Wave barrier for 50 Hz

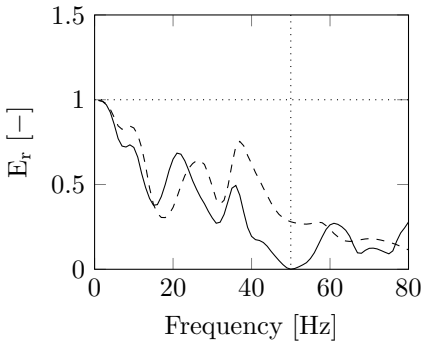

(f) E_r for 50 Hz

Figure B.5: The shape and performance of wave barriers optimized for single harmonic frequencies in a two-layer soil with interface at a depth of 4 m.

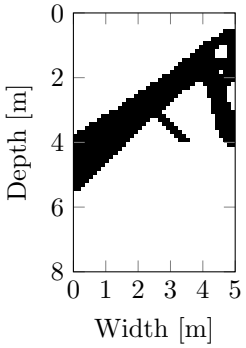

(a) Wave barrier for MINMAX

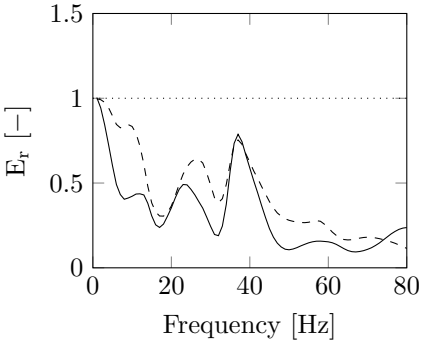

(b) E_r for MINMAX

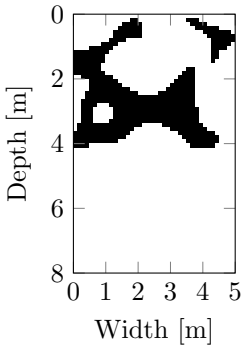

(c) Wave barrier for AVG

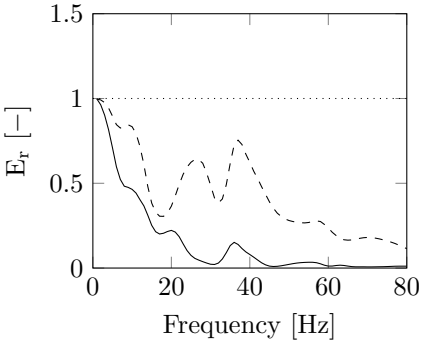

(d) E_r for AVG

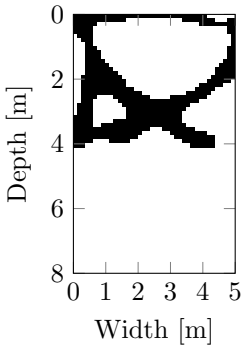

(e) Wave barrier for wAVG

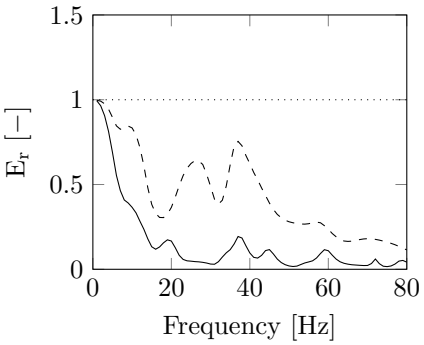

(f) E_r for wAVG

Figure B.6: The shape and performance of wave barriers optimized for single harmonic frequencies in a two-layer soil with interface at a depth of 4 m.

Appendix C

Topology optimized wave barriers for three-layered soil

C.1 Soil profile 3

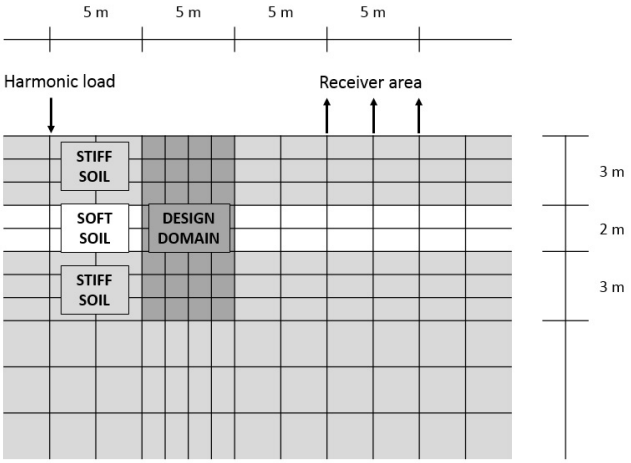

Figure C.1: Inner domain of model for soil profile 3

Layer	Depth (m)	E mod. (MPa)	Density (kg/m^3)	Poisson's ratio (-)	C_p (m/s)	C_s (m/s)
1	3	250	2000	0.45	689	208
2	5	50	1500	0.45	356	107
HS		250	2000	0.45	689	208

Table C.1: Soil properties of three-layered soil profile

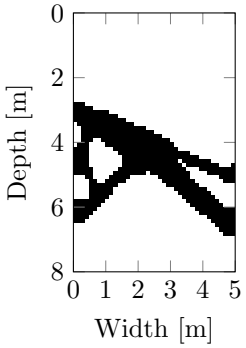

(a) Wave barrier for MINMAX

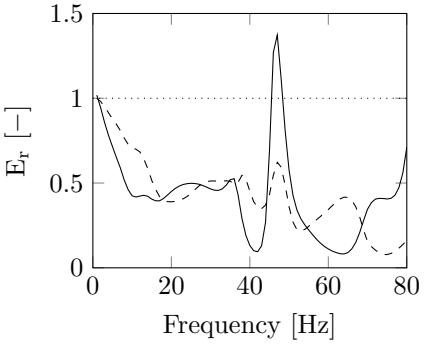

(b) E_r for MINMAX

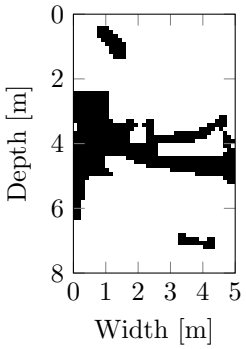

(c) Wave barrier for AVG

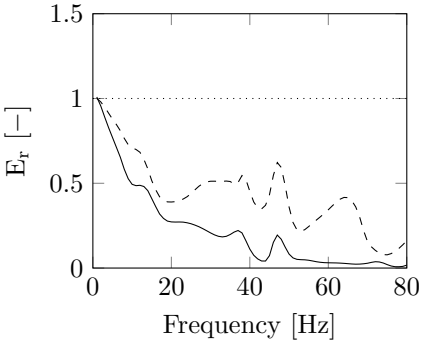

(d) E_r for AVG

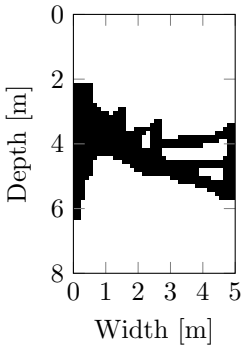

(e) Wave barrier for wAVG

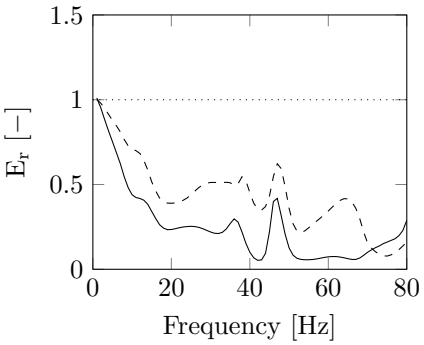

(f) E_r for wAVG

Figure C.2: The shape and performance of wave barriers optimized for min-max, average or weighted average objective functions in a three-layer soil.

Bibliography

[1] F. Wang, B. S. Lazarov, and O. Sigmund. On projection methods, convergence and robust formulations in topology optimization. *Structural and Multidisciplinary Optimization*, 43:767–784, 2011.

[2] K. D. Tsavdaridis, J. J. Kingman, and V. v. Toropov. Application of structural topology optimization to perforated steel beams. *Computers and Structures*, 158:108–123, 2015.

[3] D. Thompson. *Railway noise and vibration. Mechanisms, modeling and measures*. Elsevier, 2009.

[4] E. Peris, J. Woodcock, G. Sica, A. T. Moorhouse, and D. C. Waddington. Annoyance due to railway vibration at different times of day. *The Journal of the Acoustical Society of America*, 131:191–196, 2012.

[5] D. J. Thompson, J. Jiang, M. G. R. Toward, M. F. M. Hussein, A. Dijckmans, P. Coulier, G. Degrande, and G. Lombaert. Mitigation of railway-induced vibration by using subgrade stiffening. *Soil Dynamics and Earthquake Engineering*, 79:89–103, 2015.

[6] TNO Geologische Dienst Nederland. Ondergrondgegevens. `https://www.dinoloket.nl/ondergrondgegevens`. Accessed: 29-05-2018.

[7] D. J. Thompson, J. Jiang, M. G. R. Toward, M. F. M. Hussein, E. Ntotsios, A. Dijckmans, P. Coulier, G. Lombaert, and G. Degrande. Reducing railway-induced ground-borne vibration by using open trenches and soft-filled barriers. *Soil Dynamics and Earthquake Engineering*, 88:45–59, 2016.

[8] D. Lopez-Mendoza, A. Romero, D. P. Connolly, and P. Galvin. Scoping assessment of building vibration induced by railway traffic. *Soil Dynamics and Earthquake Engineering*, 93:147–161, 2017.

[9] H. V. C. Howarth and M. J. Griffin. Human response to simulated intermittent railway-induced building vibration. *Journal of Sound and Vibration*, 120:413–420, 1988.

[10] M. G. Smith, I. Croy, M. Ögren, and K. P. Waye. On the influence of freight trains on humans: a laboratory investigation of the impact of nocturnal low frequency vibration and noise on sleep and heart rate. *PLOS ONE*, 8:1–9, 2013.

[11] C. Van Hoorickx, M. Schevenels, and G. Lombaert. Double wall barriers for the reduction of ground vibration transmission. *Soil Dynamics and Earthquake Engineering*, 97:1–13, 2017.

[12] D. P. Connolly, G. P. Marecki, G. Kouroussis, I. Thalassinakis, and P. K. Woodward. The growth of railway ground vibration problems - a review. *Science of the Total Environment*, 568:1276–1282, 2016.

[13] A. Dijckmans, A. Ekblad, A. Smekal, G. Degrande, and G. Lombaert. Efficacy of a sheet pile wall as a wave barrier for railway induced ground vibration. *Soil Dynamics and Earthquake Engineering*, 84:55–69, 2016.

[14] S. J. Feng, X. L. Zhang, Q. T. Zheng, and L. Wang. Simulation and mitigation analysis of ground vibrations induced by high-speed train with three dimensional fem. *Soil Dynamics and Earthquake Engineering*, 94:204–214, 2017.

[15] A. T. Peplow, C. J. C. Jones, and M. Petyt. Surface vibration propagation over a layered elastic half-space with an inclusion. *Applied Acoustics*, 56:283–296, 1999.

[16] H. Takemiya and A. Fujiwara. Wave propagation/impediment in a stratum and wave impeding block (wib) measured for ssi response reduction. *Soil Dynamics and Earthquake Engineering*, 13:49–61, 1994.

[17] A. Dijckmans, P. Coulier, J. Jiang, M. G. R. Toward, D. J. Thompson, G. Degrande, and G. Lombaert. Mitigation of railway induced ground vibration by heavy masses next to the track. *Soil Dynamics and Earthquake Engineering*, 75:158–170, 2015.

[18] M. V. Tuler and S. Kaewunruen. Life cycle analysis of mitigation methodologies for railway rolling noise and groundborne vibration. *Journal of Environmental Management*, 191:75–82, 2017.

[19] C. Van Hoorickx, O. Sigmund, M. Schevenels, B. S. Lazarov, and G. Lombaert. Topology optimization of two-dimensional elastic wave barriers. *Journal of Sound and Vibration*, 376:95–111, 2016.

[20] C. Van Hoorickx, M. Schevenels, and G. Lombaert. Topology optimization of wave barriers for railway induced vibration in buildings. *VII European Congress on Computational Methods in Applied Sciences and Engineering*, 2016.

[21] P. Coulier, V. Cuellar, G. Degrande, and G. Lombaert. Experimental and numerical evaluation of effectiveness of a stiff wave barrier in the soil. *Soil Dynamics and Earthquake Engineering*, 77:238–253, 2015.

[22] N. Correia dos Santos, J. Barbosa, R. Calcada, and R. Delgado. Track-ground vibrations induced by railway-traffic: experimental validation of a 3d numerical model. *Soil Dynamics and Earthquake Engineering*, 97:324–344, 2017.

[23] K. A. Kuo, G. Lombaert, and G. Degrande. Quantifying dynamic soil-structure interaction for railway induced vibrations. *Procedia Engineering*, 199:2372–2377, 2017.

[24] P. Holscher. *Soil dynamics in urban areas*. Delft University of Technology, 2016.

[25] W. M. Ewing, W. S. Jardetzky, and F. Press. *Elastic waves in layered media*. McGraw-Hill Book Co., 1957.

[26] J. D. Achenbach. *Wave propagation in elastic solids*. North-Holland Publishing Company, 1973.

[27] G. F. Miller and H. Pursey. On the partition of energy between elastic waves in a semi-infinite solid. *Proceedings of the Royal Society of London*, 233:55–69, 1955.

[28] Lord Rayleigh. On wave propagated along the plane surface of an elastic solid. *Proceedings of the London Mathematical Society*, 17:4–11, 1885.

[29] T. G. Gutowski and C. L. Dym. Propagation of ground vibration: A review. *Journal of Sound and Vibration*, 49:179–193, 1976.

[30] H. Lamb. On the propagation of tremors over the surface of an elastic solid. *Philosophical Transactions*, 203:1–42, 1904.

[31] R. Stoneley. Elastic waves at the surface of separation of two solids. *Proceedings of the Royal Society of London*, 106:416–428, 1924.

[32] W. L. Pilant. Complex roots of the stoneley-wave equation. *Bulletin of the Seismological Society of America*, 62:285–299, 1972.

[33] P. W. Christensen and A. Klarbring. *An Introduction to Structural Optimization*. Springer, 2009.

[34] M. P. Bendsøe and N. Kikuchi. Generating optimal topologies in structural design using a homogenization method. *Computer Methods in Applied Mechanics and Engineering*, 71:197–224, 1988.

[35] M. P. Bendsøe. Optimal shape design as a material distribution problem. *Structural Optimization*, 1:193–202, 1989.

[36] M. Zhou and G. I. N. Rozvany. The coc algorithm, part ii: Topological, geometrical and generalized shape optimization. *Computer Methods in Applied Mechanics and Engineering*, 89:309–336, 1991.

[37] H. P. Mlejnek. Some aspects of the genesis of structures. *Structural Optimization*, 5:64–69, 1992.

[38] Y. M. Xie and G. P. Steven. A simple evolutionary procedure for structural optimization. *Computers & Structures*, 49:885–896, 1993.

[39] G. Allaire, F. Jouve, and A. M. Toader. A level-set method for shape optimization. *Comptes Rendus Mathematique*, 334:1125–1130, 2002.

[40] G. Allaire, F. Jouve, and A. M. Toader. Structural optimization using sensitivity analysis and a level-set method. *Journal of Computational Physics*, 194:363–393, 2004.

[41] M. Y. Wang, X. Wang, and D. Guo. A level set method for structural optimization. *Computational Methods in Applied Mechanics and Engineering*, 192:227–246, 2003.

[42] B. Bourdin and A. Chambolle. Design-dependent loads in topology optimization. *EASIM: Control, Optimisation and Calculus of Variations*, 9:19–48, 2003.

[43] 0. Sigmund and K. Maute. Topology optimization approaches. a comparative review. *Structural and Multidisciplinary Optimization*, 48:1031–1055, 2013.

[44] J. D. Deaton and R. V. Grandhi. A survey of structural and multidisciplinary continuum topology optimization: post 2000. *Structural and Multidisciplinary Optimization*, 49:1–38, 2014.

[45] M. P. Bendsøe and O. Sigmund. *Topology Optimization. Theory, Methods and Applications*. Springer, 2003.

[46] N. P. Van Dijk, K. Maute, M. Langelaar, and F. Van Keulen. Level-set methods for structural topology optimization a review. *Structural and Multidisciplinary Optimization*, 48:437–472, 2013.

[47] C. Van Hoorickx. *Design of vibration reduction measures for railway traffic by means of topology optimization.* PhD thesis, KU Leuven, 2017.

[48] G. Lombaert, G. Degrande, S. François, and D. J. Thompson. *Ground-Borne Vibration due to Railway Traffic: A Review of Excitation Mechanisms, Prediction Methods and Mitigation Measures. In: Nielsen J. et al. (eds) Noise and Vibration Mitigation for Rail Transportation Systems. Notes on Numerical Fluid Mechanics and Multidisciplinary Design*, volume 126. Springer, 2015.

[49] C. Zhao. *Dynamic and Transient Infinite Elements: Theory and Geophysical, Geotechnical and Geoenvironmental Applications.* Springer, 2009.

[50] C. Kirsch. *Non-reflecting boundary conditions for the numerical solution of wave propagation problems in unbounded domains.* PhD thesis, University of Basel, 2005.

[51] P. Joly. An elementary introduction to the construction and the analysis of perfectly matched layers for time domain wave propagation. *SeMA Journal*, 57:5–48, 2012.

[52] S. G. Johnson. Notes on perfectly matched layers (pmls), 2010.

[53] P. R. Loh, A. F. Oskooi, M. Ibanescu, M. Skorobogatiy, and S. G. Johnson. A fundamental relation between phase and group velocity, and application to the failure of perfectly matched layers in backward-wave structures. *Physical review. E, Statistical, nonlinear, and soft matter physics*, 79:065601, 2009.

[54] I. Harari and U. Albocher. Studies of fe/pml for exterior problems of time-harmonic elastic waves. *Computational Methods in Applied Mechanical Engineering*, 195:3854–3879, 2006.

[55] J. P. Berenger. A perfectly matched layer for the absorption of electromagnetic waves. *Journal of Computational Physics*, 114:185–200, 1994.

[56] I. Singer and E. Turkel. A perfectly matched layer for the Helmholtz equation in a semi-infinite strip. *Journal of Computational Physics*, 201:439–465, 2004.

[57] S. Marburg. Discretization requirements: How many elements per wavelength are necessary? In S. Marburg, editor, *Computational Acoustics of Noise Propagation in Fluids - Finite and Boundary Element Methods.* Springer, Berlin, Heidelberg, 2008.

[58] Q. Bo, L. Ali, and D. M. Irini. Numerical study of wave barrier and its optimization design. *Finite Element in Analysis and Design*, 84:1–13, 2014.

[59] M. P. Bendsøe and O. Sigmund. Material interpolation schemes in topology optimization. *Archive of Applied Mechanics*, 69:635–654, 1999.

[60] S. Xu, Y. Cai, and G. Cheng. Volume preserving nonlinear density filter based on heaviside functions. *Structural and Multidisciplinary Optimization*, 41:495–505, 2010.

[61] J. K. Guest, J. H. Prévost, and T. Belytschko. Achieving minimum length scale in topology optimization using nodal design variables and projection functions. *International Journal for Numerical Methods in Engineering*, 61:238–254, 2004.

[62] M. Zhou, B. S. Lazarov, F. Wang, and O. Sigmund. Minimum length scale in topology optimization by geometric constraints. *Computer Methods in Applied Mechanics and Engineering*, 293:266–282, 2015.

[63] S. Rojas-Labanda and M. Stolpe. Benchmarking optimization solvers for structural topology optimization. *Structural and Multidisciplinary Optimization*, 52:527–547, 2015.

[64] K. Svanberg. Some modelling aspects for the matlab implementation of mma, 2004.

[65] K. Svanberg. The method of moving asymptotes - a new method for structural optimization. *International Journal for Numerical Methods in Engineering*, 24:359–373, 1987.

[66] K. Svanberg. A class of globally convergent optimization methods based on conservative convex separable approximations. *Society for Industrial and Applied Mathematics*, 12:555–573, 2002.

[67] K. Svanberg. Mma and gcmma - two methods for nonlinear optimization, 2007.

[68] D. A. Tortorelli and P. Michaleris. Design sensitivity analysis: Overview and review. *Inverse Problems in Engineering*, 1:71–103, 1994.

[69] Y. B. Yang and H. H. Hung. A parametric study of wave barriers for reduction of train-induced vibrations. *International Journal for Numerical Methods in Engineering*, 40:3729–3747, 1997.

[70] A. T. Gaynor and J. K. Guest. Topology optimization considering overhang constraints: Eliminating sacrificial support material in additive manufacturing through design. *Structural and Multidisciplinary Optimization*, 54:1157–1172, 2016.